NASA Technical Memorandum 4009

Semiempirical Method for Prediction of Aerodynamic Forces and Moments on a Steadily Spinning Light Airplane

Bandu N. Pamadi
Vigyan Research Associates, Inc.
Hampton, Virginia

Lawrence W. Taylor, Jr.
Langley Research Center
Hampton, Virginia

National Aeronautics
and Space Administration

**Scientific and Technical
Information Division**

1987

Contents

List of Tables

List of Figures

Summary

A semiempirical method is presented for the estimation of aerodynamic forces and moments acting on a steadily rotating airplane. The airplane is divided into wing, body, and horizontal and vertical tail surfaces. The strip theory is employed to wing, body, and horizontal tail surfaces to determine their contribution to the total aerodynamic coefficients. The strip theory takes sectional, two-dimensional static aerodynamic coefficients as input and predicts rotary aerodynamic coefficients. For wing and horizontal tail surfaces, such input data are usually available from static wind-tunnel tests. However, for the body, the static test data are not normally available in the required form. Therefore, a semiempirical approach is developed for the prediction of static aerodynamic characteristics at combined high angles of attack and sideslip to produce the required input to the body strip theory. For the vertical tail surface, strip theory is not applied because of its low aspect ratio; therefore, a direct method is employed. All the mutual interferences between wing, body, and tail surfaces are ignored except the mutual interference between horizontal and vertical tail surfaces (shielding effect). A mathematical model for estimating the shielded area of the vertical tail at high angles of attack is developed based on available experimental data. The predictions of the strip theory based on static aerodynamic input data were found to differ considerably from the corresponding rotary balance test data. For wing and horizontal tail surfaces, the rotational flow model proposed by McCormick (NASA CR-165680) is used to determine additional contributions of these components. For the vertical tail, a model called "secondary flow effect" is developed to account for the curved flow effects over the vertical tail.

The analysis of the paper is quite general. However, some specific applications are considered in this paper. This theory is applied to a light, low-wing, single-engine, general aviation airplane, extensively studied in the NASA Langley stall/spin research program.

In general, the predicted trends of the rotary (spin) aerodynamic coefficients are consistent with the spin-tunnel rotary balance test data. The agreement is reasonably good at low and moderate angles of attack and moderate spin rates. However, at higher angles of attack or high spin rates, the differences become significant, particularly in estimation of side force and yawing moment. These deficiencies are attributed to various difficulties in modeling complex aerodynamics of the spinning airplane.

Introduction

The prediction and analysis of airplane stall/spin characteristics have been of great interest to designers since the beginning of aviation. This problem has assumed more importance in recent years because the uncontrolled motions of the airplane associated with stall/spin have caused significant loss to the military and civil aviation (ref. 1). Although considerable progress has been made in recent years in the areas of experimental and flight testing techniques related to stall/spin problems, an adequate mathematical model is still not available for simulation of aerodynamic forces and moments in spin.

The phenomenon of loss of damping in roll and autorotation of stalled wings has been generally recognized as a primary cause of spin for light airplanes. The spinning motion usually involves sideslip, pitching, rolling, and yawing about the body axes, and the airplane descends towards the Earth with its center of gravity describing a helical path. In steady-state spin, the aerodynamic forces and moments acting on the airplane are in equilibrium with inertia forces and moments. However, the establishment of balance between aerodynamic and inertial moments has been found to be of crucial importance in attaining a steady-state spin. If the airplane cannot find such a balance, the spinning motion remains oscillatory. The radius of spin is usually of the order of 1 semispan of the wings. However, with an increase in angle of attack α and spin rate, the spin radius approaches zero. In steep spin ($\alpha_{\text{stall}} < \alpha < 45°$), the dominant part of the aerodynamic moment is the rolling moment which mainly comes from the wings. In flat spin ($45° < \alpha < 90°$), the major component of the aerodynamic moment happens to be the yawing moment, and the chief contribution comes from the body as the vertical tail is often rendered ineffective because of the shielding effect created by the wake from the horizontal tail. Additional information on the airplane spin can be found in references 2 and 3.

The aerodynamics associated with a spinning airplane is quite complex. It is dominated by extensive regions of separated flows and complex mutual interference between various aerodynamic surfaces. Still, it remains as one of the most challenging problems of aerodynamics. The traditional approach based on the stability derivative concept does not prove useful in the analysis of spinning motion because the aerodynamic forces and moments at poststall conditions display high nonlinearity with angle of attack and spin rate. This problem, at present, is still beyond the reach of computational fluid dynamic methods. In view of this, a semiempirical analysis based on as much physical information as possible and derived

from experimental work can play an important role in the theoretical analysis of airplane spin.

Glauert (ref. 3), Gates and Bryant (ref. 4), and Wykes, Casteel, and Collins (ref. 5) employed strip theory to estimate the aerodynamic characteristics of a steadily spinning airplane. The strip theory takes static aerodynamic data as input and predicts the rotary aerodynamic coefficients. These studies were limited to the analysis of steep spins. The problem of flat spins, where both the angle of attack and spin rates can be quite high, was not given much attention. Nonavailability of an adequate aerodynamic mathematical model led to the development of the spin-tunnel rotary balance apparatus for generating the pertinent aerodynamic test data (ref. 6). By incorporating the spin-tunnel rotary balance aerodynamic test data into the six-degree-of-freedom equations of motion, it has been demonstrated that the steady-state spins can usually be predicted (refs. 7 and 8). Thus, the experimental data base generated by rotary balance tests has played a very useful role in understanding the stall spin problems. On the other hand, for a spinning airplane, the experimental investigations dealing with flow visualization and pressure measurements similar to those carried out for rotating propellers (ref. 9) and which could provide insight to develop a comprehensive theory are almost nonexistent.

In the present study, an effort has been made to estimate the aerodynamic forces and moments acting on a light spinning airplane. Here, the airplane is considered to be steadily rotating about a vertical axis analogous to a model undergoing spin-tunnel rotary balance tests so that the present theory ties in as closely as possible with the rotary balance test data. Also, this condition approximates quite well an airplane in a steady-state spinning flight. Angles of attack up to 90° and reduced spin rates up to 1.0 are considered in the present analysis.

The airplane model is considered to be divided into wing, body, horizontal and vertical tail surfaces. The effect of power is ignored. The strip theory used for wing and horizontal tail surfaces is based on the input of sectional, two-dimensional static wind-tunnel test data (ref. 10) and is similar to the methods used in earlier studies (refs. 3 and 4). However, for the body, the static wind-tunnel test data in sectional coefficient form are not usually available. Therefore, a semiempirical approach is developed to predict the static aerodynamic characteristics at combined high angles of attack and sideslip to generate the required input to body theory. All the interference effects between wing, body, and tail surfaces are ignored except the mutual interference between horizontal and vertical tail surfaces (shielding effect). A procedure for estimating the shielded area of the vertical tail is developed based on experimental data and is incorporated in the calculation of vertical tail aerodynamic characteristics.

The predictions of the strip theory based on the static aerodynamic input data were found to differ considerably from the corresponding rotary balance test data (refs. 11 and 12). This discrepancy is attributed to the presence of curved or rotational fluid flow. Herein the term "rotational flow" is used to refer to the curved nature of the flow due to angular velocity Ω. The simple strip theory accounts only for the kinematics associated with angular velocity Ω and has no mechanism to handle the physical aspects of the flow pattern. A brief description of the flow field over rotating airplane surfaces is presented based on available information in the literature. For wing and horizontal tail surfaces, the rotational flow model proposed by McCormick (ref. 13) is employed to determine additional contributions of these components. The rotational flow effects are ignored for the body. For the vertical tail, a secondary flow model is proposed to account for its curved flow effects.

The strip theory is applied to a light, single-engine, low wing general aviation airplane which has been extensively studied as model A in references 10, 11, 12, 14, and 15. We have presented calculations for the basic configuration of the model A airplane of references 10, 11, 12, 14, and 15, whose tail configuration is designated as tail 4, and two other tail configurations (3 and 5). The presentation of results follows the pattern of spin-tunnel rotary balance test data of references 10 through 12. The nomenclature adopted is also similar to that used in these references.

For application of the present method to other light airplane configurations, it is necessary to have the input empirical data in the form similar to that discussed.

Some partial results of this investigation have been presented by the authors to recent conferences (refs. 16 and 17). An extension of the strip theory approach to wings of arbitrary planform is presented in reference 18.

Symbols

A	axial force
AR	aspect ratio
b_H	horizontal tail span
b_h	local width of body cross section
b_V	vertical tail span
b_W	wing span

C_A axial-force coefficient, $\frac{\text{Axial force}}{\frac{1}{2}\rho U_\infty^2 S_W}$

C_D drag coefficient

C_L lift coefficient, $\frac{\text{Lift}}{\frac{1}{2}\rho U_\infty^2 S_W}$

C_l rolling-moment coefficient, $\frac{\text{Rolling moment about cg}}{\frac{1}{2}\rho U_\infty^2 S_W b_W}$

C_m pitching-moment coefficient, $\frac{\text{Pitching moment about cg}}{\frac{1}{2}\rho U_\infty^2 S_W \bar{c}_W}$

C_N normal-force coefficient, $\frac{\text{Normal force}}{\frac{1}{2}\rho U_\infty^2 S_W}$

C_n yawing-moment coefficient, $\frac{\text{Yawing moment about cg}}{\frac{1}{2}\rho U_\infty^2 S_W b_W}$

C_X two-dimensional axial-force coefficient

$C_{X,c}$ axial-force coefficient of two-dimensional square section

C_Y side-force coefficient, $\frac{\text{Side Force}}{\frac{1}{2}\rho U_\infty^2 S_W}$

C_Y^* side-force coefficient of unshielded vertical tail

$C_{Y,c}(\text{B})$ side-force coefficient of idealized two-dimensional body cross section of model A airplane

$C_{Y,c}(\text{SC})$ side-force coefficient of two-dimensional square cross section

c local chord

c_d drag coefficient of circular cylinder

c_f chord of flat plate

$\bar{c}_W$ wing mean geometric chord

D drag force

d_f maximum width of flat-plate wake

$F_{Y,V}$ vertical tail side force

h_V vertical distance between X-axis and centroid of unshielded area of vertical tail

k_1, k_2 apparent mass coefficients of body

L lift force

l length of body

l_H horizontal tail length, distance between 0.25 mean aerodynamic chord of horizontal tail and airplane center of gravity

l_V vertical tail length, distance between 0.25 mean aerodynamic chord of vertical tail and airplane center of gravity

N normal force

N_{Re} Reynolds number

p pressure

p_o stagnation pressure

p_s static pressure

p_w pressure in wake

q local dynamic pressure

q_∞ free-stream dynamic pressure, $\frac{1}{2}\rho U_\infty^2$

R spin radius

r radius

r_c corner radius of square cross section

r_j radius of impinging airstream

r_V streamwise coordinate of stagnation streamline in secondary flow over vertical tail

S area

S_B cross-sectional area of body

$S_{B,max}$ maximum cross-sectional area of body

S_s shielded area

$S_{V,eff}$ effective vertical tail cross-sectional area

U local velocity

U_s velocity along stagnation streamline (fig. 15)

U_∞ free-stream velocity

V_B volume of body

X, Y, Z axis system

x, y, z coordinate system attached to body with origin at center of gravity

x_{cg} center-of-gravity location, measured from nose of body

$\bar{x}_{cg}$ $= \frac{x_{cg}}{c}$

$\bar{x}_{cp}$ center of pressure of wing measured from leading edge and expressed in terms of chord

α	angle of attack
α_ℓ	local angle of attack
β	sideslip angle
Δ	elemental quantity (strip)
ϵ	correction factor for three-dimensional effects over body
η_H	horizontal tail efficiency, q_H/q_∞
η_{stall}	spanwise extent of stall over wing or horizontal tail, $\frac{2y_{stall}}{b_W \text{ or } b_H}$
η_V	vertical tail efficiency, $\frac{q_V}{q_\infty}$
θ	$= \tan^{-1} \frac{\Omega y}{U}$
θ_H	$= \tan^{-1} \frac{\Omega y_H}{U_H}$
λ	$= \tan^{-1} \frac{\Omega b}{2U}$
λ_H	$= \tan^{-1} \frac{\Omega b_H}{2U_H}$
ρ	density
ϕ	cross-flow angle, $\tan^{-1} \frac{\tan \beta}{\sin \alpha}$
ϕ_c	cross-flow angle when $C_Y = 0$
ω	reduced spin rate, positive for right spin and negative for left spin (as viewed from top), $\Omega b/2U$
Ω	angular velocity about spin axis, positive for right spin and negative for left spin (as viewed from top)

Subscripts:

L	left
ℓ	strip or local
max	maximum
min	minimum
R	right
stall	condition or parameter at stall

Superscript:

$'$	parameter in rotational or secondary flow effect

Abbreviations (also used as subscripts):

B	body (fuselage)
cg	center of gravity
H	horizontal tail
V	vertical tail
W	wing
2-D	two-dimensional

Analysis

Let us consider an airplane model, mounted on a rotary balance apparatus in the spin tunnel and steadily rotating at a constant angular velocity Ω about the spin axis, which is vertical. A schematic sketch of this configuration is shown in figure 1. For the purpose of this analysis, the following assumptions are introduced, mainly because we intend to tie the present theory as closely as possible to the test conditions employed in the rotary balance tests (refs. 11 and 12), which could be generally different from those encountered in actual steady-state spin of the free airplane:

1. The spin axis passes through the model center of gravity so that the spin radius R and sideslip at center of gravity are zero
2. The Y-axis of the airplane lies in the horizontal plane so that the bank angle is zero
3. The effect of power is ignored and the model configuration without propeller is considered in the analysis
4. The control surface deflections are zero; in the present analysis, the dihedral effects of wing and horizontal tail are ignored and the mutual aerodynamic interferences between various airplane components are ignored except the interference between horizontal and vertical tail surfaces (shielding effect); however, it is possible that some of the interference effects not considered herein could be significant, as discussed later, and need proper modeling
5. Difference between tunnel test and flight Reynolds number is ignored

In strip theory approach, the surface (say wing) is usually divided into a number of strips. The force on each strip is assumed to be the same as it would be were the surface moving with an equivalent linear velocity, that is, the vector sum of all the linear velocities at that strip. For a rectangular wing with strips oriented normal to the Y-axis (fig. 2), this equivalent velocity is equal to $U + \Omega y$. The strip theory approach used for wings and horizontal tails is similar to that employed by Glauert (ref. 3).

Wing Contribution

Strip theory calculations. Consider the airplane model to be rotating in a clockwise (positive) direction as viewed from the top. The effect of the angular velocity in spin Ω is to induce, at any spanwise location y, a velocity component equal to Ωy as indicated

in figure 2. As a result, the local angle of attack α_ℓ on the right wing increases and that on the left wing decreases compared with the angle of attack at the root chord α. The maximum and minimum values of α occur, respectively, at the right and left wing tips. We have

$$\alpha_\ell = \alpha \pm \theta \tag{1}$$

where

$$\theta = \tan^{-1} \frac{\Omega y}{U}$$

In equation (1), the + sign applies to the right wing and the − sign applies to the left wing; the variations in the angle of attack across the wing span can be substantial. For the spin-tunnel model of reference 14, the figures are as follows:

For a steep spin,

$$\alpha = 50^\circ \qquad \omega = 0.33 \qquad \alpha_{max} = 68.3^\circ \qquad \alpha_{min} = 34.3^\circ$$

and for a flat spin,

$$\alpha = 80^\circ \qquad \alpha_{max} = 111.79^\circ \qquad \alpha_{min} = 48.21^\circ$$

It may be observed that for this case, the flow close to the right wing tip is actually reversed; that is, it comes from the trailing edge.

The local dynamic pressure is given by

$$q_\ell = \frac{1}{2}\rho U_\infty^2 \left[1 + \left(\frac{\Omega y}{U_\infty}\right)^2\right] \tag{2}$$

The lift and drag forces on any strip of width dy are

$$\Delta L = \frac{1}{2}\rho U_\infty^2 \left[1 + \left(\frac{\Omega y}{U_\infty}\right)^2\right] C_{L,\ell} c \, dy \tag{3}$$

and

$$\Delta D = \frac{1}{2}\rho U_\infty^2 \left[1 + \left(\frac{\Omega y}{U}\right)^2\right] C_{D,\ell} c \, dy \tag{4}$$

Here, $C_{L,\ell}$ and $C_{D,\ell}$ are the sectional lift and drag coefficients to be evaluated for the corresponding angle of attack α_ℓ which depends on the angle of attack at the root α and the spin rate Ω.

The normal and chordwise forces on the strip are given by

$$\Delta N = \Delta L \cos(\alpha \pm \theta) + \Delta D \sin(\alpha \pm \theta) \tag{5}$$

and

$$\Delta A = -\Delta L \sin(\alpha \pm \theta) + \Delta D \cos(\alpha \pm \theta) \tag{6}$$

The aerodynamic coefficients of the wing (based on the free-stream dynamic pressure q_∞, wing area S_W, and wing mean geometric chord $\bar{c}_W$ can then be derived as follows (refs. 2 and 3):

$$C_{N,W} = \frac{1}{2 \tan \lambda} \int_0^\lambda \left[\Delta C_{N,R} + \Delta C_{N,L}\right] \sec^4 \theta \, d\theta \tag{7}$$

$$C_{A,W} = \frac{1}{2 \tan \lambda} \int_0^\lambda \left[\Delta C_{A,R} + \Delta C_{A,L}\right] \sec^4 \theta \, d\theta \tag{8}$$

$$C_{l,W} = \frac{1}{4 \tan^2 \lambda} \int_0^\lambda \left[\Delta C_{N,L} - \Delta C_{N,R}\right] \times \tan \theta \sec^4 \theta \, d\theta \tag{9}$$

$$C_{n,W} = \frac{1}{4 \tan^2 \lambda} \int_0^\lambda \left[\Delta C_{A,L} - \Delta C_{A,R}\right] \times \tan \theta \sec^4 \theta \, d\theta \tag{10}$$

$$C_{m,W} = \frac{1}{4 \tan^2 \lambda} \int_0^\lambda \left[\Delta C_{N,R} + \Delta C_{N,L}\right] \times (\bar{x}_{cg} - \bar{x}_{cp}) \sec^4 \theta \, d\theta \tag{11}$$

where $\bar{x}_{cp}$ is the center-of-pressure location measured from the nose of the body (in wing chords). The side-force coefficient of the wings $C_{Y,W}$ is generally small and is neglected:

$$C_{Y,W} = 0 \tag{12}$$

In equations (3) to (11), the wing section coefficients, $C_{L,\ell}$ and $C_{D,\ell}$, and $\bar{x}_{cp}$ are input parameters which must be known a priori. However, for a particular airplane under consideration, if the actual wind-tunnel test data are not available, the data given in references 19 through 21 can be used.

Effect of angular velocity on wing. The spin-tunnel rotary balance test data (refs. 11 and 12) indicate that the aerodynamic coefficients—particularly, normal force, rolling, and pitching moments—display a pronounced dependence on spin rate. When compared with these data, the prediction of strip theory with static wind-tunnel test data as input differs appreciably. The reasons for such discrepancies include (1) the induced flow from neighboring strips, (2) cross flow due to pressure gradients perpendicular to the strips, (3) centrifugal forces, and (4) curved flow.

The effect of spin rate on the aerodynamic forces and moments of a spinning wing, as recorded by the rotary balance test data (refs. 11 and 12), can be summarized as follows:

Low angles of attack (below stall, say $0^\circ < \alpha < 20^\circ$): With an increase in spin rate,

1. The normal force decreases

2. The rolling moment decreases and becomes more damping in nature
3. The pitching moment increases initially but starts dropping subsequently

High angles of attack (above stall, $\alpha > 20°$): With an increase in spin rate,

1. The normal force increases continuously
2. The rolling moment decreases appreciably and becomes more damping; however, for extremely high α, the trend reverses and rolling moment increases with α
3. Pitching moment decreases monotonically

Studies which could provide some physical insight into the flow pattern and pressure variation over a spinning airplane wing and could have been helpful in the development of a mathematical model are almost nonexistent. This is a complex aerodynamic problem because it is dominated by extensive regions of separated flow, strong viscous-inviscid interaction, and configuration and Reynolds number dependence in addition to the presence of spin rate. The analysis of such a flow problem is considered to be beyond the scope of the present study. Instead, we propose to develop an approximate solution suitable for engineering purposes with the help of available experimental studies related to this subject. A brief description of some related investigations reported in literature is presented in the following sections.

Studies at low angles of attack. In reference 9, Himmelskamp has reported wind-tunnel tests on a rotating propeller. The model he tested had two blades with a chord of 12 cm, a hub diameter of 10 cm, and a tip diameter of 50 cm (AR = 8.33). (See fig. 3.) The cross-sectional shape was profile No. 625 of the Goettingen collection with a thickness-to-chord ratio of 0.20. The advance ratio $U/\Omega R$ was varied from 0.124 to 0.459. However, the angle of attack of the blade sections was not varied directly; instead various combinations of tunnel velocity and advance ratio were employed to get the desired angle-of-attack variation. Himmelskamp has presented test results in the form of sectional lift and drag coefficients based on local dynamic pressure at various radial locations from 40 to 80 percent radius. These results are given in figure 3. The local lift and drag coefficients of the blade sections close to the hub are higher than those located outboard. Also, the sectional aerodynamic lift and drag coefficients are greater than corresponding two-dimensional static wind-tunnel test data. Himmelskamp attributes these increases in sectional lift and drag to the phenomenon of local thinning of boundary layer near the hub and Coriolis force acting favorably on fluid particles.

If Himmelskamp's test propeller is considered as a rectangular untwisted wing with a chord of 12 cm, span of 100 cm, and AR of 8.33 and set in spinning motion similar to a wing model undergoing rotary balance tests, we have carried out a strip theory analysis using sectional lift and drag data of figure 3 as input empirical parameters. Calculations extend only to $\omega = 0.35$ on account of limitations in data. The results of these calculations are presented in figure 4 along with the spin-tunnel rotary balance test data (ref. 12) for a spinning airplane configuration of rectangular wing planform (AR = 6.10). From figure 4, there is qualitative agreement despite the differences in two geometries. From this, we can infer the following:

1. The type of physical flow pattern leading to higher values of sectional lift and drag, particularly for inboard sections observed on a rotating propeller (ref. 9) in axial flow, may also occur over a spinning wing at low angles of attack
2. With such empirical data which incorporate the physics of the flow as input, the strip theory is capable of providing meaningful estimates of the aerodynamic coefficients of a rotating (spinning) wing

Studies at high angles of attack. The flow over a spinning, stalled wing is exceedingly complex and is not thoroughly understood. The situation is aggravated by a dearth of experimental data which treat local flow and pressures. It is necessary, then, to deduce what one can from the average or total force and moment measurements.

Application of the strip theory used previously for low angles of attack to the stalled wing results in the normal-force coefficients presented in figure 5. The normal-force coefficient for $\alpha = 90°$ is seen to increase by about one third at $\omega = 1$, which is consistent with the average increase of dynamic pressure due to spinning. Extrapolation of the rotary balance test data, however, shows an increase of about one in the normal-force coefficient for $\alpha = 90°$ and $\omega = 1$. After adjusting for differences at $\omega = 0$, the discrepancy is seen to grow approximately with the square of ω.

Unfortunately, there is no accepted theory which accounts for this discrepancy in C_N. Matters are made worse by the manner in which normal force is nondimensionalized by dividing by the free-stream velocity. A spinning wing at $\alpha = 90°$ will create a normal force if the airfoil section is cambered as in this paper even when the free-stream velocity approaches zero. The consequence is that the nondimensional normal-force coefficient and ω will grow

without bound as U approaches zero. Propeller characteristics are usually nondimensionalized by using the tip velocity which avoids this singularity.

In reference 13, McCormick hypothesizes that relatively stagnant air on the lee side of a stalled spinning wing will have a spanwise pressure gradient due to centrifugal force. The resulting reduced pressure in the center portion of the wing gives rise to an increase in the normal-force coefficient (fig. 6); that is,

$$C'_{N,\mathrm{W}} = \frac{\omega^2}{3}\left(1+\eta_s^3\right)$$

where $\eta_s = \frac{2y_s}{b_\mathrm{W}}$, the normalized spanwise location of the stalled region. It is assumed that the spin axis is at $y = 0$. The corresponding increment for rolling-moment coefficient is

$$C'_{l,\mathrm{W}} = \mp\frac{\omega^2}{16}\left(1-\eta_s^4\right)$$

The expression for $C'_{l,\mathrm{W}}$ in reference 13 seems to be incorrect.

The corresponding change in the pitching-moment coefficient is

$$C'_{m,\mathrm{W}} = C'_{N,\mathrm{W}}\left(\bar{x}_{\mathrm{cg}} - \bar{x}'_{\mathrm{cp}}\right)$$

where $\bar{x}'_{\mathrm{cp}}$ is the center of pressure and is assumed to be equal to 0.5.

The addition of the correction term to the normal-force coefficient is seen in figure 6 to compare more closely with the experimental data. The similar comparison in figure 7 for rolling-moment coefficient also shows reasonable correlation. Unfortunately, it is not possible to validate the detailed assumptions integral to the McCormick model because of the lack of local flow measurements for spinning stalled wings.

Body Contribution

The cross-sectional shape of the body and Reynolds number have a significant influence on the spin and recovery characteristics of the airplanes (refs. 22 through 24). Bodies having rectangular or square cross sections with sharp corners particularly in the aft portion, produce autorotative side-force and yawing moments. These studies indicate that rounding off the bottom corners generally produces a damping effect whereas rounding off the top corners often does not alter the basic prospin tendency.

Polhamus (ref. 24) has studied the two-dimensional axial- and side-force characteristics of noncircular cross sections having various corner radii at subcritical and supercritical Reynolds numbers. He finds that the corner radius and Reynolds number have a strong effect on the side-force characteristics of two-dimensional noncircular cylinders. In figure 8, Polhamus' experimental data for two-dimensional square cylinders of various corner radii are presented. For a square section with rounded corners, at subcritical Reynolds numbers, the side force is positive (prospin) for small values of ϕ and becomes negative (antispin) at supercritical Reynolds numbers. However, for the section having an 8-percent corner radius, the Reynolds number has very little effect on the side-force variation. This pronounced effect of the Reynolds number may sometimes cause the spin-tunnel free-flight model to exhibit a flat spin mode, whereas the full-scale airplane may refuse to enter a flat spin (ref. 15). Such complex behavior of noncircular cross-sectional bodies typical of airplane bodies requires considerable care in making theoretical analyses of spinning airplanes.

During a spin, the body operates at a high angle of attack, and its cross sections experience a varying sideslip. At present, no comprehensive method is available for the prediction of aerodynamic characteristics of noncircular cross-sectional bodies operating at combined high angles of attack and sideslip. Therefore, in the following sections, a semiempirical procedure is developed for a static body operating at (1) angle of attack, (2) sideslip, and (3) combined angles of attack and sideslip. Then this procedure is extended to the problem of a spinning body with the use of strip theory.

For the analysis of static body at angles of attack and sideslip, a coordinate system as shown in figure 9 is assumed where the origin is the location at the nose. However, for the spinning body, the same coordinate system as defined earlier with the origin at the center of gravity (fig. 2) is employed.

Body at angle of attack. According to Allen (ref. 25), for a body of revolution at small angle of attack,

$$C_{L,\mathrm{B}} = \frac{(k_2-k_1)\sin 2\alpha\cos\frac{\alpha}{2}}{S_{\mathrm{B,max}}}\int_0^l \frac{dS_\mathrm{B}}{dx}\,dx + \frac{2\sin^2\alpha\cos\alpha}{S_{\mathrm{B,max}}}\int_0^l \epsilon r c_d\,dx \tag{19}$$

$$C_{D,\mathrm{B}} = \frac{(k_2-k_1)\sin 2\alpha\sin\frac{\alpha}{2}}{S_{\mathrm{B,max}}}\int_0^l \frac{dS_\mathrm{B}}{dx}\,dx + \frac{2\sin^3\alpha}{S_{\mathrm{B,max}}}\int_0^l \epsilon r c_d\,dx \tag{20}$$

$$C_{m,\mathrm{B}} = \frac{(k_2 - k_1)\sin 2\alpha \cos\frac{\alpha}{2}}{V_\mathrm{B}} \int_0^l \frac{dS_\mathrm{B}}{dx}(x_\mathrm{cg} - x)\, dx + \frac{2\sin^2\alpha}{V_\mathrm{B}} \int_0^l \epsilon r c_d (x_\mathrm{cg} - x)\, dx \tag{21}$$

In equations (19) to (21), the first term represents the potential term proposed originally by Munk (ref. 26), and the second term is Allen's modification (ref. 25) to Munk's theory derived from the viscous cross-flow concepts containing the empirical two-dimensional drag coefficient (c_d) of the circular cylinder. The zero-lift drag term appearing in Allen's equation (ref. 25) is ignored. Jorgensen (ref. 27) extends this approach to noncircular bodies with the following modification:

$$C_{L,\mathrm{B}} = \frac{C_1 (k_2 - k_1)\sin 2\alpha \cos\frac{\alpha}{2}}{S_{\mathrm{B,max}}} \int_0^l \frac{dS_\mathrm{B}}{dx}\, dx + \frac{\sin^2\alpha\cos\alpha}{S_{\mathrm{B,max}}} \int_0^l \epsilon b_h C_{X,c}\, dx \tag{22}$$

$$C_{D,\mathrm{B}} = \frac{C_1 (k_2 - k_1)\sin 2\alpha \sin\frac{\alpha}{2}}{S_{\mathrm{B,max}}} \int_0^l \frac{dS_\mathrm{B}}{dx}\, dx + \frac{\sin^3\alpha}{S_{\mathrm{B,max}}} \int_0^l \epsilon b_h C_{X,c}\, dx \tag{23}$$

$$C_{m,\mathrm{B}} = \frac{C_1 (k_2 - k_1)\sin 2\alpha \cos\frac{\alpha}{2}}{V_\mathrm{B}} \int_0^l \frac{dS_\mathrm{B}}{dx}(x_\mathrm{cg} - x)\, dx + \frac{\sin^2\alpha}{V_\mathrm{B}} \int_0^l \epsilon b_h C_{X,c}(x_\mathrm{cg} - x)\, dx \tag{24}$$

The modifications are (1) the first term is multiplied by a constant C_1 so that the quantity $C_1 (k_2 - k_1)$ represents the apparent mass coefficient of the noncircular cross section and (2) the coefficient $C_{X,c}$ (based on b_h) replaces c_d and represents the cross-flow drag coefficient of the noncircular cross section. It may be noted that for a circular cross section, $C_1 = 1.0$, $b_h = 2r$, and $C_{X,c} = c_d$.

Jorgensen (ref. 27) proposes that equations (22) to (24) be applied for $\alpha = 0°$ to $90°$. In the present analysis, all the concepts proposed by Jorgensen (ref. 27) are used.

If C_L and C_D are known, the normal- and axial-force coefficients can be determined from equations (5) and (6). Since the axial force does not produce any moment about the spin axis, it is not addressed.

Body in sideslip. For a noncircular body in sideslip, we extend Jorgensen's concept (ref. 27) as follows:

$$C_{Y,\mathrm{B}} = -\frac{C_1 (k_2 - k_1)\sin 2\beta \cos\frac{\beta}{2}}{S_{\mathrm{B,max}}} \int_0^l \frac{dS_\mathrm{B}}{dx} + \frac{\sin^2\beta}{S_{\mathrm{B,max}}} \int_0^l \epsilon b_h C_{Y,c}\, dx \tag{25}$$

and

$$C_{n,\mathrm{B}} = -\frac{C_1 (k_2 - k_1)\sin 2\beta \cos\frac{\beta}{2}}{V_\mathrm{B}} \int_0^l \frac{dS_\mathrm{B}}{dx}(x_\mathrm{cg} - x)\, dx + \frac{\sin^2\beta}{V_\mathrm{B}} \int_0^l b_h \epsilon C_{Y,c}(x_\mathrm{cg} - x)\, dx \tag{26}$$

In equations (25) and (26), notice that the first term has a negative sign and the empirical side-force coefficient $C_{Y,c}$ (which is supposed to embody the side-force characteristics of a noncircular cross section) replaces $C_{X,c}$. In equations (22) through (26), $C_{X,c}$ and $C_{Y,c}$ are empirical parameters. Therefore, to proceed with the calculations, it is necessary to have this information from experimental data.

The rolling moment developed by the body is generally small because of its limited moment arm and is ignored.

Combined angles of attack and sideslip. For any combination of α and β ($\alpha \neq 0$), we can define a cross-flow angle ϕ (fig. 9) such that,

$$\tan\phi = \frac{\tan\beta}{\sin\alpha} \tag{27}$$

Equation (27) relates the sectional cross-flow angle ϕ with angles of attack and sideslip. To evaluate the aerodynamic forces and moments under combined α and β, the proposed procedure is as follows:

1. For the given values of α and β, find the value of ϕ from equation (27)
2. Obtain the corresponding values of $C_{X,c}$ and $C_{Y,c}$ for the subject cross-sectional shape from the experimental data which, as said before, is supposed to be available
3. With these values of $C_{X,c}$ and $C_{Y,c}$, solve equations (19) through (27) to obtain the required aerodynamic coefficients

Strip theory calculations. The variation of cross-flow angle and dynamic pressure along the length of a rotating body are given by

$$\phi(x) = \tan^{-1}\frac{\Omega x}{U_\infty} \tag{28}$$

$$q_l(x) = \frac{1}{2}\rho U_\infty^2 \left[1 + \left(\frac{\Omega x \sin\alpha}{U_\infty}\right)^2\right] \quad (29)$$

Notice that the cross-flow angle ϕ is independent of the angle of attack.

The strip theory procedure for the evaluation of aerodynamic characteristics of a rotating (spinning) body is as follows:

1. Divide the subject body into a convenient number of axial strips (say 25) of length dx
2. Then at a given strip, evaluate $\phi(x)$ and $q_{l,\mathrm{B}}(x)$ from equations (28) and (29)
3. From the following equations, evaluate the aerodynamic coefficients (per unit length) of each strip:

$$\Delta C_{N,\mathrm{B}} = \frac{C_1 (k_2 - k_1) \sin 2\alpha \cos\frac{\alpha}{2}}{S_{\mathrm{B,max}}} \frac{dS_\mathrm{B}}{dx} + \frac{\sin^2\alpha}{S_{\mathrm{B,max}}} \epsilon b_h C_{X,c} \quad (30)$$

$$\Delta C_{m,\mathrm{B}} = \Delta C_{N,\mathrm{B}} \frac{S_{\mathrm{B,max}}}{V_\mathrm{B}} (x_{cg} - x) \quad (31)$$

$$\Delta C_{Y,\mathrm{B}} = -\frac{C_1 (k_2 - k_1) \sin 2\beta \cos\frac{\beta}{2}}{S_{\mathrm{B,max}}} \frac{dS_\mathrm{B}}{dx} + \frac{\sin^2\beta}{S_{\mathrm{B,max}}} \epsilon b_h C_{Y,c} \quad (32)$$

$$\Delta C_{n,\mathrm{B}} = \Delta C_{Y,\mathrm{B}} \frac{S_{\mathrm{B,max}}}{V_\mathrm{B}} (x_{cg} - x) \quad (33)$$

4. Numerically integrate the following expressions to obtain the aerodynamic coefficients of a rotating (spinning) body:

$$C_{N,\mathrm{B}} = \int_{-l_2}^{l_1} \left[1 + \left(\frac{\Omega x \sin\alpha}{U_\infty}\right)^2\right] \times \Delta C_{N,\mathrm{B}}(x)\, dx \quad (34)$$

$$C_{m,\mathrm{B}} = \int_{-l_2}^{l_1} \left[1 + \left(\frac{\Omega x \sin\alpha}{U_\infty}\right)^2\right] \times \Delta C_{m,\mathrm{B}}(x)\, dx \quad (35)$$

$$C_{Y,\mathrm{B}} = \int_{-l_2}^{l_1} \left[1 + \left(\frac{\Omega x \sin\alpha}{U_\infty}\right)^2\right] \times \Delta C_{Y,\mathrm{B}}(x)\, dx \quad (36)$$

$$C_{n,\mathrm{B}} = \int_{-l_2}^{l_1} \left[1 + \left(\frac{\Omega x \sin\alpha}{U_\infty}\right)^2\right] \times \Delta C_{n,\mathrm{B}}(x)\, dx \quad (37)$$

$$C_{l,\mathrm{B}} = 0 \quad (38)$$

where l_1 and l_2 are the distances of the center of gravity from leading and trailing edges, respectively (fig. 10).

Rotational flow effects. Clarkson, Malcolm, and Chapman (ref. 28) have investigated the effect of angular velocity Ω on the aerodynamic forces and moments of certain autorotative flow mechanisms, one of which is the body with rectangular cross sections investigated by Polhamus (ref. 24). In their tests, the Reynolds numbers ranged from subcritical to supercritical, and the nondimensional spin rates based on the body length varied from -0.2 to 0.20. They observed that the autorotative flow mechanisms, once formed, get locked in and rotate with the body. The speed of rotation Ω apparently did not have a significant influence on the force and moment characteristics. Although the range of Ω considered in this work is much higher, for the lack of more comprehensive information, the rotational flow effects are ignored for the body.

Horizontal Tail Contribution

Strip theory calculations. Proceeding similar to the analysis of the wing, we obtain

$$C_{N,\mathrm{H}} = \frac{\eta_\mathrm{H} S_\mathrm{H}}{2 S_\mathrm{W} \tan\lambda_\mathrm{H}} \int_0^{\lambda_\mathrm{H}} (\Delta C_{N,\mathrm{H}R} + \Delta C_{N,\mathrm{H}L}) \times \sec^4\theta_\mathrm{H}\, d\theta_\mathrm{H} \quad (39)$$

$$C_{A,\mathrm{H}} = \frac{\eta_\mathrm{H} S_\mathrm{H}}{2 S_\mathrm{W} \tan\lambda_\mathrm{H}} \int_0^{\lambda_\mathrm{H}} (\Delta C_{A,\mathrm{H}R} + \Delta C_{A,\mathrm{H}L}) \times \sec^4\theta_\mathrm{H}\, d\theta_\mathrm{H} \quad (40)$$

$$C_{m,\mathrm{H}} = -C_{N,\mathrm{H}} (l_\mathrm{H}/\bar{c}_\mathrm{W}) \quad (41)$$

$$C_{l,\mathrm{H}} = \frac{\eta_\mathrm{H}}{4\tan^2\lambda_\mathrm{H}} \frac{S_\mathrm{H} b_\mathrm{H}}{S_\mathrm{W} b_\mathrm{W}} \int_0^{\lambda_\mathrm{H}} (\Delta C_{N,\mathrm{H}L} - \Delta C_{N,\mathrm{H}R}) \times \tan\theta_\mathrm{H} \sec^4\theta_\mathrm{H}\, d\theta_\mathrm{H} \quad (42)$$

$$C_{n,\mathrm{H}} = \frac{\eta_\mathrm{H}}{4\tan^2\lambda_\mathrm{H}} \frac{S_\mathrm{H} b_\mathrm{H}}{S_\mathrm{W} b_\mathrm{W}} \int_0^{\lambda_\mathrm{H}} (\Delta C_{A,\mathrm{H}R} - \Delta C_{A,\mathrm{H}L}) \times \tan\theta_\mathrm{H} \sec^4\theta_\mathrm{H}\, d\theta_\mathrm{H} \quad (43)$$

In equations (39) through (43), η_H is the horizontal tail efficiency. We assume that $\eta_\mathrm{H} = 1$ if the horizontal tail is clearly out of wing wake and $\eta_\mathrm{H} = 0$ if it is fully immersed in it (fig. 10). The wake of a stalled wing can be assumed to be bounded approximately by the straight lines extending from the leading and

trailing edges of the wing in the direction of the local flow (ref. 19).

Rotational flow effects. For the rotational flow effects on the horizontal tail, the procedure is similar to that for the wing calculations except the parameter $\sqrt{y_H^2 + l_H^2}$ replaces y for the distance of the strip from the center of rotation. In this case, the spanwise pressure variations leading to the rotational flow corrections are the y-components of the radial pressure gradient term. With this, we obtain the following relations for the horizontal tail with the x-component pressure forces arising because of the assumed radial pressure gradient being ignored:

$$C'_{N,H} = \frac{2S_H}{3S_W}\eta_H\omega^2 \tag{44}$$

$$C'_{l,H} = 0 \tag{45}$$

and for partial separation on either panel,

$$C'_{N,H} = \frac{\omega^2 S_H}{3S_W}\eta_H\left(1 + \eta^4_{stall}\right) \tag{46}$$

$$C'_{l,W} = -\frac{\omega^2\eta_H S_H b_H}{16S_W b_W}\left(1 - \eta^4_{stall}\right) \tag{47}$$

$$C'_{m,H} = -C'_{N,H}\left(\frac{l_H}{\bar{c}_W}\right) \tag{48}$$

Vertical Tail Contribution

Shielding effect. When stalled, the flow over the horizontal tail breaks off from its upper surface. This separated flow forms a region of dead air or wake on the lee side of the horizontal tail. On a spinning airplane, the wake flow of the outboard panel (the left panel in a right spin and the right panel in a left spin) of the horizontal tail is pushed towards the vertical tail (fig. 11). This results in the shielding of the vertical tail by the stalled stagnant fluid of the wake. Notice that the wake of the inboard panel is swept away and does not create any shielding over the vertical tail surface. Thus, only the outboard panel of the horizontal tail would be responsible for the shielding phenomenon.

In order to determine the aerodynamic forces and moments over the shielded vertical tail, the following assumptions are introduced:

1. The shielded area is a function of angle of attack and is independent of angular velocity in spin
2. The characteristics of the wake of the horizontal stabilizer can be approximated on the basis of experimental data on the two-dimensional flat-plate wake
3. The unshielded region of the vertical tail retains its effectiveness
4. The shielded area of the vertical tail is otherwise ineffective aerodynamically, except for the secondary flow effects discussed later

Modeling of two-dimensional flat-plate wake. At low Reynolds numbers, the mean flow in the wake, close to the flat plate, may be broadly divided into two regions (fig. 12(a)): (1) a recirculating region (ARB) bounded by the flat plate and the dividing streamline and (2) the external, irrotational flow. (See ref. 29.)

Arie and Rouse (ref. 30) find that the recirculation region (ARB) has an approximately elliptical shape and extends to a downstream distance of about 2.4 times the flat-plate chord (c_f). Abernathy (ref. 31) gives the following relations for a_1 and d_f (fig. 12(a)) of the recirculating region,

$$a_1 = 0.5c_f$$

$$d_f = \sqrt{2}c_f \sin\alpha \tag{49}$$

If these two sources of experimental data (refs. 30 and 31) are combined, the part of the wake behind the normal flat plate can be sketched as shown in figure 12(a). The major axis a of the ellipse turns out to be equal to $3.8c_f$, and the part of the ellipse ahead of the flat plate in the upstream direction (which is of no physical significance) has a length of $1.4c_f$. For application of this result to other angles of attack, we assume that the correlation with angle of attack given in equation (49) holds for other dimensions of the ellipse also. In other words,

$$a = 3.8c_f \sin\alpha \tag{50}$$

$$a_1 = 0.5c_f \sin\alpha \tag{51}$$

Thus for any given α, the geometrical parameters such as a, a_1, and d_f can be determined from equations (49) through (51), and the shape of the elliptical recirculating bubble can be sketched as shown schematically in figure 12(b). The shielded area (S_s) of the vertical tail corresponds to the shaded region.

The experimental results of Abernathy (ref. 31) based on which model is constructed are obtained for $\alpha \geq 40°$. Therefore, for $\alpha_{stall} < \alpha < 40°$, we use linear interpolation with the assumption that at $\alpha = \alpha_{stall}$, we get $S_s = 0$.

Calculation of aerodynamic coefficients. Here, a direct approach can be made instead of the strip theory because the vertical tail normally has a small aspect ratio. The sideslip and dynamic pressure at the vertical tail are given by

$$\beta_V = -\sin^{-1}\left\{\frac{2\omega\,(l_V/b_W)\sin\alpha}{\sqrt{1+[2\omega\,(l_V/b_W)\sin\alpha]^2}}\right\} \tag{52}$$

$$q_V = \frac{1}{2}\rho U_\infty^2 \eta_V \left[1+\left(\frac{2\omega l_V \sin\alpha}{b_W}\right)^2\right] \tag{53}$$

Under a partially shielded condition, we assume that the side force is given by

$$F_{Y,V} = q_V C^*_{Y,V} S_{V,\text{eff}} \tag{54}$$

$$F_{Y,V} = \frac{1}{2}\rho U_\infty^2 \eta_V \left[1+\left(\frac{2\omega l_V}{b_W}\sin\alpha\right)^2\right] C^*_{Y,V} S_{V,\text{eff}} \tag{55}$$

where $S_{V,\text{eff}} = S_V - S_s$ and $C^*_{Y,V}$ is the side-force coefficient of the vertical tail. Its determination is discussed later. Then

$$C_{Y,V} = \frac{F_{Y,V}}{qS_W} \tag{56}$$

$$C_{Y,V} = \left[1+\left(\frac{2\omega l_V}{b_W}\sin\alpha\right)^2\right]\eta_V \frac{S_{V,\text{eff}}}{S_W} C^*_{Y,V} \tag{57}$$

$$C_{l,V} = C_{Y,V}\frac{h_V}{b_W} \tag{58}$$

$$C_{n,V} = -C_{Y,V}\frac{l_V}{b_W} \tag{59}$$

where h_V is the vertical distance between the X-axis and the centroid of the unshielded area (taken positive upwards) of the vertical tail. In left spin, ω is negative, β_V is positive, and $C_{Y,V}$ is negative. As a result, $C_{l,V}$ and $C_{n,V}$ have opposite signs to those given in equations (58) and (59). Further, we assume

$$C_{N,V} = C_{m,V} = C_{A,V} = 0 \tag{60}$$

Secondary flow effects. The spin-tunnel rotary balance data (ref. 11) indicate the existence of a noticeable amount of damping in yaw (in excess of that predicted by eqs. (52) through (54)) at combined high angles of attack and spin rates. Such a fact, however, may never be noticed by the pilot in spin flight tests because the magnitude of such a damping effect may be small under spin flight test conditions. This development of the damping in yaw is an interesting phenomenon because it occurs when the vertical tail is assumed to have lost its effectiveness due to shielding. A detailed analysis of this problem which is characterized by extensive regions of separated and recirculating flows, in addition to the presence of the spin rate, is considered to be beyond the scope of this study. However, a physical explanation and an approximate mathematical model of this phenomenon, referred to here as the "secondary effect," is presented in the following discussion.

A simple way of visualizing this secondary effect is to assume that the airplane model is in a pure rotary motion, and the upward velocity in the spin tunnel is zero. Here, the "flat-plate" drag of the vertical tail generates a positive rolling moment and a negative (damping) yawing moment about the center-of-gravity of the airplane model. This phenomenon is analogous to the one referred to as secondary effect. The difference here is that the static pressure in the air surrounding the vertical tail is equal to p_w, the pressure in the wake of the horizontal tail.

On a spinning airplane, the mass of fluid in the wake has a relative transverse velocity equal to $\Omega l_V \sin\alpha$ with respect to the airplane and is assumed to impinge perpendicularly on the windward side of the vertical tail. As a result, a stagnation line forms over the windward side of the vertical tail about which the airstream divides itself and moves in opposite directions (fig. 13). The existence of such a flow pattern has been noticed in the full-scale flight tests conducted by the Langley Research Center.

As a consequence of this wake flow impingement, which is designated here as "secondary flow effect," a side force $F_{Y,V}$ (positive in right spin and negative in left spin) develops on the fin and generates an autorotative rolling moment and an antispin yawing moment (fig. 14). It is assumed that this wake flow impingement is limited to the shielded portion of the vertical tail. An estimation of the incremental aerodynamic forces and moments due to the secondary flow effect on the vertical tail is done as follows.

It is assumed that the wake flow impingement pattern is similar to that of the impingement of a uniform flow of radius r_j (fig. 15). (See ref. 32). For uniform flow impingement on a normal surface, the pressure and velocity along the stagnation streamline are related by Bernouli's equation,

$$p_s + \frac{1}{2}\rho U_s^2 = p_o \tag{61}$$

where p_s, U_s, and p_o are static pressure, velocity, and stagnation pressure. Also,

$$p_o = p + \frac{1}{2}\rho U^2 \tag{62}$$

where p and U are the pressure and velocity of the uniform impingement stream. Close to the stagnation point, we can assume (ref. 32)

$$U_s = \frac{r}{r_j} U \tag{63}$$

where r is the distance from the stagnation point measured along the surface streamline, and r_j is the radius of the impinging airstream. Substituting equations (62) and (63) into equation (61) results in the following equation, which gives the pressure distribution on the surface,

$$p_s = p + \frac{1}{2}\rho U^2 \left[1 - \left(\frac{r}{r_j}\right)^2\right] \tag{64}$$

Now for application of this model to wake flow impingement over the vertical tail, we have (fig. 13)

$$\left.\begin{aligned} U &= \Omega l_V \sin\alpha \\ p &= p_w \\ r_j &= c_V \\ r &= r_V \end{aligned}\right\} \tag{65}$$

Therefore, the pressure distribution along the chord of the vertical tail is given as

$$p_s = p_w + \frac{1}{2}\rho (\Omega l_V \sin\alpha)^2 \left[1 - \left(\frac{r_V}{c_V}\right)^2\right] \tag{66}$$

On the lee side of the vertical tail, pressure is assumed to be equal to p_w. Thus, the net side force on a strip with width Δr_V due to the pressure difference $(p_s - p_w)$ is given by

$$\Delta F'_{Y,V} = (p_s - p_w)\, b_V \Delta r_V \tag{67}$$

$$\Delta F'_{Y,V} = \frac{1}{2}\rho (\Omega l_V \sin\alpha)^2 \left[1 - (r_V/c_V)^2\right] b_V \Delta r_V \tag{68}$$

The total side-force coefficient on the vertical tail when it is fully shielded is

$$C'_{Y,V} = \frac{2b_V}{S_W}\left(\frac{\Omega l_V \sin\alpha}{U}\right)^2 \int_o^{c_V/2} \times \left[1 - \left(\frac{r_V}{c_V}\right)^2\right] dr_V \tag{69}$$

$$C'_{Y,V} = \frac{11 S_V}{3 S_W}\left(\frac{\omega l_V \sin\alpha}{b_W}\right)^2 \tag{70}$$

For a partially shielded condition, replace S_V by S_s to give

$$C'_{Y,V} = \frac{11 S_s}{3 S_W}\left(\frac{\omega l_V \sin\alpha}{b_W}\right)^2 \tag{71}$$

Then the rolling- and yawing-moment coefficients due to this secondary flow effect are (fig. 9(b))

$$\left.\begin{aligned} C'_{l,V} &= \pm C'_{Y,V} \frac{h'_V}{b_W} \\ C'_{n,V} &= \mp C'_{Y,V} \frac{l_V}{b_W} \end{aligned}\right\} \tag{72}$$

For right spins, $C'_{l,V}$ is positive and $C'_{n,V}$ is negative; for left spins, $C'_{l,V}$ is negative and $C'_{n,V}$ is positive. Thus, from equations (70) and (72), we observe that the magnitudes of the side-force, rolling-moment, and yawing-moment coefficients due to the secondary flow effect on the vertical tail will assume significance at combined large angles of attack and spin rates.

Total Airplane

Expressions (eqs. (73) through (80)) are presented for determining the aerodynamic coefficients of various combinations of airplane components based on the calculations in the previous section. The format for the presentation of results follows the manner in which the rotary balance test data are reported in references 11 and 12. It may be noted that the axial-force data are not available in reference 11. Since the axial force does not play any significant role in equilibrium spin, it is not considered. However, for complete airplane configurations, the axial-force data are available in reference 12. Therefore, in the present paper, results on the axial force are limited to airplane configurations only. The prime ($'$) denotes the rotational or secondary flow effect.

Body B configuration:

$$\left.\begin{aligned} C_N &= C_{N,B} \\ C_Y &= C_{Y,B} \\ C_m &= C_{m,B} \\ C_n &= C_{n,B} \end{aligned}\right\} \tag{73}$$

BW configuration:

$$\left.\begin{aligned} C_N &= C_{N,\mathrm{B}} + C_{N,\mathrm{W}} + C'_{N,\mathrm{W}} \\ C_Y &= C_{Y,\mathrm{B}} \\ C_m &= C_{m,\mathrm{B}} + C_{m,\mathrm{W}} + C'_{m,\mathrm{W}} \\ C_l &= C_{l,\mathrm{W}} + C'_{l,\mathrm{W}} \\ C_n &= C_{n,\mathrm{B}} + C_{n,\mathrm{W}} \end{aligned}\right\} \quad (74)$$

BH configuration:

$$\left.\begin{aligned} C_N &= C_{N,\mathrm{B}} + C_{N,\mathrm{H}} + C'_{N,\mathrm{H}} \\ C_Y &= C_{Y,\mathrm{B}} \\ C_m &= C_{m,\mathrm{B}} + C_{m,\mathrm{H}} + C'_{m\mathrm{H}} \\ C_l &= C_{l,\mathrm{H}} + C'_{l,\mathrm{H}} \\ C_n &= C_{n,\mathrm{B}} + C_{n,\mathrm{H}} \end{aligned}\right\} \quad (75)$$

BV configuration:

$$\left.\begin{aligned} C_N &= C_{N,\mathrm{B}} \\ C_Y &= C_{Y,\mathrm{B}} + C_{Y,\mathrm{V}} \\ C_m &= C_{m,\mathrm{B}} \\ C_l &= C_{l,\mathrm{V}} \\ C_n &= C_{n,\mathrm{B}} + C_{n,\mathrm{V}} \end{aligned}\right\} \quad (76)$$

BWH configuration:

$$\left.\begin{aligned} C_N &= C_{N,\mathrm{B}} + C_{N,\mathrm{W}} + C'_{N,\mathrm{W}} + C_{N,\mathrm{H}} + C'_{N,\mathrm{H}} \\ C_Y &= C_{Y,\mathrm{B}} \\ C_m &= C_{m,\mathrm{B}} + C_{m,\mathrm{W}} + C'_{m,\mathrm{W}} + C_{m,\mathrm{H}} + C'_{m,\mathrm{H}} \\ C_l &= C_{l,\mathrm{W}} + C'_{l,\mathrm{W}} + C_{l,\mathrm{H}} + C'_{l,\mathrm{H}} \\ C_n &= C_{n,\mathrm{B}} + C_{n,\mathrm{W}} + C_{n,\mathrm{H}} \end{aligned}\right\} \quad (77)$$

BWV configuration:

$$\left.\begin{aligned} C_N &= C_{N,\mathrm{B}} + C_{N,\mathrm{W}} + C'_{N,\mathrm{W}} \\ C_Y &= C_{Y,\mathrm{B}} + C_{Y,\mathrm{V}} \\ C_m &= C_{m,\mathrm{B}} + C_{m,\mathrm{W}} + C'_{m,\mathrm{W}} \\ C_l &= C_{l,\mathrm{W}} + C'_{l,\mathrm{W}} + C_{l,\mathrm{V}} \\ C_n &= C_{n,\mathrm{B}} + C_{n,\mathrm{W}} + C_{n,\mathrm{V}} \end{aligned}\right\} \quad (78)$$

BHV configuration:

$$\left.\begin{aligned} C_N &= C_{N,\mathrm{B}} + C_{N,\mathrm{H}} + C'_{N,\mathrm{H}} \\ C_Y &= C_{Y,\mathrm{B}} + C_{Y,\mathrm{V}} + C'_{Y,\mathrm{V}} \\ C_m &= C_{m,\mathrm{B}} + C_{m,\mathrm{H}} + C'_{m,\mathrm{H}} \\ C_l &= C_{l,\mathrm{H}} + C'_{l,\mathrm{H}} + C_{l,\mathrm{V}} + C'_{l,\mathrm{V}} \\ C_n &= C_{n,\mathrm{B}} + C_{n,\mathrm{H}} + C_{n,\mathrm{V}} + C'_{n,\mathrm{V}} \end{aligned}\right\} \quad (79)$$

BWHV configuration:

$$\left.\begin{aligned} C_N &= C_{N,\mathrm{B}} + C_{N,\mathrm{W}} + C'_{N,\mathrm{W}} + C_{N,\mathrm{H}} + C'_{N,\mathrm{H}} \\ C_A &= C_{A,\mathrm{B}} + C_{A,\mathrm{W}} + C_{A,\mathrm{H}} \\ C_Y &= C_{Y,\mathrm{B}} + C_{Y,\mathrm{W}} + C_{Y,\mathrm{H}} + C_{Y,\mathrm{V}} + C'_{Y,\mathrm{V}} \\ C_m &= C_{m,\mathrm{B}} + C_{m,\mathrm{W}} + C'_{m,\mathrm{W}} + C_{m,\mathrm{H}} + C'_{m,\mathrm{H}} \\ C_l &= C_{l,\mathrm{W}} + C'_{l,\mathrm{W}} + C_{l,\mathrm{H}} + C'_{l,\mathrm{H}} + C_{l,\mathrm{V}} + C'_{l,\mathrm{V}} \\ C_n &= C_{n,\mathrm{B}} + C_{n,\mathrm{W}} + C_{n,\mathrm{H}} + C_{n,\mathrm{V}} + C'_{n,\mathrm{V}} \end{aligned}\right\} \quad (80)$$

Application

The semiempirical aerodynamic analysis of the spinning airplane developed herein has been applied to a light, general aviation, spin research airplane, called "model A," which is extensively studied in the stall/spin research program of the Langley Research Center (refs. 9 through 13).

The dimensional characteristics of the full-scale model A airplane are presented in table I. A three-view drawing of the basic airplane is shown in figure 16, and the details of tails 3, 4, and 5 for which the calculations are performed are given in figure 17. The tail configuration of the basic airplane is designated as tail 4, and wing section is the modified NACA 64_2-415 airfoil. The major difference in various tail configurations is the location of the horizontal tail with respect to the vertical tail. Among these

configurations, tail 3 produces a maximum shielding effect, and tail 5 (T-tail) is not expected to produce any shielding. These tail configurations are selected to examine the validity of the shielding model developed earlier.

Input Data

In the semiempirical theory of a spinning airplane presented, several empirical constants are embedded. In the following discussion, these constants are evaluated for the subject airplane model.

Wing. The empirical constants are $C_{L,l}$, $C_{D,l}$, (or $C_{N,l}$ and $C_{A,l}$) and $\bar{x}_{cp}$. In reference 10, the static wind-tunnel test data are presented for the body B and the wing-body BW combinations. Ignoring wing-body interference, the wing characteristics are derived by subtracting the data for the body from the data for the wing-body combination. The experimental center-of-pressure $\bar{x}_{cp}$ data are taken from reference 33. These derived data are presented in figure 18.

Body. The empirical constants to be evaluated for the subject body are C_1, $C_{X,c}$, and $C_{Y,c}$. The constant C_1 depends on the body length and cross-sectional shape, and $C_{X,c}$ and $C_{Y,c}$ are aerodynamic parameters which depend on the cross-sectional shape, cross-flow angle ϕ, and the Reynolds number. The range of cross-flow angle ϕ over which the experimental data for $C_{X,c}$ and $C_{Y,c}$ are required is shown in figure 19. For rotary (spin) conditions, the maximum value of ϕ is around 40° for all angles of attack. However, in static calculations, larger values of ϕ (up to approximately 80°) are encountered.

The coefficients $C_{X,c}$ and $C_{Y,c}$ correspond to a two-dimensional cylinder which has a constant cross section. However, the actual cross-sectional shape of the subject body varies along the length as shown in figure 20. Therefore, we have to idealize the body of model A, as the one having the same values of S_B and dS_B/dx as the subject body (fig. 21) but a constant cross-sectional shape. For this purpose, we refer to the study of Bihrle and Bowman (ref. 23) who tested various bodies similar to that of the model A airplane. In their tests, the aft body shape was fixed, and the cross-sectional shape of the forward part was varied. They observed that the cross-sectional shape of the nose did not have significant influence on the autorotational characteristics of the body. This observation may be attributed to the short moment arm of the forward part of the body. However, these comments are specific to this configuration and may not be valid for other bodies. Thus, we assume that the idealized constant cross-sectional shape of the subject body is that of the aft portion, which happens to be a square section with sharp bottom corners and a well-rounded top surface as shown in figure 22. For this idealized section, the empirical constants are evaluated as follows:

C_1: For a square section with sharp corners, Jorgensen (ref. 27) suggests a value of 1.19, which has been used in the present calculations.

$C_{X,c}$: Wind-tunnel test data are not available for the idealized cross-sectional shape. Perhaps the closest data available are those reported by Polhamus (ref. 24) for a square section with a corner radius of 8 percent (fig. 8). With the assumption that the nature of windward corners has the primary influence on the cross-flow characteristics compared with lee-side corners, we use these data in the present calculations.

$C_{Y,c}$: The required test data are not available. The generation of these data is discussed in the following paragraphs:

Side force—In reference 10, the three-dimensional static side-force data on the isolated body of the model A airplane are presented at various angles of attack between 0° to 90° and sideslip angle of 0° to 30°. With the use of equation (27), the variation of side force with cross-flow angle ϕ is obtained as shown in figure 23. The test data corresponding to high angle of attack ($\alpha > 70°$) are well correlated because the cross flow is very much independent of the axial flow at these angles of attack. However, the large scatter in the data points corresponding to tests at lower angles of attack is because of the strong interdependence between axial and cross flows. Therefore, a meanline is drawn through the scattered data to approximate the variation of $C_{Y,c}$ at high α with ϕ as shown in figure 23. These correlated test data are designated as "$C_{Y,c}$(B)."

Square cylinder test data—A cross-sectional shape which is close to that of an idealized body section and for which comprehensive two-dimensional test data are available is the square section having an 8-percent corner radius (ref. 24), which has been discussed earlier. The values of $C_{X,c}$ and $C_{Y,c}$ for this body are nearly independent of the Reynolds number (ref. 24). However, for the present idealized cross section, the cross-flow aerodynamic forces can have a dependence on the Reynolds number on account of the rounded top surface

(fig. 24). These experimental data are designated as "$C_{Y,c}$(SC)."

These two sets of data are used in the present calculations as follows:

Static aerodynamic coefficients:

$\alpha < 70°$, $C_{X,c}$ and $C_{Y,c}$(SC)
$\alpha > 70°$, $C_{X,c}$ and $C_{Y,c}$(B)

Rotary aerodynamics:

All angles of attack, $C_{X,c}$ and $C_{Y,c}$(B)

Horizontal tail. The empirical constants required are $C_{N,\mathrm{H}}$, $C_{A,\mathrm{H}}$, and $\bar{x}_{\mathrm{cp,H}}$. These coefficients are assumed to be identical to those of the wing as given in figure 18. It was assumed that the differences in the aspect ratio and airfoil shape do not significantly affect these parameters. The determination of η_{H}, the tail efficiency parameter, is determined graphically by considering whether the tail is submerged ($\eta_{\mathrm{H}} = 0$) or falls out of the wing wake ($\eta_{\mathrm{H}} = 1$) as illustrated in figure 25. Tails 3 and 4 are out of the wing wake for $\alpha > 20°$. However, the T-tail (tail 5) gets immersed in the wing wake around $\alpha = 20°$ and can be assumed to fall out of wake for $\alpha \geq 30°$.

Vertical tail. The empirical constant $C^*_{Y,\mathrm{V}}$ appearing in equations (54), (55), and (57) can be evaluated with Datcom methods (ref. 19) for sideslip angles below stall. Beyond stall, assuming that the low aspect ratio vertical tail behaves like a square plate, Hoerner's data (ref. 20) can be used for the vertical tail operating beyond stall in sideslip. Based on these two sources of data, the side-force data for the vertical tail are generated as shown in figure 26.

Figure 27 presents the schematics of the graphical determination of the shielded area of the vertical tail at various angles of attack. The calculated variation of S_s with α for tails 3 and 4 is shown in figure 28. It may be noted that $S_s = 0$ for tail 5 (T-tail configuration).

Presentation of Results

The static longitudinal coefficients of the body (B) are shown in figure 29, and the lateral aerodynamic coefficients are shown in figures 30 and 31. The static side-force and yawing-moment characteristics of the wing-body (BW) combination at selected angles of attack are given in figure 32. The predicted static side-force and yawing-moment coefficients of V and BHV configurations, which are based on the present shielding model, are given in figure 33 along with static wind-tunnel data (ref. 10).

The steady-state rotary (spin) aerodynamic characteristics of basic airplane components are presented in tables II through VI. With these values and equations (73) through (80), the aerodynamic coefficients for any desired configuration can be obtained. These results are plotted in figures 34 to 44, along with corresponding spin-tunnel rotary balance test data (refs. 11 and 12). Such a detailed, piece-by-piece comparison helps to bring out the capabilities and limitations of the present approach. In figures 45 to 49, the aerodynamic coefficients are presented for different tail configurations and at angles of attack around which equilibrium spin modes have been recorded in free spinning tests in the spin tunnel (ref. 14). These results are also compared with the corresponding spin-tunnel rotary balance data (ref. 12).

Discussion

Static Aerodynamic Characteristics

This discussion is limited to body and vertical tail because the static aerodynamic coefficients for other components (wing and horizontal tail) are directly taken from the wind-tunnel test data (ref. 10) and not calculated here.

Body. The predicted value of C_D (fig. 29) agrees well with static wind-tunnel test data up to $\alpha = 60°$, but for $\alpha > 60°$, the present value is on the higher side. At $\alpha = 90°$, the difference between the two results is about 15 percent.

C_L. Predicted values of C_L are in fair agreement with experimental data (fig. 29) for low ($\alpha \leq 20°$) and high ($\alpha \geq 70°$) angles of attack. For $20° < \alpha < 70°$, the significant differences exist. The maximum value of C_L and the angle of attack at which this occurs are fairly well predicted.

C_m. The basic static stability trend is captured by the present approach; that is, the static instability up to $\alpha = 30°$ and subsequent stability are predicted. However, significant differences in magnitudes are noted to exist.

C_Y. The side-force coefficient C_Y has an interesting variation with α and β. At low angles of attack, for example, $\alpha \leq 20°$, the side force is negative at all values of β (fig. 30) and is reasonably well-predicted by the present theory. At higher angles of attack with the exceptions of 30° and 40°, the side force is positive and changes sign for higher values of β. Although calculations pick up this trend well, significant differences exist between theory and experimental data.

C_n. At all angles of attack, C_n is generally negative for the range of β shown in figure 31. According to static wind-tunnel data, the body is directionally unstable up to $\beta = 15°$ to 20° and becomes stable subsequently for higher values of β. This trend is captured by the present method, particularly at high angles of attack. As before, significant differences in magnitudes exist.

BW ***configuration.*** In figure 32, the present calculations (ignoring wing-body interference effect) are compared with static wind-tunnel test data (ref. 10). Also included in this figure are the experimental data for the body (B) for relative comparison. It is observed that the significant interference effect exists between wing and body.

BHV ***configuration.*** From figures 33 and 34, we observe that the predicted values of C_Y based on the shielding effect model are in fair agreement with static wind-tunnel test data (ref. 10). However, the calculated values of C_n differ considerably from the static wind-tunnel data (ref. 10) particularly at high angles of attack. At these angles of attack, the vertical tail has lost most of its effectiveness. Therefore, this discrepancy in C_n could be due to the aft body-tail interference effect (not modeled here) which may alter the side force locally without affecting overall side force much but changes the yawing moment significantly on account of its large moment arm.

Rotary Aerodynamic Characteristics

Body (B) configuration. From figure 34, it is observed that large differences exist in magnitudes between the present result and rotary balance test data (ref. 11). Although the basic autorotational tendency ($C_n > 0$ for $\omega > 0$) of the body is predicted, the autorotational speeds (value of ω when $C_n = 0$) are not well predicted.

BW ***configuration.*** The approach of strip theory combined with McCormick's rotational flow model (ref. 13) gives a good result in comparison with rotary balance test data for C_N, C_l, and C_m (fig. 35). The increments to C_N, C_l, and C_m calculated on the basis of McCormick's rotational flow model are of considerable magnitude at high spin rates. However, significant differences between the present results and rotary balance test data exist, particularly for side-force and yawing-moment coefficients.

BH ***configuration.*** The variation of C_Y, C_N, and C_m follows the earlier trends (fig. 36). For the BH configuration, the calculated rolling-moment coefficient is very small (e.g., $C_l \approx 0$ for $\alpha = 90°$). However, the rotary balance data indicate the existence of substantial rolling moment (autorotative type) at $\alpha = 60°$ and 90°, which is far in excess of that given by the strip theory.

In figure 36, for the coefficients C_Y and C_n, the rotary balance test data for the body alone are also superposed. Observe that in relative comparison, the yawing-moment coefficient for the BH configuration is significantly different from the body-alone values. The strip theory contribution of the horizontal tail to C_Y and C_n is very small. Therefore, the significant change in C_n when both the body and horizontal tail are together must be on account of the aft body–horizontal tail interference as noted by earlier authors (refs. 22 and 23) and not considered here.

BV ***configuration.*** In figure 37, the discrepancies in C_l and C_n for the BV configuration are less severe compared with those for the BH configuration. The interference effect between the aft body–vertical tail is also significant as seen by a relative comparison for BV and B data for C_Y and C_n. Although the main trend of results is consistent with rotary balance tests, differences in terms of magnitude still exist.

BWH ***configuration.*** The coefficients C_N, C_l, and C_m (fig. 38) follow the trends noted earlier. However, the predicted side-force and yawing-moment coefficients differ appreciably from the rotary balance test data. Contributions of wing and horizontal tails to side-force and yawing-moment coefficients are small in comparison to that of the body.

In figure 38, the rotary balance test data for C_Y and C_n for B, BW, and BH configurations are also included along with the data for the BWH configuration. From a relative comparison of these values, it is clear that significant interference exists between wing, body, and horizontal tail surfaces. As stated earlier, these interference effects are not modeled here. The magnitudes of interference effects are so appreciable that the presence of wing and horizontal tails has masked the basic autorotational tendency of the body.

BWV ***configuration.*** The basic trends of most of the experimental rotary aerodynamic coefficients are predicted by the present method (fig. 39). Differences in magnitudes do exist. The disagreement in C_Y suggests that there is an appreciable interference effect (between body, wing, and vertical tail) as noted previously.

BHV ***configuration.*** The predicted trends of C_N, C_m, and C_l agree with those given by rotary balance data (figs. 40 and 41). The calculated side-force and yawing-moment coefficients differ considerably from the rotary balance test data. This phenomenon is attributed to the aft body–tail interference effect noted earlier.

BWHV ***configuration.*** The present theory predicts the characteristics of the total airplane reasonably well at low and moderate angles of attack and low spin rates. The differences in magnitudes become significant at high angles of attack and spin rates, particularly for side-force, rolling-, and yawing-moment coefficients.

Prediction of Equilibrium Spin Modes

For the spin research airplane model A, the free spinning model tests (ref. 14) have indicated the existence of steady-state (equilibrium) spin modes as follows:

Tail 3:

(1) Moderately steep spin mode, $\alpha = 50°$ and $\omega = 0.33$
(2) Flat spin mode, $\alpha = 80°$ and $\omega = 0.62$

Tail 4:

(1) Moderately steep spin mode, $\alpha = 35°$ and $\omega = 0.22$
(2) Flat spin mode, $\alpha = 77°$ and $\omega = 0.92$

Tail 5:

Moderately steep spin mode, $\alpha = 41°$ and $\omega = 0.234$

In figures 45 to 49, the predicted rotary aerodynamic coefficients for these spin modes are presented and are compared with corresponding spin-tunnel rotary balance test data (ref. 12). In free spinning model tests, prospin controls are employed. Since the deflection of control surfaces is not considered in the present analysis, the spin-tunnel rotary balance test data included in figures 35 to 39 are also taken for zero control surface deflections. This kind of comparison is not a true indication of the real situation but still is a good representative of the aerodynamic parameters dictating the spin modes.

From figures 45, 47, and 49, which correspond to steep or moderately steep spin modes for tails 3, 4, and 5, respectively, it is observed that for most of the coefficients there is a fair agreement between the present theory and spin-tunnel rotary balance test data (ref. 12), around the values of ω where the steady-state spin modes occur. However, for flat spin modes where the reduced spin rates are high (figs. 46 and 48), the discrepancies in the estimation of C_Y and C_n are large and should be of concern. Therefore, the present theory needs further development, particularly with respect to C_Y and C_n for satisfactory prediction of flat spin modes.

Concluding Remarks

The aerodynamics of a spinning airplane is complex and is dominated by extensive regions of separated flow fields, mutual interferences between aerodynamic and control surfaces, and the complex effect of spin rate. As a result, the aerodynamic coefficients of a spinning airplane display a high degree of nonlinearity with angle of attack and spin rate; this makes the conventional approach based on stability and control derivatives invalid for the problem of the spinning airplane. This complex problem is still not amenable to computational fluid dynamic methods. The present theory which is semiempirical in nature and is developed on the basis of synthesis of the available experimental data from various sources is an attempt to fill the void. In this way, this work represents a first, unified approach to the problem of estimating the aerodynamic characteristics of a light spinning airplane. In the course of this investigation, it was realized that several lacunae exist in literature, and this problem, which is of vital importance to general aviation, needs immediate attention to generate an experimental data base, which can give more insights and help in the development of a theoretical model. In view of such a situation, the present theory had to be based on many speculations and heuristic assumptions to put all the pieces together. The results and experience of this study are summarized as follows along with the recommendations for future work.

The strip theory approach is capable of predicting the aerodynamic characteristics of a steadily spinning airplane. With appropriate input data to account for the effects of angular velocity in spin, its accuracy is significantly enhanced. The present semiempirical theory is found to be capable of providing reasonable estimates of the aerodynamic coefficients of a spinning airplane for steep and moderately steep spin conditions. However, the theory needs further development for successful application to flat spin problems.

At high angles of attack α, the rotary balance test data indicate that the spin rate has a strong influence on normal-force, pitching-moment, and rolling-moment coefficients of a spinning airplane. In comparison, the predictions based on strip theory with static wind-tunnel data as input differ significantly from these test data. The physical mechanism responsible for this phenomenon is not clear at this

stage as there is no experimental data base which records flow pattern or pressure distributions over a spinning wing and throws some light on the physics of the flow.

No validated aerodynamic models for stalled spinning wings exist. McCormick (NASA CR-165680) hypothesizes incremental changes in the aerodynamic forces and moments caused by the spanwise pressure gradient on the lee side of the wing due to centrifugal force. Although the inclusion of the increments improves the comparison of strip theory with experimental test data, there is a dearth of evidence necessary to validate the underlying assumptions. Local flow measurements of stalled spinning wings are needed to enable the formulation of a comprehensive theory.

A semiempirical method is developed for the prediction of body aerodynamic characteristics at high angles of attack and sideslip. This approach gives the required static input data in the strip theory for the spinning airplane.

All the mutual interference effects between various components are not considered except the shielding of vertical tail surface by the wake of horizontal tail. A simple procedure for estimating the shielded area of the vertical tail is presented. Increments to aerodynamic coefficients on account of the secondary flow within the shielded part of the vertical tail are estimated by a simple analysis of wake flow impingement on the vertical tail.

Some of the mutual interference effects between body, wing, and tail surfaces of a spinning airplane, which are not considered herein, are found to be large and significant. Of particular concern is the interference effect between aft body and horizontal tail surfaces, which can have a strong influence on side force and yawing moments. Further studies are necessary in this direction to gain a better understanding of these complex effects.

It is recommended that further research be initiated to study the aerodynamics of the spinning airplane at high angles of attack and spin rate. Flow visualization and pressure distribution measurements should be carried out along with direct force and moment coefficients so as to increase the process of understanding and development of a comprehensive theory for a spinning light airplane.

NASA Langley Research Center
Hampton, VA 23665-5225
November 5, 1987

References

1. Silver, Brent W.: Statistical Analysis of General Aviation Stall Spin Accidents. [Preprint] 760480, Soc. of Automotive Engineers, Apr. 1976.
2. Dickinson, B.: *Aircraft Stability and Control for Pilots and Engineers.* Sir Isaac Pitman & Sons Ltd., c.1968.
3. Glauert, H.: *The Investigation of the Spin of an Aeroplane.* R. & M. No. 618, British Advisory Committee for Aeronautics, June 1919.
4. Gates, S. B.; and Bryant, L. W.: *The Spinning of Aeroplanes.* R. & M. No. 1001, British Aeronautical Research Council, 1927.
5. Wykes, John H.; Casteel, Gilbert R.; and Collins, Richard A.: *An Analytical Study of the Dynamics of Spinning Aircraft. Part I—Flight Test Data Analyses and Spin Calculations.* WADC Tech. Rep. 58-381, Pt. I, U.S. Air Force, Dec. 1958. (Available from DTIC as AD 203 788.)
6. Bamber, M. J.; and House, R. O.: *Spinning Characteristics of the XN2Y-1 Airplane Obtained From the Spinning Balance and Compared With Results From the Spinning Tunnel and From Flight Tests.* NACA Rep. 607, 1937.
7. Bihrle, William, Jr.; and Barnhart, Billy: Spin Prediction Techniques. *A Collection of Technical Papers—AIAA Atmospheric Flight Mechanics Conference,* Aug. 1980, pp. 76–82. (Available as AIAA-80-1564.)
8. Tischler, M. B.; and Barlow, J. B.: Determination of the Spin and Recovery Characteristics of a General Aviation Design. *J. Aircr.*, vol. 18, no. 4, Apr. 1981, pp. 238–244.
9. Himmelskamp, H.: *Profile Investigations on a Rotating Airscrew.* Rep. & Transl. No. 832, British Ministry of Aircraft Products Volkenrode, Sept. 1, 1947.
10. Bihrle, William, Jr.; Barnhart, Billy; and Pantason, Paul: *Static Aerodynamic Characteristics of a Typical Single-Engine Low-Wing General Aviation Design for an Angle-of-Attack Range of -8° to 90°.* NASA CR-2971, 1978.
11. Bihrle, William, Jr.; Hultberg, Randy S.; and Mulcay, William: *Rotary Balance Data for a Typical Single-Engine Low-Wing General Aviation Design for an Angle-of-Attack Range of 30° to 90°.* NASA CR-2972, 1978.
12. Hultberg, Randy S.; and Mulcay, William: *Rotary Balance Data for a Typical Single-Engine General Aviation Design for an Angle-of-Attack Range of 8° to 90°. I—Low-Wing Model A.* NASA CR-3100, 1980.
13. McCormick, Barnes W.: *The Prediction of Normal Force and Rolling Moment Coefficients for a Spinning Wing.* NASA CR-165680, 1981.
14. Burk, Sanger M., Jr.; Bowman, James S., Jr.; and White, William L.: *Spin-Tunnel Investigation of the Spinning Characteristics of Typical Single-Engine General Aviation Airplane Designs. I—Low-Wing Model A: Effects of Tail Configurations.* NASA TP-1009, 1977.
15. Staff, Langley Research Center: *Exploratory Study of the Effects of Wing-Leading-Edge Modifications on the Stall/Spin Behavior of a Light General Aviation Airplane.* NASA TP-1589, 1979.
16. Pamadi, Bandu N.; and Taylor, Lawrence W., Jr.: An Estimation of Aerodynamic Forces and Moments on an

Airplane Model Under Steady State Spin Conditions. AIAA-82-1311, Aug. 1982.
17. Pamadi, Bandu N.; and Taylor, Lawrence W., Jr.: An Evaluation of Aerodynamics Modeling of Spinning Light Airplanes. AIAA-83-0368, Jan. 1983.
18. Poppen, William A., Jr.: *A Method for Estimating the Rolling Moment Due to Spin Rate for Arbitrary Planform Wings.* NASA TM-86365, 1985.
19. *USAF Stability and Control Datcom.* Contracts AF33(616)-6460 and F33615-76-C-3061, McDonnell Douglas Corp., Oct. 1960. (Revis. Apr. 1978.)
20. Hoerner, Sighard F.: *Fluid-Dynamic Drag.* Hoerner Fluid Dynamics (Brick Town, N.J.), c.1965.
21. Critzos, Chris C.; Heyson, Harry H.; and Boswinkle, Robert W., Jr.: *Aerodynamic Characteristics of NACA 0012 Airfoil Section at Angles of Attack From 0° to 180°.* NACA TN 3361, 1955.
22. Beaurain, L. (Leo Kanner Associates, transl.): *General Study of Light Plane Spin, Aft Fuselage Geometry*, Part 1. NASA TT F-17,446, 1977.
23. Bihrle, William, Jr.; and Bowman, James S., Jr.: Influence of Wing, Fuselage, and Tail Design on Rotational Flow Aerodynamics Beyond Maximum Lift. *J. Aircr.*, vol. 18, no. 11, Nov. 1981, pp. 920–925.
24. Polhamus, Edward C.: *Effect of Flow Incidence and Reynolds Number on Low-Speed Aerodynamic Characteristics of Several Noncircular Cylinders With Applications to Directional Stability and Spinning.* NASA TR R-29, 1959. (Supersedes NACA TN 4176.)
25. Allen, H. Julian: *Estimation of the Forces and Moments Acting on Inclined Bodies of Revolution of High Fineness Ratio.* NACA RM A9I26, 1949.
26. Munk, Max M.: *The Aerodynamic Forces on Airship Hulls.* NACA Rep. 184, 1924.
27. Jorgensen, Leland Howard: *Prediction of Static Aerodynamic Characteristics for Slender Bodies Alone and With Lifting Surfaces to Very High Angles of Attack.* NASA TR R-474, 1977.
28. Clarkson, M. H.; Malcolm, G. N.; and Chapman, G. T.: Experimental Determination of Post-Stall Rotary Derivatives for Airplane-Like Configurations at Several Reynolds Numbers. AIAA Paper 75-171, Jan. 1975.
29. Maull, D. J.: Mechanisms of Two and Three-Dimensional Base Drag. *Aerodynamic Drag Mechanisms of Bluff Bodies and Road Vehicles*, Gino Sovran, Thomas Morel, and William T. Mason, Jr., eds., Plenum Press, 1978, pp. 137–159.
30. Arie, Mikio; and Rouse, Hunter: Experiments on Two-Dimensional Flow Over a Normal Wall. *J. Fluid Mech.*, vol. 1, pt. 2, July 1956, pp. 129–141.
31. Abernathy, F. H.: Flow Over an Inclined Plate. *J. Basic Eng.*, vol. 84, no. 3, Sept. 1962, pp. 380–388.
32. Schlichting, Hermann (J. Kestin, transl.): *Boundary-Layer Theory*, Sixth ed. McGraw-Hill Book Co., 1968.
33. Saini, Jugal Kishore: An Experimental Investigation of the Effects of Leading Edge Modifications on the Post-Stall Characteristics of an NACA 0015 Wing. M.S. Thesis, Univ. of Maryland, Aug. 1979.

Table I. Dimensional Characteristics of Full-Scale Model A Airplane

Wing:	
Span, m	7.46
Area, m^2	9.11
Root chord, m	1.22
Tip chord, m	1.22
Mean aerodynamic chord, m	1.22
Aspect ratio	6.10
Dihedral, deg	5.0
Incidence at—	
Root, deg	5.0
Tip, deg	5.0
Airfoil section	Modified NACA 64_2-415
Fuselage:	
Overall length, m	5.39
Distance from leading edge to airplane center of gravity, m	1.91
Maximum width, m	1.09
Maximum height, m	1.15
Maximum cross-sectional area, m^2	1.16
Volume, m^3	3.48
Horizontal tail:	
Span, m	2.34
Incidence, deg	3.0
Root chord, m	1.10
Tip chord, m	0.51
Mean aerodynamic chord, m	0.84
Aspect ratio	2.91
Tail length (distance of center of gravity to $0.25\bar{c}_H$), l_H, for tail 3, m	3.48
Airfoil section	NACA 65_1-012
Vertical tail:	
Span, m	1.25
Root chord, m	1.10
Tip chord, m	0.51
Mean aerodynamic chord, m	0.84
Aspect ratio	1.55
Tail length (distance from center of gravity to $0.25\bar{c}_V$), l_V, for tail 3, m	3.48
Airfoil section	NACA 65_1-012

Table II. Side-Force Coefficients of Airplane Components

ω	$C_{Y,B}$	Tail 3		Tail 4		Tail 5
		$C_{Y,V}$	$C'_{Y,V}$	$C_{Y,V}$	$C'_{Y,V}$	$C_{Y,V}$
$\alpha = 30°$						
0	0	0	0	0	0	0
0.10	−0.010	0.009	0	0.015	0	0.015
0.20	−0.023	0.031	0	0.047	0	0.051
0.30	−0.036	0.034	0.001	0.053	0	0.056
0.40	−0.051	0.038	0.001	0.059	0	0.062
0.50	−0.066	0.041	0.001	0.065	0	0.069
0.60	−0.078	0.046	0.002	0.072	0.001	0.075
0.70	−0.089	0.050	0.003	0.079	0.001	0.082
0.80	−0.098	0.054	0.004	0.087	0.001	0.090
0.90	−0.106	0.059	0.005	0.095	0.001	0.098
$\alpha = 45°$						
0	0	0	0	0	0	0
0.10	−0.015	0.006	0	0.019	0	0.022
0.20	−0.036	0.016	0.001	0.044	0	0.055
0.30	−0.056	0.019	0.002	0.052	0.001	0.064
0.40	−0.080	0.021	0.003	0.060	0.001	0.073
0.50	−0.105	0.024	0.005	0.069	0.002	0.083
0.60	−0.125	0.027	0.008	0.078	0.003	0.094
0.70	−0.140	0.031	0.010	0.089	0.004	0.106
0.80	−0.165	0.034	0.013	0.101	0.005	0.118
0.90	−0.170	0.038	0.017	0.114	0.006	0.132
$\alpha = 60°$						
0	0	0	0	0	0	0
0.10	−0.020	0.001	0	0.017	0	0.027
0.20	−0.047	0.003	0.002	0.036	0.001	0.059
0.30	−0.075	0.003	0.004	0.043	0.002	0.070
0.40	−0.108	0.004	0.007	0.051	0.004	0.082
0.50	−0.142	0.004	0.011	0.060	0.006	0.095
0.60	−0.170	0.005	0.015	0.070	0.008	0.110
0.70	−0.191	0.005	0.021	0.081	0.011	0.126
0.80	−0.207	0.006	0.027	0.093	0.014	0.144
0.90	−0.219	0.005	0.034	0.077	0.018	0.124
$\alpha = 90°$						
0	0	0	0	0	0	0
0.10	−0.024	0	0.001	0.003	0.001	0.051
0.20	−0.056	0	0.002	0.004	0.003	0.062
0.30	−0.090	0	0.005	0.005	0.006	0.075
0.40	−0.131	0	0.009	0.006	0.011	0.090
0.50	−0.173	0	0.015	0.007	0.017	0.106
0.60	−0.206	0	0.021	0.008	0.024	0.125
0.70	−0.230	0	0.029	0.010	0.033	0.146
0.80	−0.249	0	0.038	0.008	0.043	0.127
0.90	−0.263	0	0.048	0.009	0.055	0.138

Table III. Normal-Force Coefficients of Airplane Components

ω	$C_{N,\mathrm{B}}$	$C_{N,\mathrm{W}}$	$C'_{N,\mathrm{W}}$	$C_{N,\mathrm{H}}$	$C'_{N,\mathrm{H}}$
$\alpha = 30°$					
0	0.197	0.823	0	0.137	0
0.10	0.198	0.826	0.007	0.137	0.001
0.20	0.199	0.811	0.027	0.137	0.005
0.30	0.200	0.807	0.060	0.138	0.011
0.40	0.201	0.826	0.079	0.138	0.020
0.50	0.204	0.839	0.109	0.135	0.031
0.60	0.207	0.838	0.141	0.135	0.023
0.70	0.211	0.830	0.178	0.134	0.031
0.80	0.215	0.824	0.231	0.135	0.040
0.90	0.219	0.815	0.280	0.138	0.050
$\alpha = 45°$					
0	0.396	0.870	0	0.145	0
0.10	0.398	0.867	0.007	0.144	0.001
0.20	0.401	0.859	0.027	0.144	0.005
0.30	0.404	0.850	0.060	0.144	0.011
0.40	0.407	0.851	0.107	0.144	0.020
0.50	0.413	0.833	0.167	0.143	0.031
0.60	0.421	0.842	0.240	0.142	0.044
0.70	0.431	0.862	0.273	0.142	0.060
0.80	0.441	0.893	0.353	0.141	0.079
0.90	0.452	0.925	0.378	0.142	0.100
$\alpha = 60°$					
0	0.595	0.720	0	0.120	0
0.10	0.599	0.741	0.007	0.121	0.001
0.20	0.603	0.767	0.027	0.122	0.005
0.30	0.609	0.797	0.060	0.123	0.011
0.40	0.616	0.828	0.107	0.125	0.020
0.50	0.627	0.858	0.167	0.127	0.031
0.60	0.642	0.888	0.240	0.129	0.044
0.70	0.660	0.917	0.327	0.131	0.060
0.80	0.680	0.952	0.427	0.135	0.079
0.90	0.701	0.942	0.540	0.139	0.100
$\alpha = 90°$					
0	0.797	0.750	0	0.125	0
0.10	0.802	0.753	0.007	0.125	0.001
0.20	0.809	0.760	0.027	0.125	0.005
0.30	0.818	0.773	0.060	0.125	0.011
0.40	0.830	0.790	0.107	0.126	0.020
0.50	0.849	0.809	0.167	0.126	0.031
0.60	0.874	0.831	0.240	0.127	0.044
0.70	0.903	0.865	0.327	0.128	0.060
0.80	0.936	0.912	0.427	0.130	0.079
0.90	0.971	0.970	0.540	0.132	0.100

Table IV. Yawing-Moment Coefficients of Airplane Components

ω	$C_{n,\mathrm{B}}$	$C_{n,\mathrm{W}}$	$C_{n,\mathrm{H}}$	Tail 3		Tail 4		Tail 5
				$C_{n,\mathrm{V}}$	$C'_{n,\mathrm{V}}$	$C_{n,\mathrm{V}}$	$C'_{n,\mathrm{V}}$	$C_{n,\mathrm{V}}$
$\alpha = 30°$								
0	0	0	0	0	0	0	0	0
0.10	0.001	0.006	0	−0.004	0	−0.008	0	−0.007
0.20	0.003	0.010	0	−0.014	0	−0.023	0	−0.023
0.30	0.004	0.015	0	−0.015	0	−0.026	0	−0.025
0.40	0.007	0.018	0	−0.017	0	−0.029	0	−0.028
0.50	0.009	0.016	0	−0.019	0	−0.032	0	−0.031
0.60	0.010	0.012	0	−0.020	−0.001	−0.036	−0.001	−0.034
0.70	0.011	0.009	0	−0.022	−0.001	−0.039	−0.001	−0.037
0.80	0.011	0.006	0	−0.024	−0.002	−0.043	−0.001	−0.040
0.90	0.010	0.003	0	−0.027	−0.002	−0.047	−0.001	−0.044
$\alpha = 45°$								
0	0	0	0	0	0	0	0	0
0.10	0.002	−0.002	0	−0.003	0	−0.009	0	−0.010
0.20	0.004	−0.004	0	−0.007	0	−0.022	0	−0.025
0.30	0.006	−0.004	0	−0.008	−0.001	−0.026	−0.001	−0.029
0.40	0.010	−0.002	0	−0.010	−0.001	−0.030	−0.001	−0.033
0.50	0.014	0	0	−0.010	−0.002	−0.034	−0.001	−0.037
0.60	0.015	0.005	0	−0.012	−0.004	−0.039	−0.002	−0.042
0.70	0.016	0.009	0	−0.014	−0.005	−0.044	−0.002	−0.048
0.80	0.015	0.010	0	−0.015	−0.006	−0.055	−0.003	−0.053
0.90	0.014	0.010	0	−0.017	−0.008	−0.056	−0.003	−0.060
$\alpha = 60°$								
0	0	0	0	0	0	0	0	0
0.10	0.002	−0.002	0	−0.001	0	−0.009	0	−0.012
0.20	0.006	−0.004	0	−0.001	−0.001	−0.018	−0.001	−0.027
0.30	0.010	−0.006	0	−0.001	−0.002	−0.021	−0.001	−0.032
0.40	0.017	−0.007	0	−0.002	−0.003	−0.025	−0.002	−0.037
0.50	0.023	−0.008	0	−0.002	−0.005	−0.030	−0.003	−0.043
0.60	0.025	−0.008	0	−0.002	−0.007	−0.034	−0.004	−0.049
0.70	0.025	−0.007	0	−0.002	−0.010	−0.040	−0.006	−0.057
0.80	0.024	−0.005	0	−0.003	−0.012	−0.046	−0.007	−0.065
0.90	0.022	−0.001	0	−0.002	−0.015	−0.038	−0.009	−0.056
$\alpha = 90°$								
0	0	0	0	0	0	0	0	0
0.10	0.003	0	0	0	0	−0.002	−0.001	−0.023
0.20	0.008	0	0	0	−0.001	−0.002	−0.002	−0.028
0.30	0.013	0.001	0	0	−0.002	−0.002	−0.003	−0.034
0.40	0.021	0.002	0	0	−0.004	−0.003	−0.005	−0.040
0.50	0.029	0.003	0	0	−0.007	−0.003	−0.008	−0.048
0.60	0.032	0.003	0	0	−0.010	−0.004	−0.012	−0.056
0.70	0.032	0.003	0	0	−0.014	−0.005	−0.016	−0.066
0.80	0.030	0.003	0	0	−0.017	−0.004	−0.021	−0.057
0.90	0.027	0.003	0	0	−0.022	−0.004	−0.027	−0.062

Table V. Rolling-Moment Coefficients of Airplane Components

ω	$C_{l,\mathrm{W}}$	$C'_{l,\mathrm{W}}$	$C_{l,\mathrm{H}}$	$C'_{l,\mathrm{H}}$	Tail 3		Tail 4		Tail 5
					$C_{l,\mathrm{V}}$	$C'_{l,\mathrm{V}}$	$C_{l,\mathrm{V}}$	$C'_{l,\mathrm{V}}$	$C_{l,\mathrm{V}}$
$\alpha = 30°$									
0	0	0	0	0	0	0	0	0	0
0.10	−0.009	0	0	0	0.001	0	0.001	0	0.001
0.20	−0.027	0	0	0	0.002	0	0.004	0	0.004
0.30	−0.033	0	0	0	0.003	0	0.004	0	0.004
0.40	−0.026	−0.006	0	0	0.003	0	0.004	0	0.005
0.50	−0.025	−0.012	−0.001	0	0.003	0	0.005	0	0.005
0.60	−0.030	−0.020	−0.001	−0.001	0.003	0	0.005	0	0.006
0.70	−0.042	−0.029	−0.001	−0.002	0.004	0	0.006	0	0.006
0.80	−0.057	−0.039	−0.001	−0.002	0.004	0	0.007	0	0.007
0.90	−0.075	−0.050	−0.001	−0.002	0.004	0	0.007	0	0.007
$\alpha = 45°$									
0	0	0	0	0	0	0	0	0	0
0.10	0.008	0	0	0	0	0	0.001	0	0.002
0.20	0.011	0	0	0	0.001	0	0.003	0	0.004
0.30	0.012	0	0	0	0.001	0	0.004	0	0.005
0.40	0.010	0	0	0	0.002	0	0.004	0	0.005
0.50	−0.007	0	0	0	0.002	0	0.005	0	0.006
0.60	−0.015	0	0	0	0.002	0.001	0.006	0	0.007
0.70	−0.019	−0.013	0	0	0.002	0.001	0.007	0	0.008
0.80	−0.021	−0.017	0	0	0.003	0.001	0.008	0	0.009
0.90	−0.027	−0.036	0	0	0.003	0.001	0.009	0	0.010
$\alpha = 60°$									
0	0	0	0	0	0	0	0	0	0
0.10	0.003	0	0	0	0	0	0.001	0	0.002
0.20	0.007	0	0	0	0	0	0.003	0	0.004
0.30	0.011	0	0	0	0	0	0.003	0.001	0.005
0.40	0.015	0	0	0	0	0.001	0.004	0.001	0.006
0.50	0.016	0	0	0	0	0.001	0.004	0.002	0.007
0.60	0.015	0	0	0	0	0.001	0.005	0.003	0.008
0.70	0.013	0	0	0	0	0.002	0.006	0.004	0.009
0.80	0.010	0	0	0	0	0.002	0.007	0.005	0.011
0.90	−0.017	0	0	0	0	0.003	0.006	0.006	0.009
$\alpha = 90°$									
0	0	0	0	0	0	0	0	0	0
0.10	0	0	0	0	0	0	0	0	0.004
0.20	0	0	0	0	0	0	0	0	0.005
0.30	0	0	0	0	0	0	0	0	0.006
0.40	0	0	0	0	0	0.001	0.001	0.001	0.007
0.50	0.001	0	0	0	0	0.001	0.001	0.001	0.008
0.60	0.001	0	0	0	0	0.002	0.001	0.002	0.009
0.70	0.002	0	0	0	0	0.002	0.001	0.003	0.011
0.80	0.001	0	0	0	0	0.003	0.001	0.003	0.009
0.90	0.001	0	0	0	0	0.004	0.001	0.004	0.010

Table VI. Pitching-Moment Coefficients of Airplane Components

ω	$C_{m,\mathrm{B}}$	$C_{m,\mathrm{W}}$	$C'_{m,\mathrm{W}}$	$C_{m,\mathrm{H}}$	$C'_{m,\mathrm{H}}$
$\alpha = 30°$					
0	0.111	−0.129	0	−0.415	0
0.10	0.108	−0.128	−0.002	−0.415	−0.003
0.20	0.105	−0.123	−0.006	−0.415	−0.015
0.30	0.101	−0.119	−0.015	−0.415	−0.033
0.40	0.098	−0.116	−0.020	−0.418	−0.061
0.50	0.096	−0.115	−0.026	−0.418	−0.094
0.60	0.095	−0.116	−0.035	−0.415	−0.070
0.70	0.095	−0.118	−0.044	−0.415	−0.094
0.80	0.094	−0.122	−0.057	−0.415	−0.121
0.90	0.093	−0.126	−0.069	−0.418	−0.152
$\alpha = 45°$					
0	0.060	−0.174	0	−0.437	0
0.10	0.053	−0.173	−0.002	−0.437	−0.001
0.20	0.046	−0.171	−0.007	−0.437	−0.002
0.30	0.038	−0.169	−0.015	−0.437	−0.003
0.40	0.030	−0.167	−0.026	−0.436	−0.061
0.50	0.024	−0.162	−0.041	−0.434	−0.094
0.60	0.020	−0.159	−0.059	−0.431	−0.133
0.70	0.017	−0.157	−0.067	−0.431	−0.182
0.80	0.012	−0.156	−0.087	−0.428	−0.240
0.90	0.007	−0.157	−0.093	−0.431	−0.303
$\alpha = 60°$					
0	−0.048	−0.176	0	−0.378	0
0.10	−0.059	−0.178	−0.002	−0.378	−0.003
0.20	−0.071	−0.181	−0.007	−0.378	−0.015
0.30	−0.085	−0.184	−0.015	−0.382	−0.033
0.40	−0.099	−0.187	−0.026	−0.382	−0.061
0.50	−0.111	−0.190	−0.041	−0.382	−0.094
0.60	−0.122	−0.193	−0.059	−0.385	−0.133
0.70	−0.133	−0.195	−0.080	−0.385	−0.182
0.80	−0.146	−0.197	−0.105	−0.390	−0.240
0.90	−0.161	−0.196	−0.132	−0.400	−0.303
$\alpha = 90°$					
0	−0.282	−0.183	0	−0.378	0
0.10	−0.297	−0.184	−0.002	−0.378	−0.003
0.20	−0.316	−0.185	−0.007	−0.378	−0.015
0.30	−0.338	−0.189	−0.015	−0.382	−0.033
0.40	−0.363	−0.193	−0.026	−0.382	−0.061
0.50	−0.387	−0.197	−0.041	−0.382	−0.094
0.60	−0.411	−0.203	−0.080	−0.385	−0.133
0.70	−0.436	−0.220	−0.105	−0.385	−0.182
0.80	−0.466	−0.220	−0.105	−0.385	−0.240
0.90	−0.502	−0.232	−0.132	−0.400	−0.300

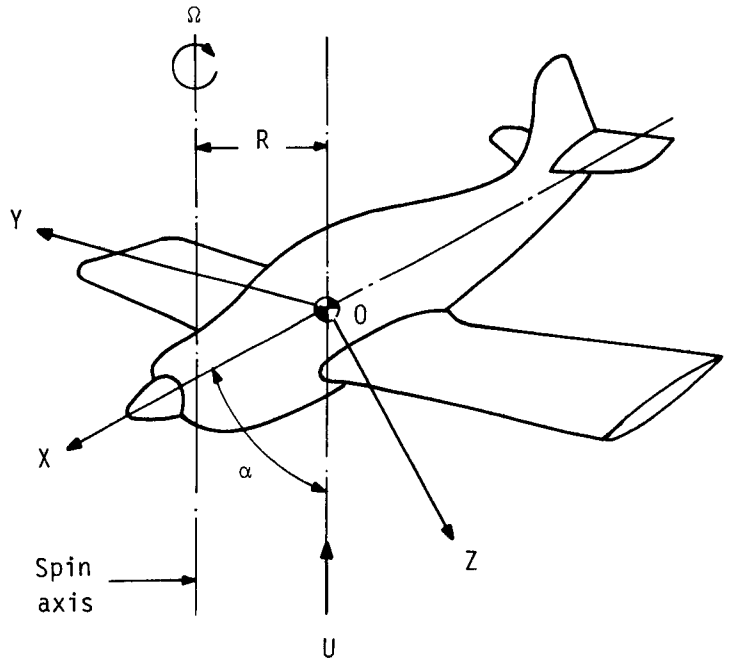

Figure 1. Schematic diagram of steadily rotating airplane model in spin tunnel.

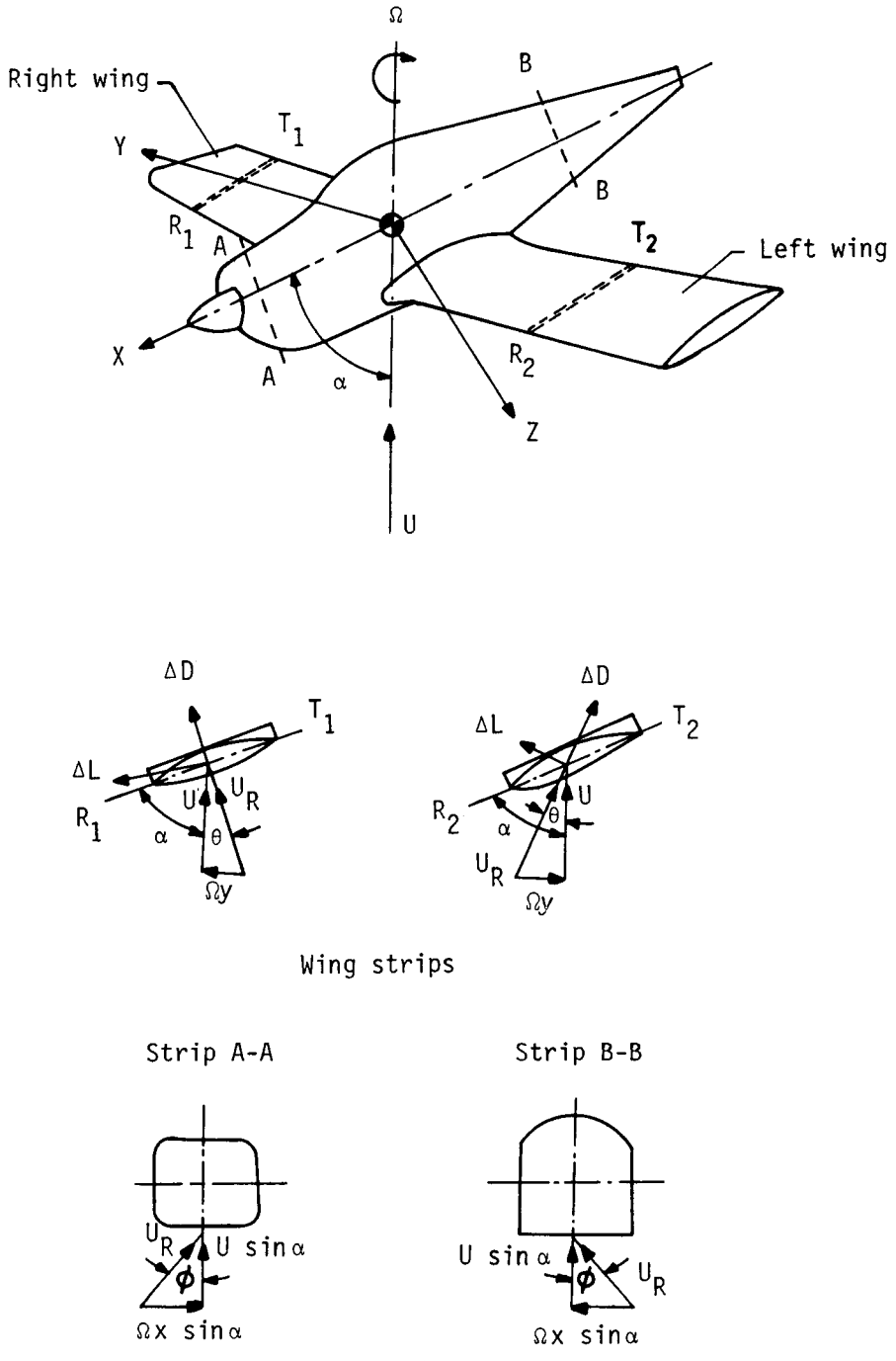

Figure 2. Schematic diagram showing strip parameters of wing and body of rotating airplane.

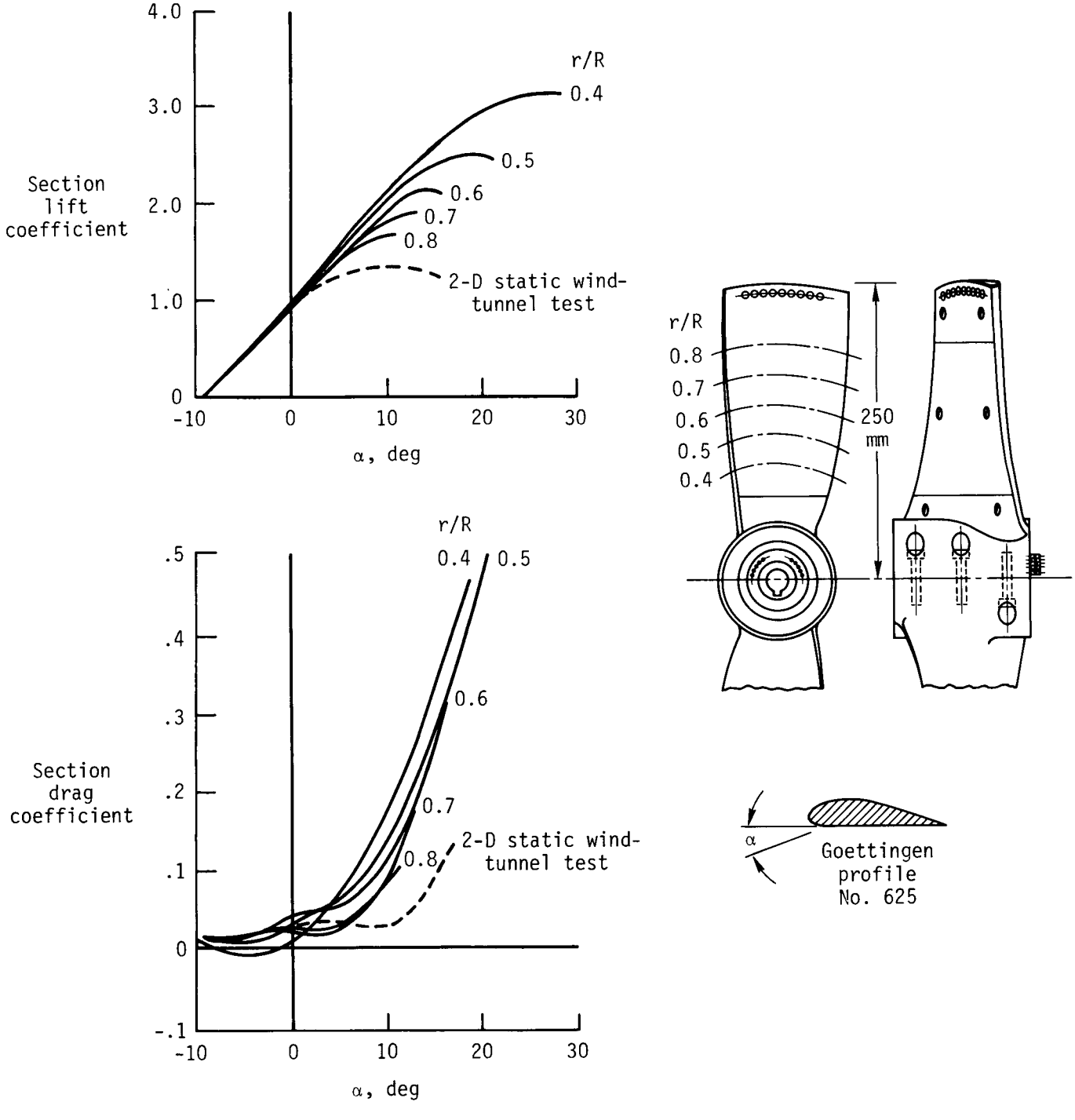

Figure 3. Variation of section lift and drag coefficients on rotating propeller. (From Himmelskamp, ref. 9.)

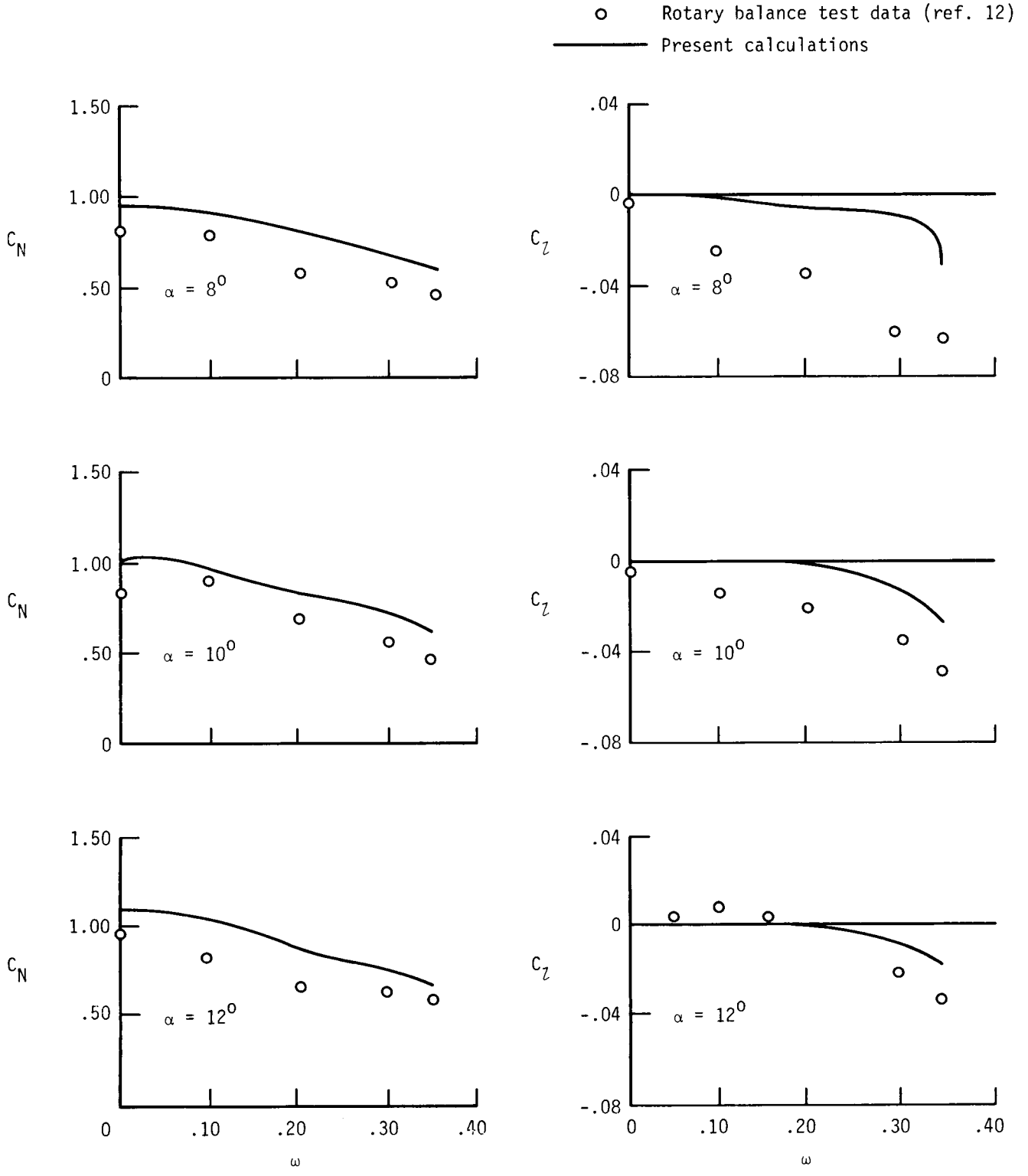

(a) Normal-force coefficient.

(b) Rolling-moment coefficient.

Figure 4. Strip theory calculations for Himmelskamp's rotating propeller (ref. 9).

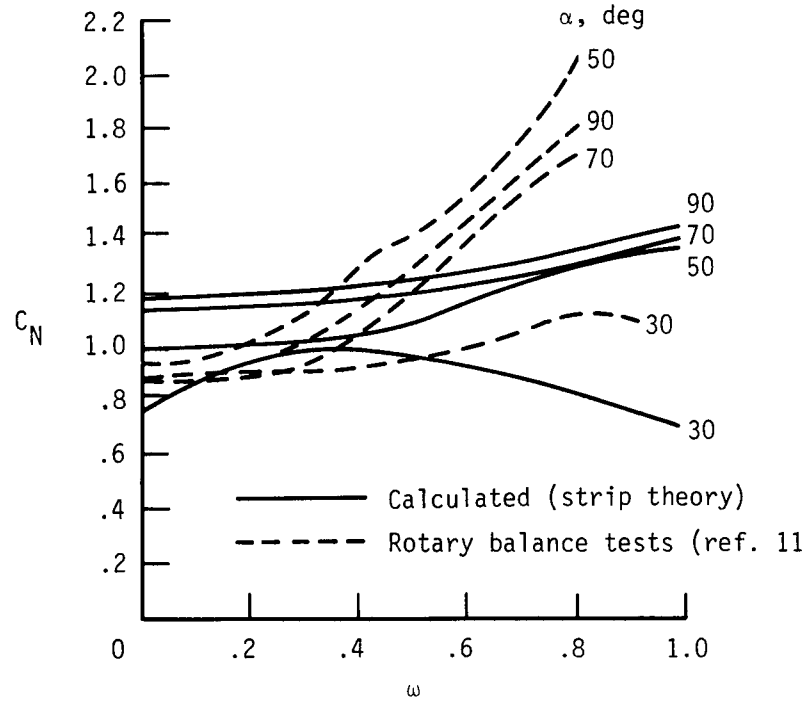

Figure 5. Comparison of strip theory calculations for normal-force coefficient with rotary balance test data. (From ref. 13.)

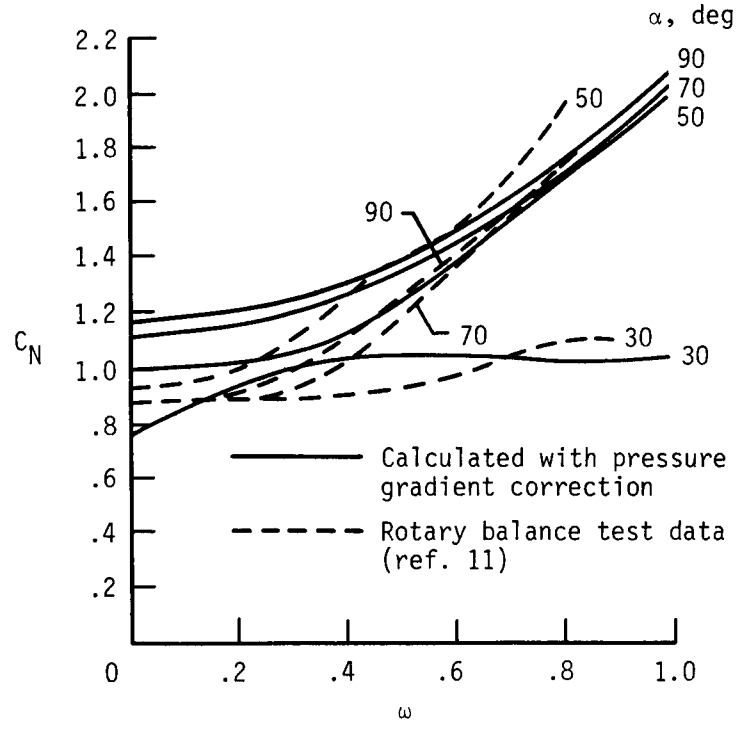

Figure 6. Comparison of McCormick's strip theory calculations for normal-force coefficient incorporating radial pressure gradient term (ref. 13) with rotary balance test data (ref. 11).

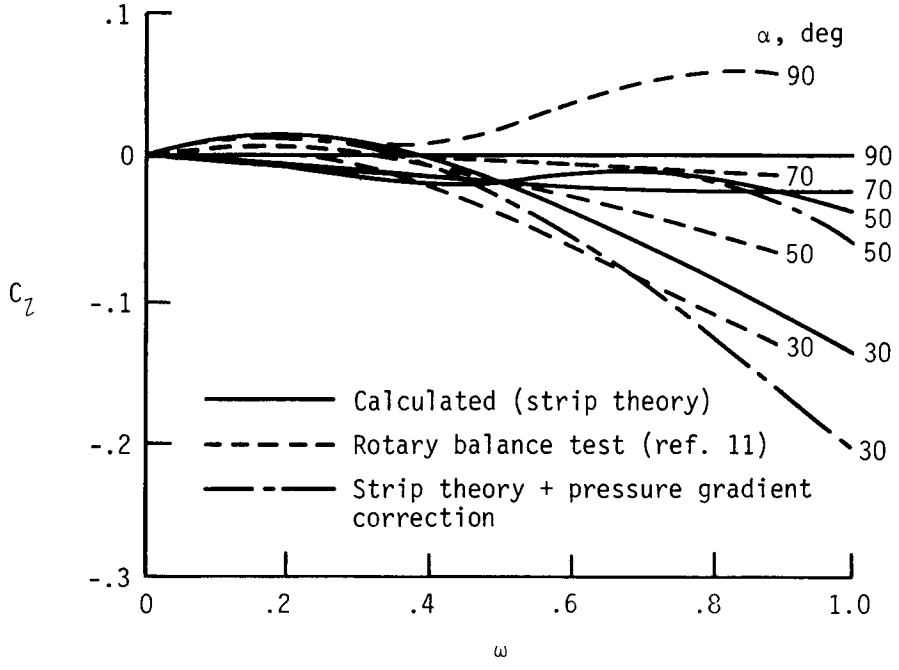

Figure 7. Comparison of calculated rolling-moment coefficient based on strip theory and radial pressure gradient correction (ref. 13) with rotary balance test data (ref. 11).

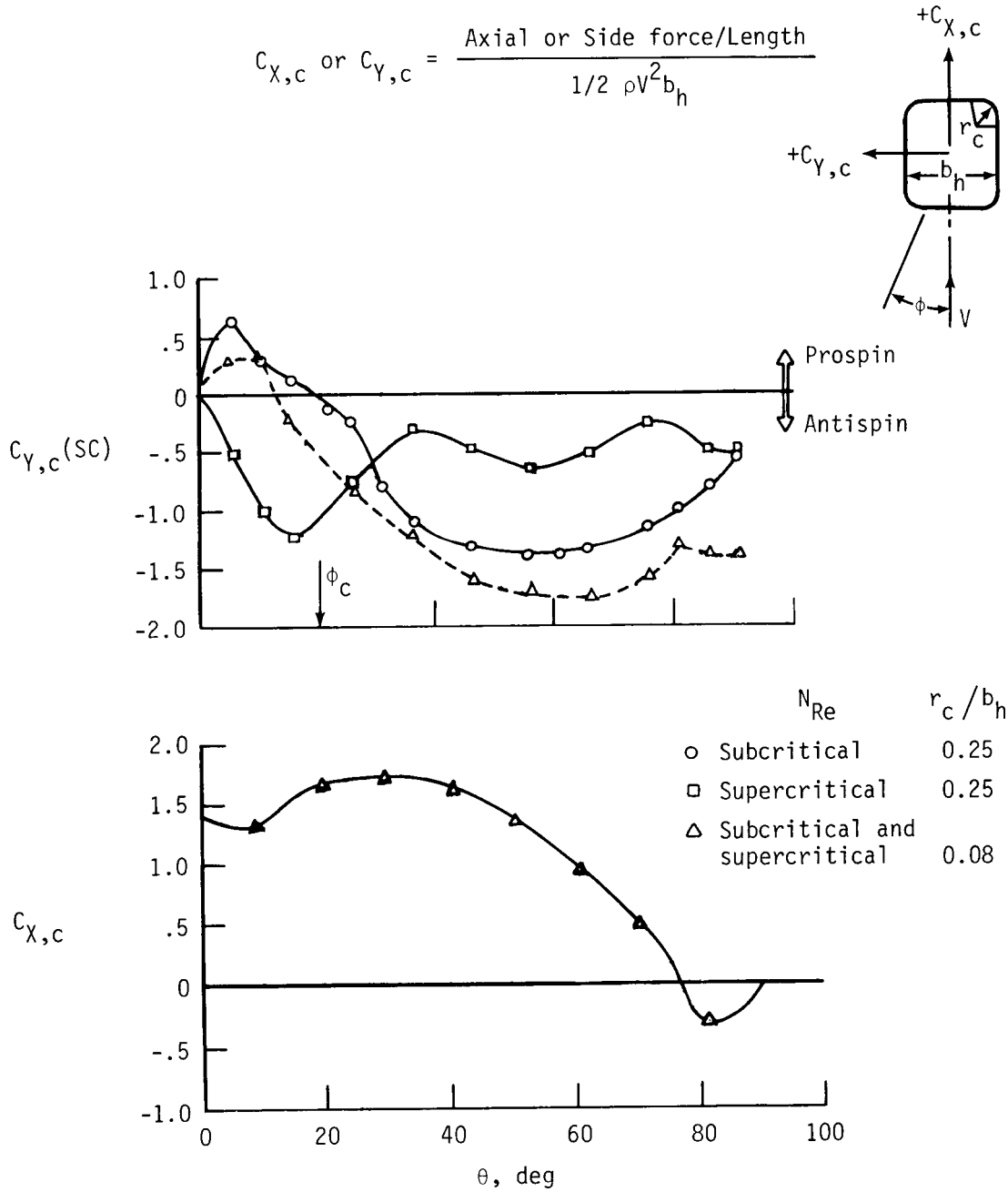

Figure 8. Aerodynamic characteristics of two-dimensional square cylinders (ref. 24).

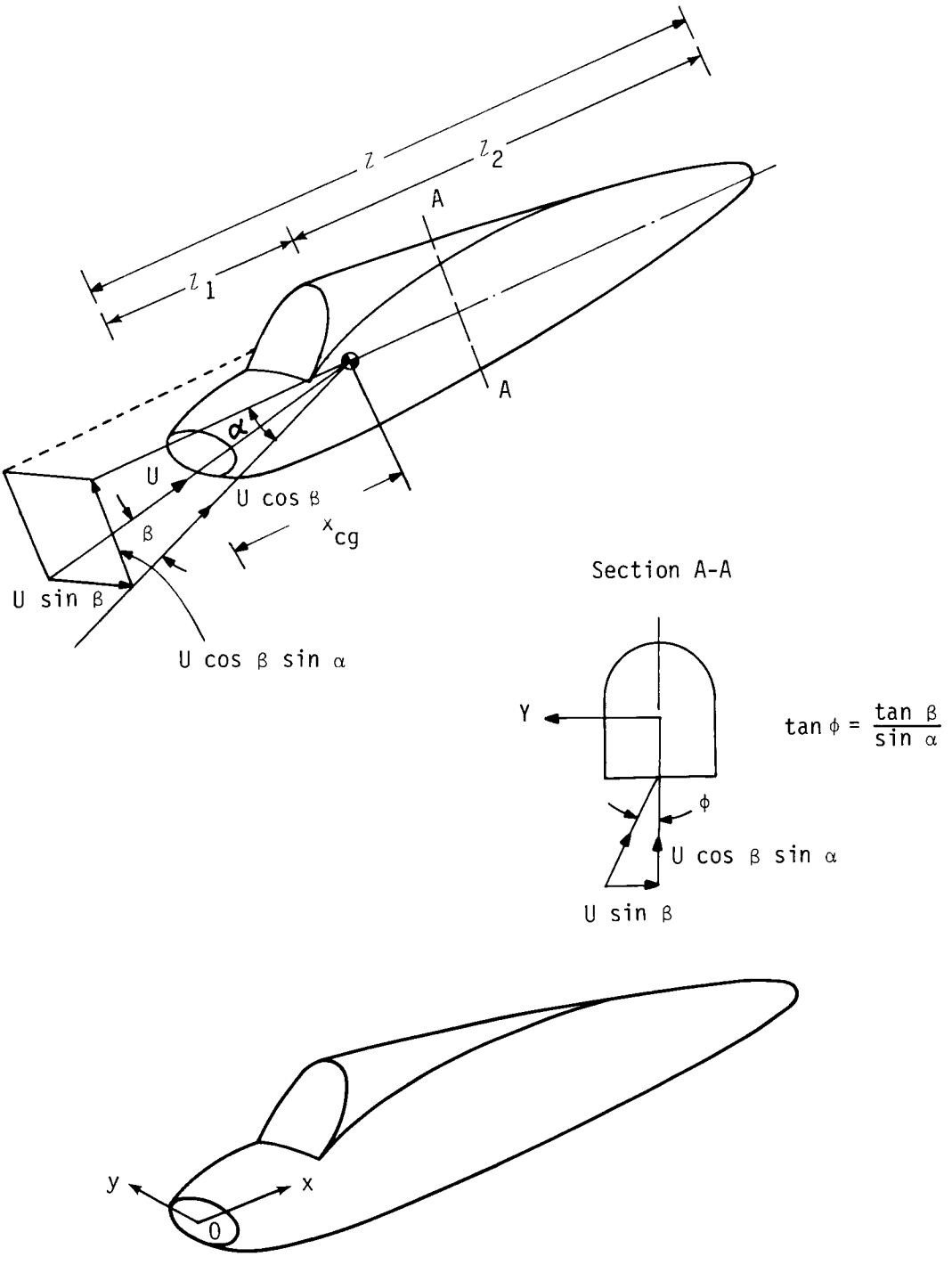

Figure 9. Static body at angles of attack and sideslip.

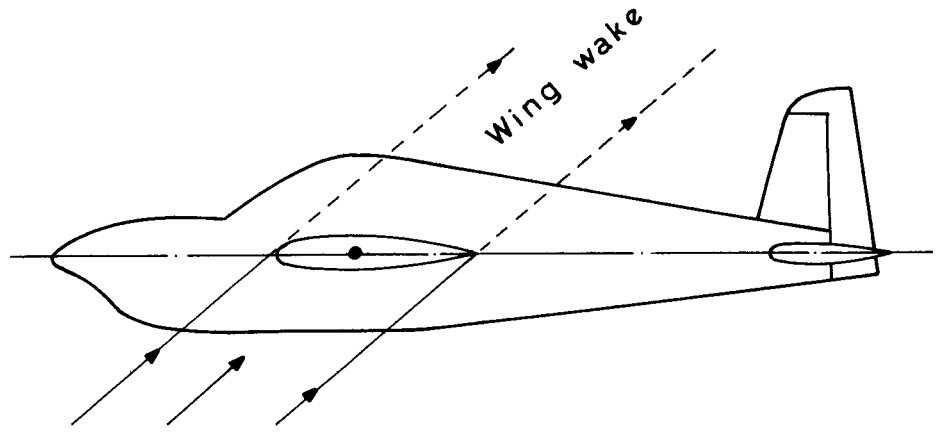

(a) Horizontal tail out of wing wake; $\eta_H = 1$.

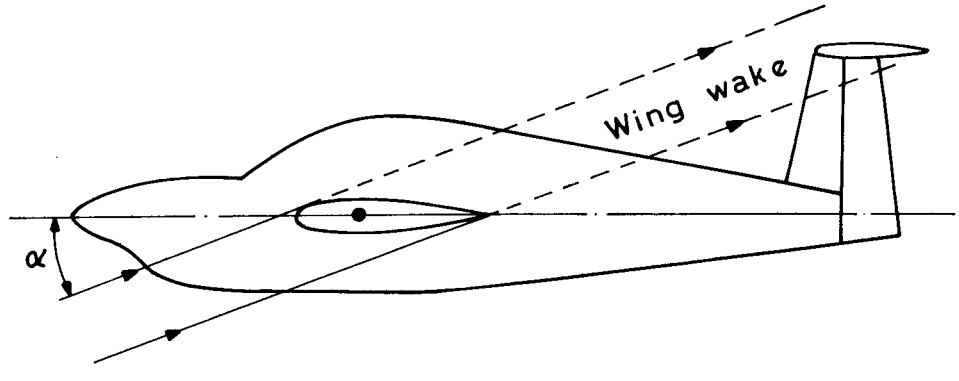

(b) Horizontal tail fully immersed in wing wake; $\eta_H = 0$.

Figure 10. Wing-tail flow interactions.

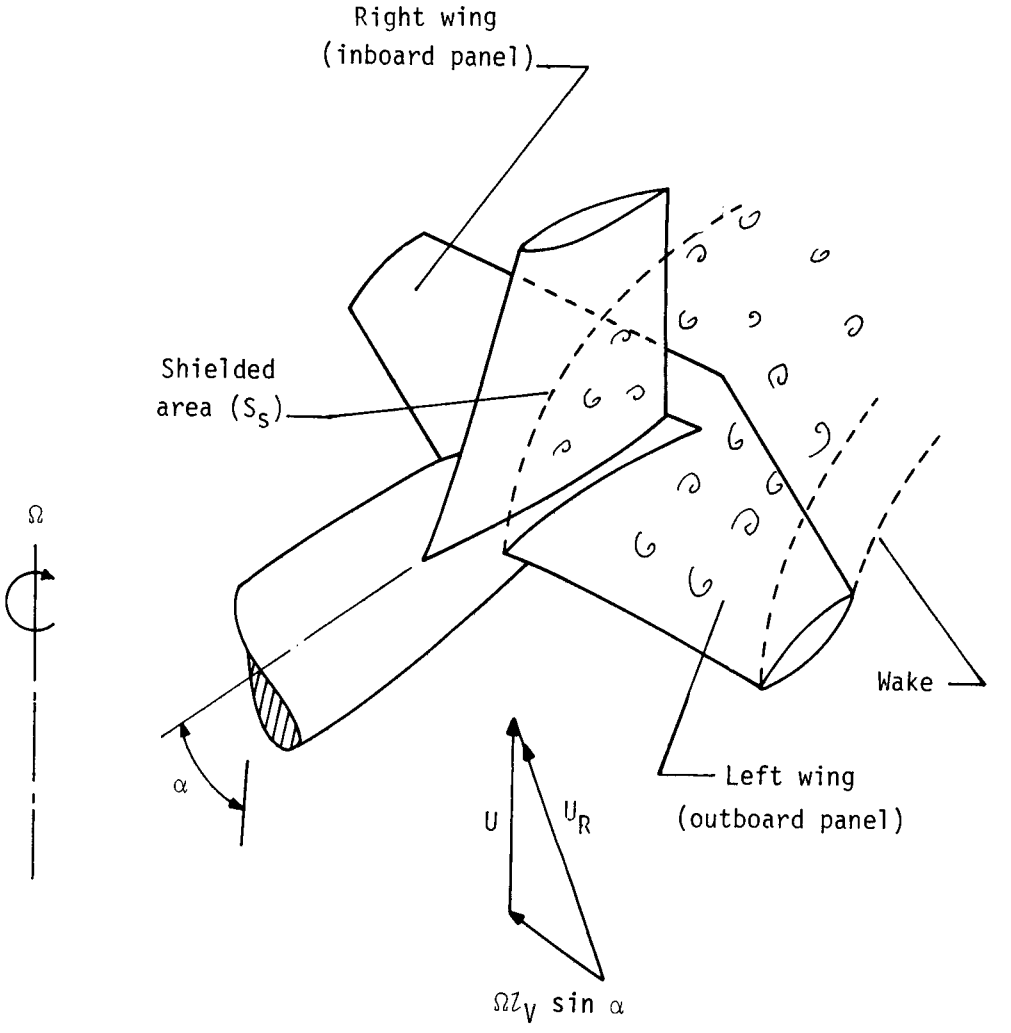

Figure 11. Schematic diagram showing shielding of vertical tail in right spin.

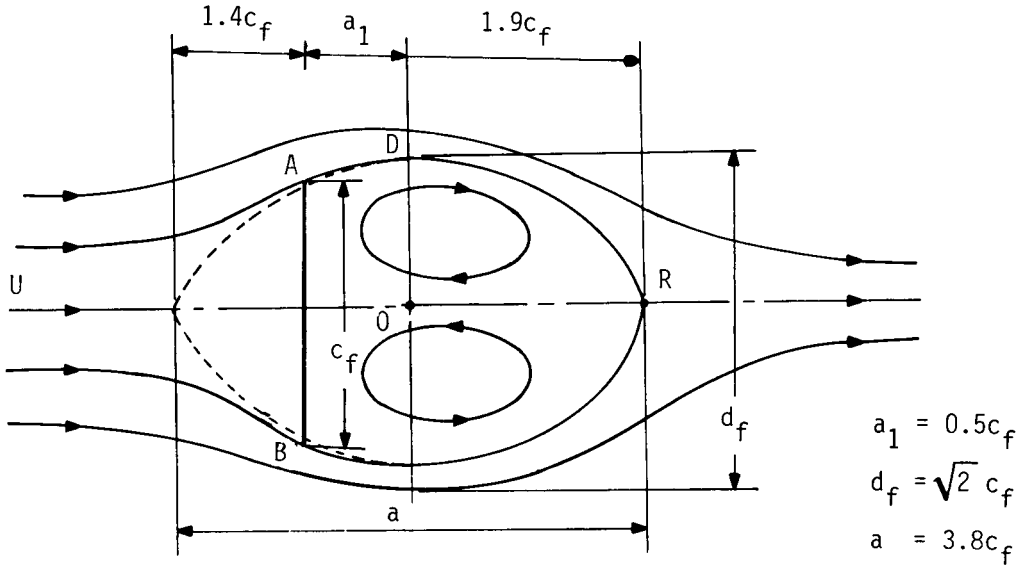

(a) Recirculating region in the wake of a normal flat plate (refs. 30 and 31).

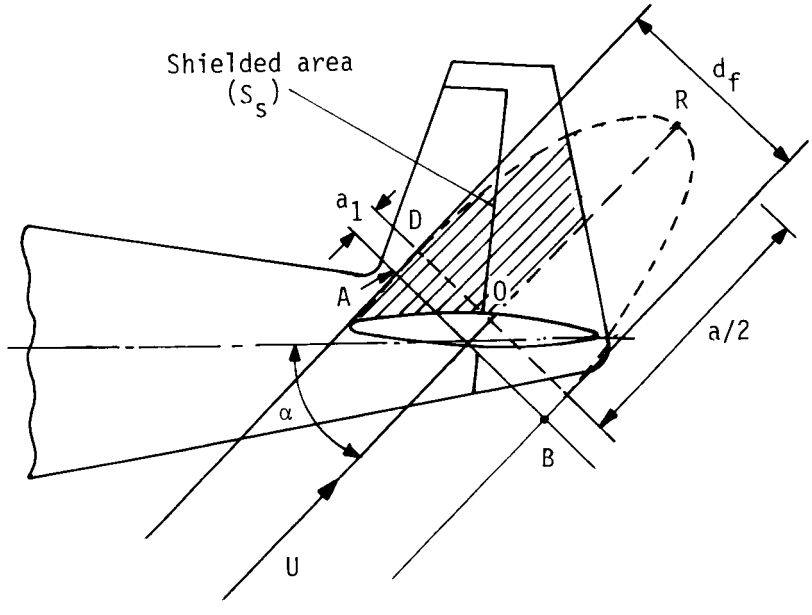

(b) Evaluation of shielded area.

Figure 12. Modeling of shielded area of vertical tail in spin.

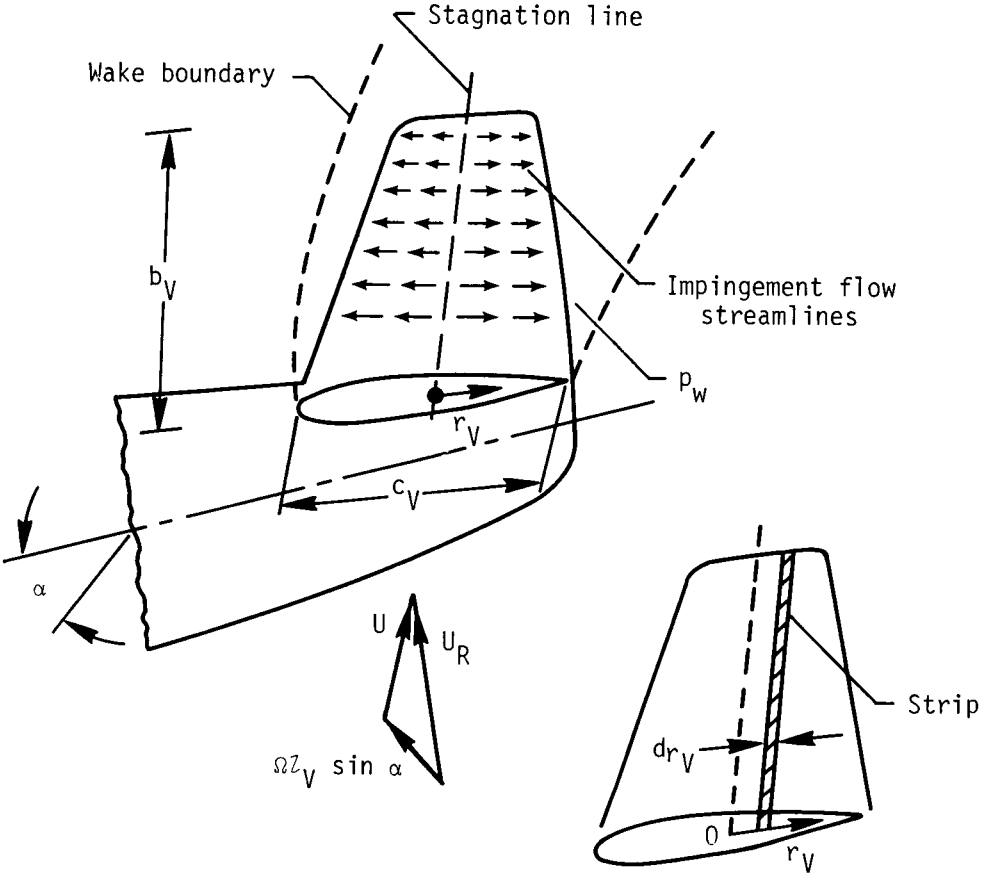

Figure 13. Schematic diagram of impingement of wake flow over vertical tail.

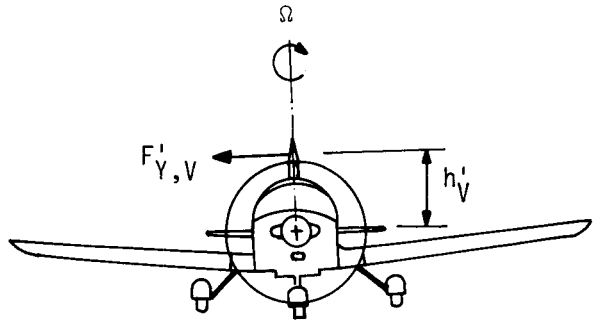

Side force due to secondary flow effect

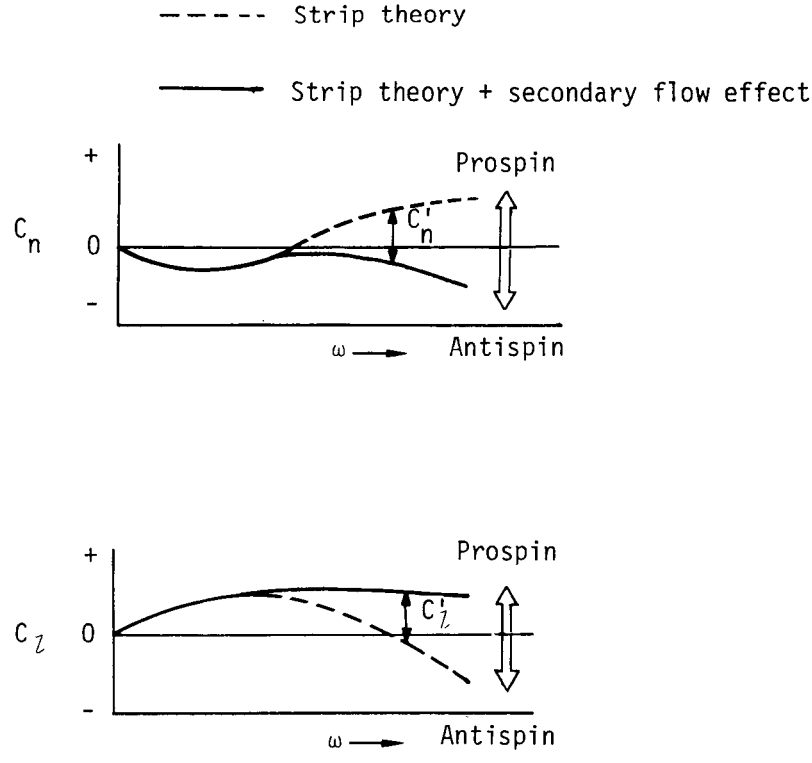

Figure 14. Schematic illustration of secondary flow effects over vertical tail in right spin.

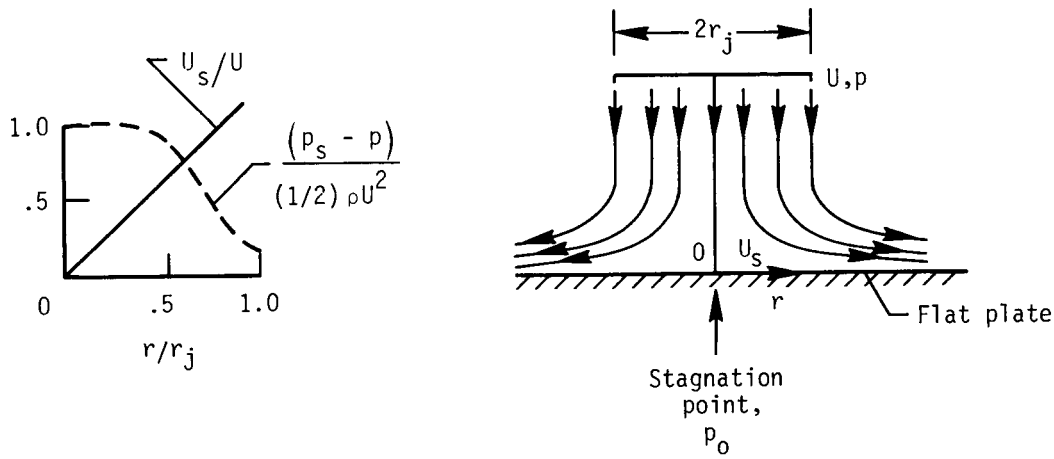

Figure 15. Schematic sketch of idealized impinging flow (ref. 32).

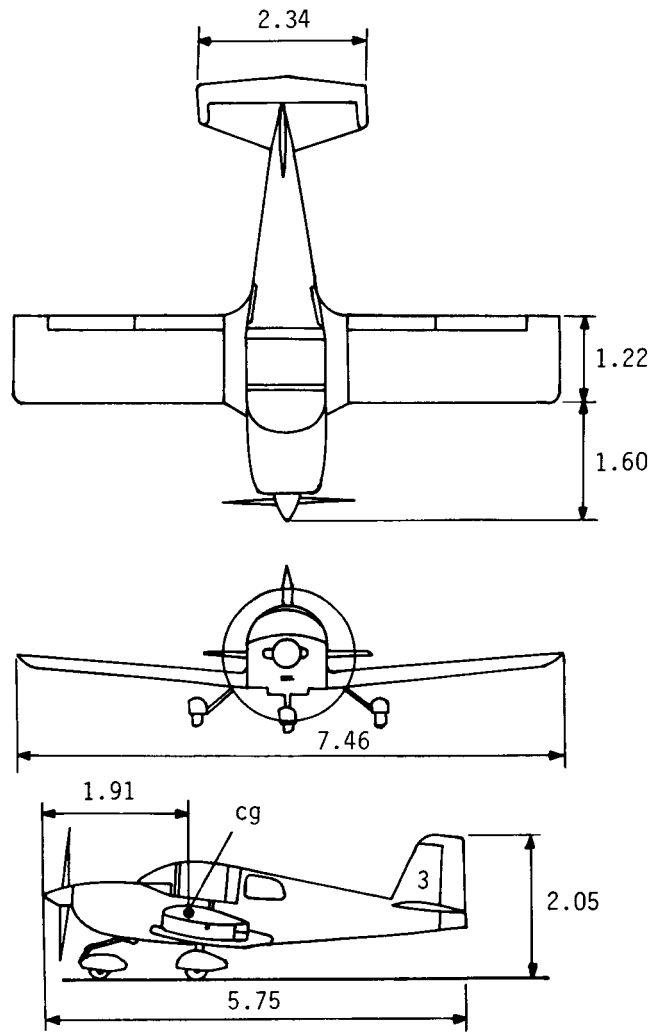

Figure 16. Spin research airplane (full scale). Model A with tail 3; all dimensions are in meters.

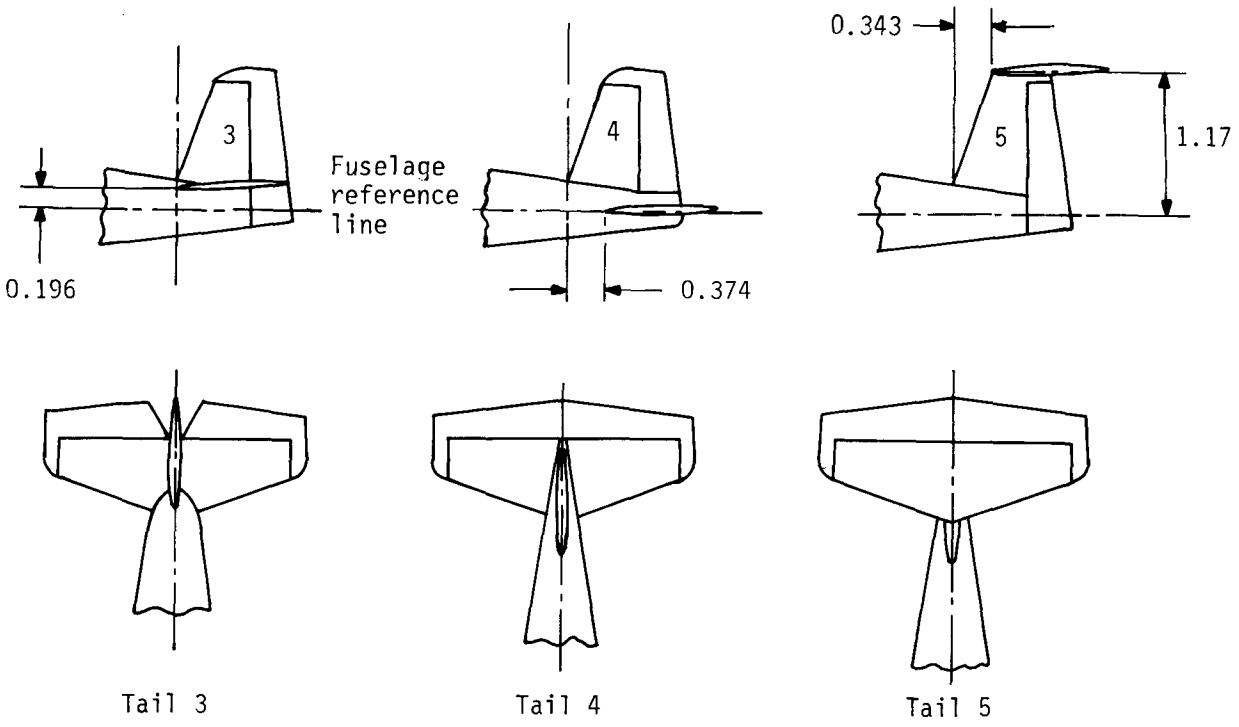

Figure 17. Tail configurations. All dimensions are in meters.

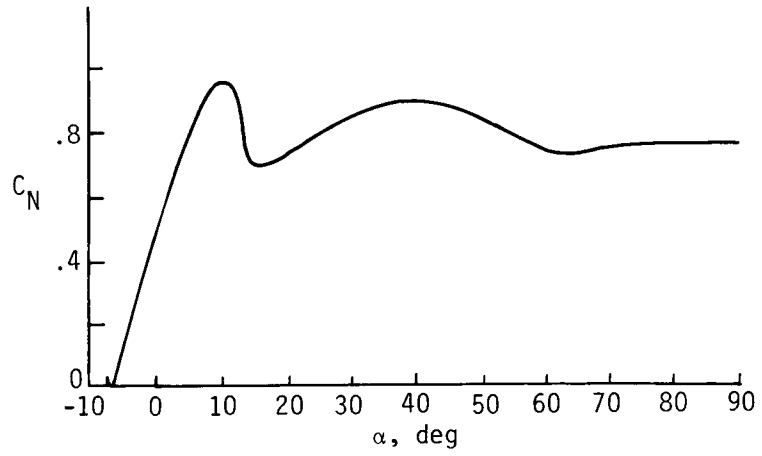

(a) Normal-force coefficient (from ref. 10).

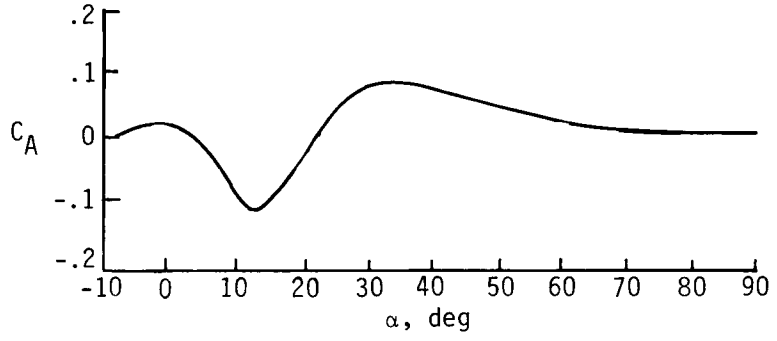

(b) Axial-force coefficient (from ref. 10).

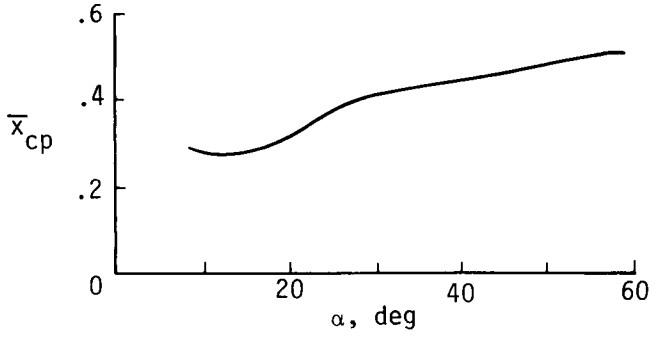

(c) Center of pressure (from ref. 33).

Figure 18. Input static aerodynamic data for wing and horizontal tail. $N_{Re} = 0.288 \times 10^6$.

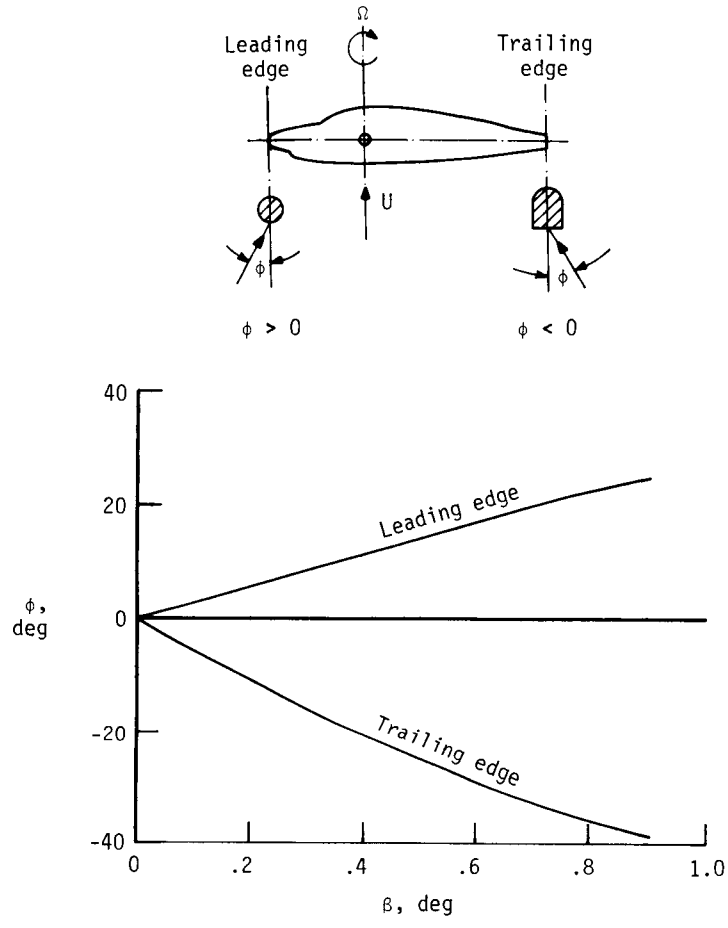

(a) Cross-flow angles encountered in spin.

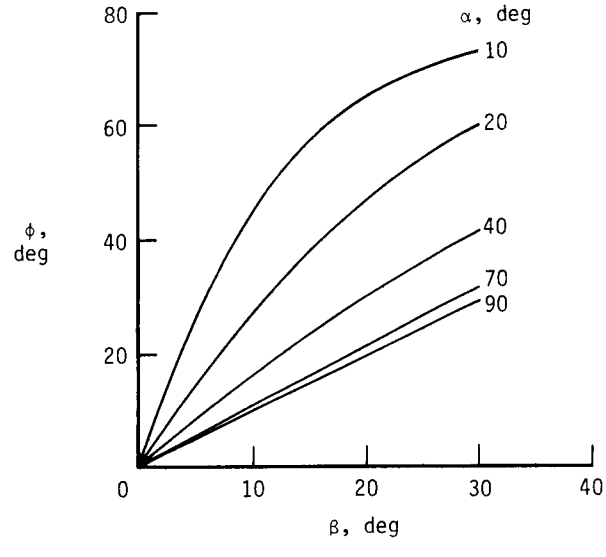

(b) Cross-flow angles encountered in static calculations.

Figure 19. Cross-flow angles over body.

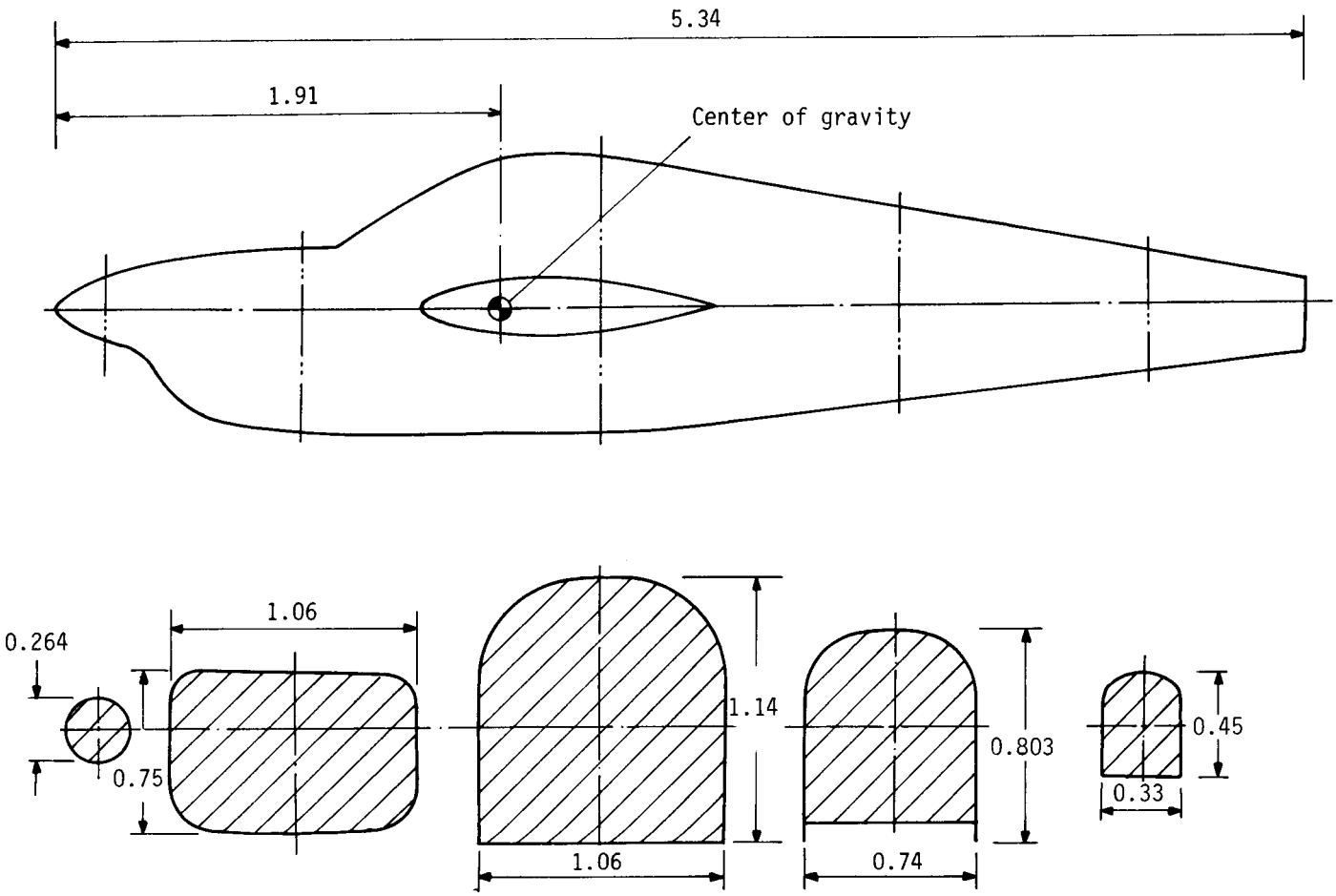

Figure 20. Geometry of body of model A airplane. All dimensions are in meters.

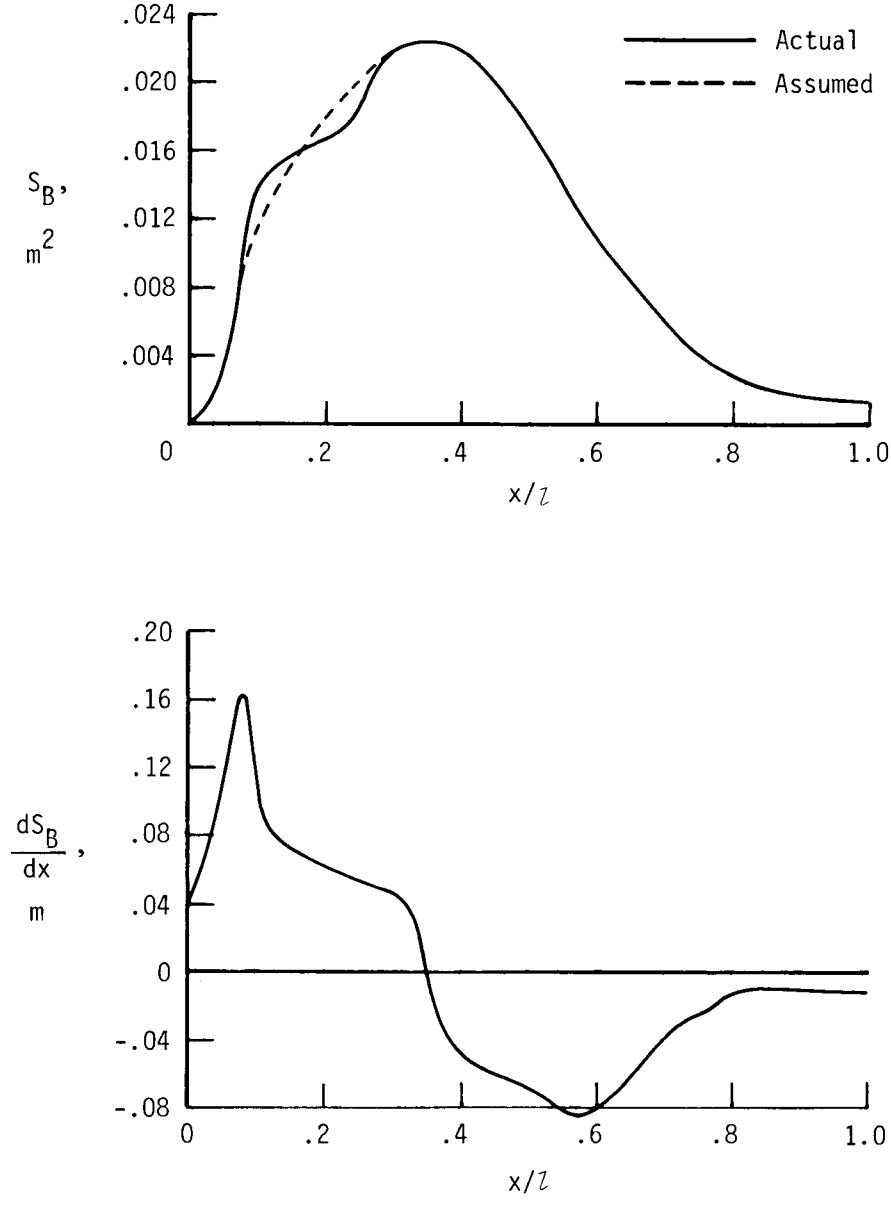

Figure 21. Actual and assumed cross-sectional areas of body.

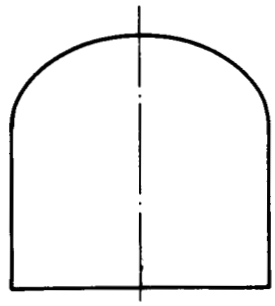

Figure 22. Idealized cross-sectional shape of body.

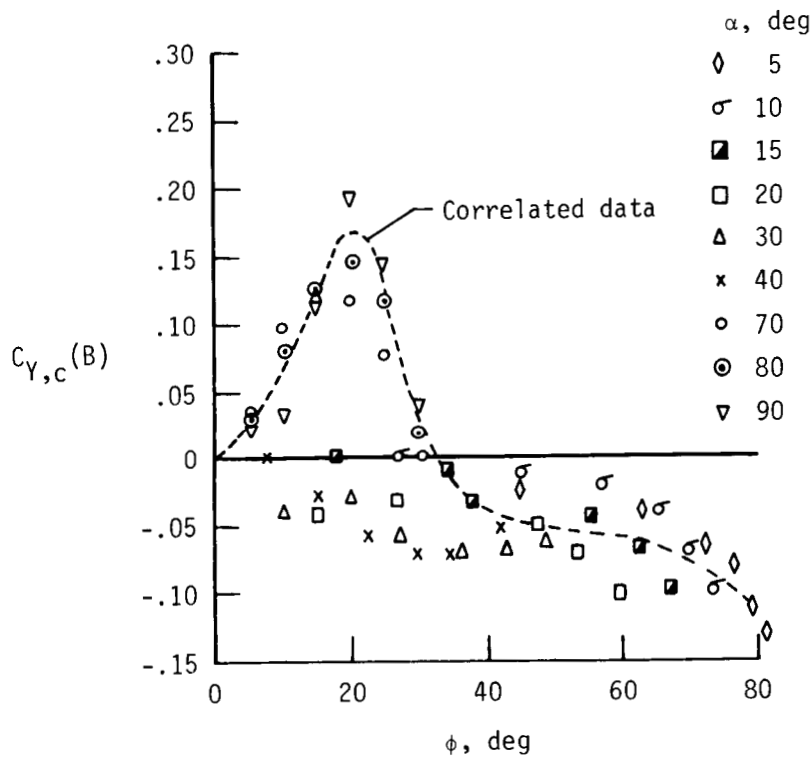

Figure 23. Correlation of side-force data (ref. 10). $N_{Re} = 0.288 \times 10^6$.

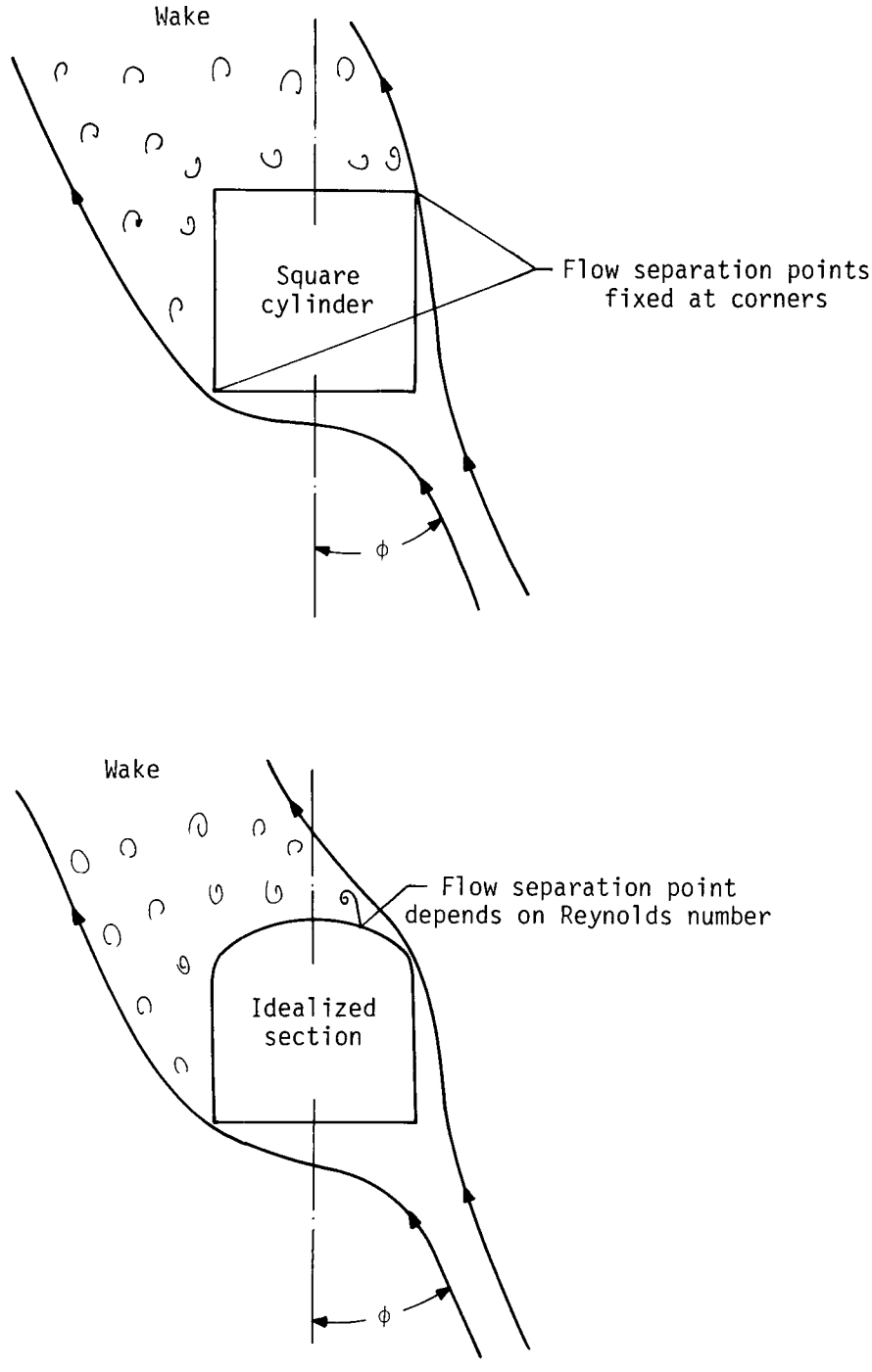

Figure 24. Schematic sketch of flow patterns.

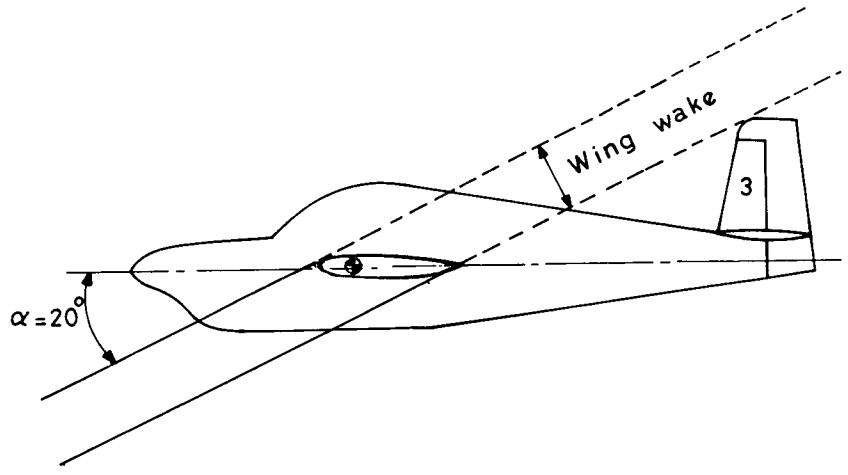

(a) Tail 3; horizontal tail always out of wing wake for $\alpha > 20°$; $\eta_H = 1$.

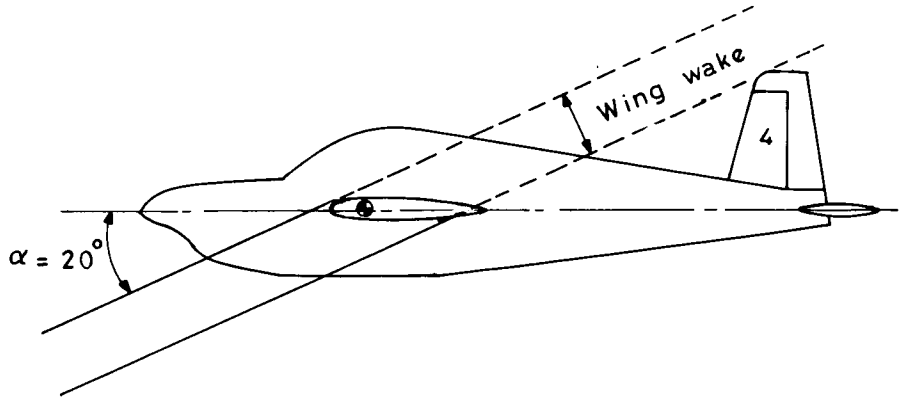

(b) Tail 4; horizontal tail always out of wing wake for $\alpha > 20°$; $\eta_H = 1$.

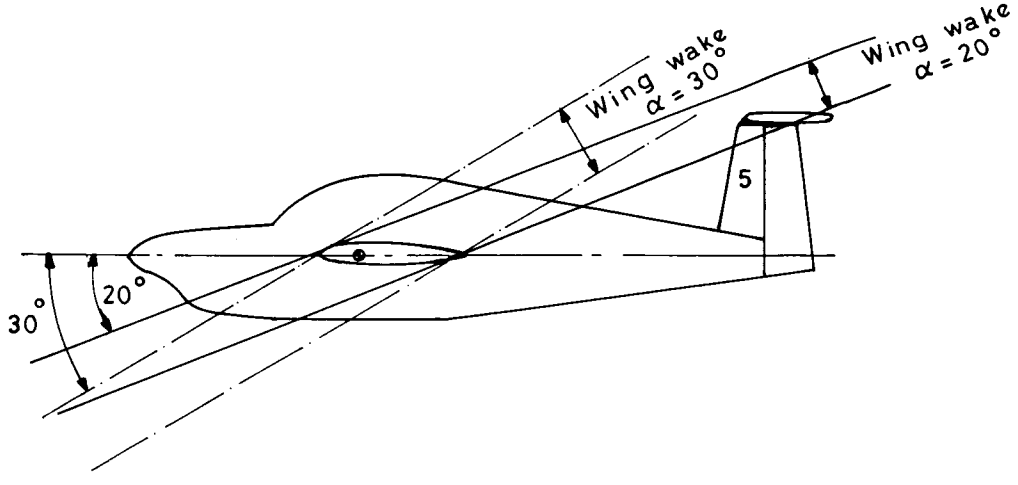

(c) Tail 5; horizontal tail immersed in wing wake for $\alpha \leq 20°$ ($\eta_H = 0$) and out of wing wake for $\alpha > 30°$ ($\eta_H = 1$).

Figure 25. Interactions of wing wake and horizontal tail.

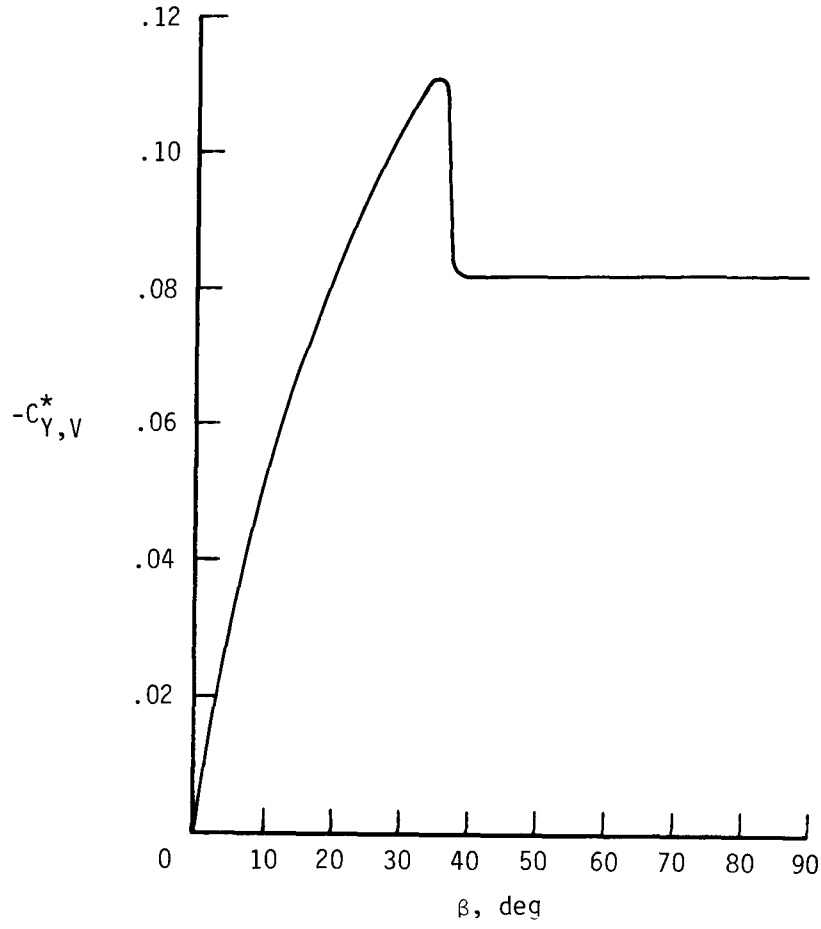

Figure 26. Side-force coefficients for unshielded vertical tail of low aspect ratio.

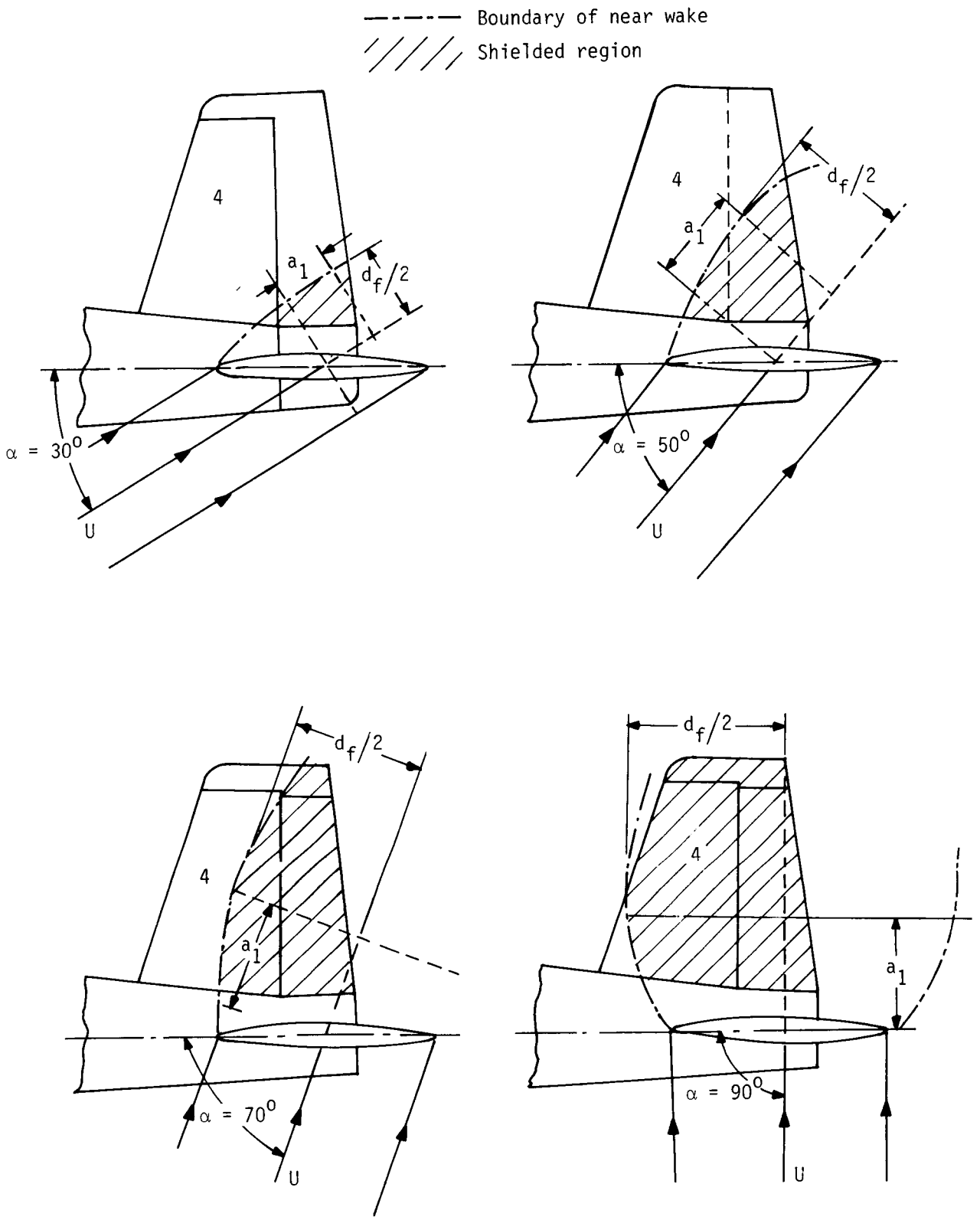

Figure 27. Graphical evaluation of shielded area of vertical tail at various angles of attack (tail 4).

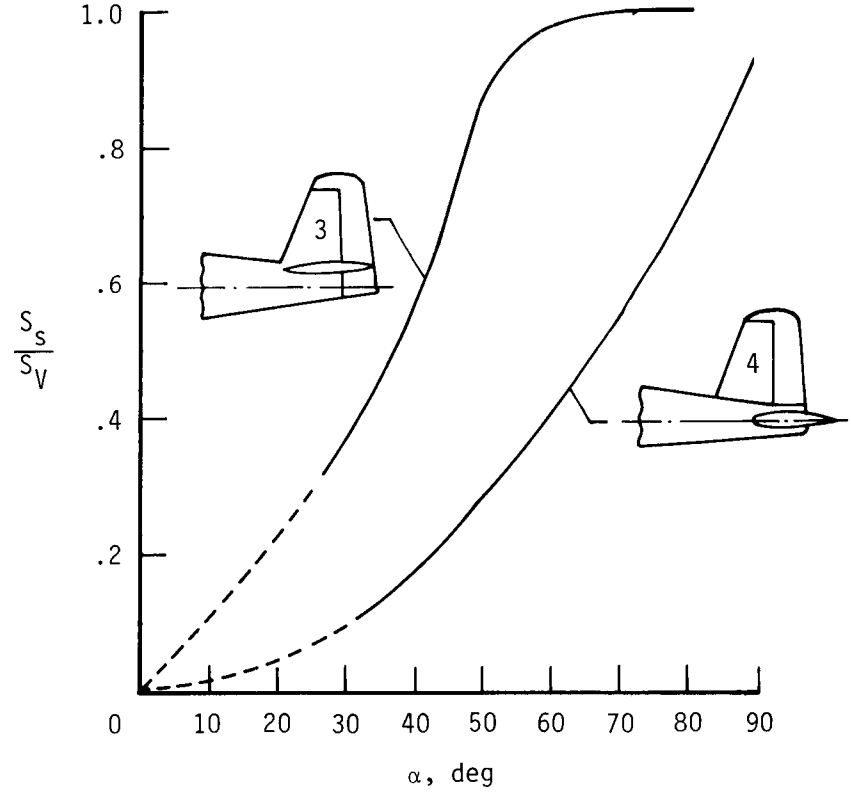

Figure 28. Variation of shielded area with angle of attack.

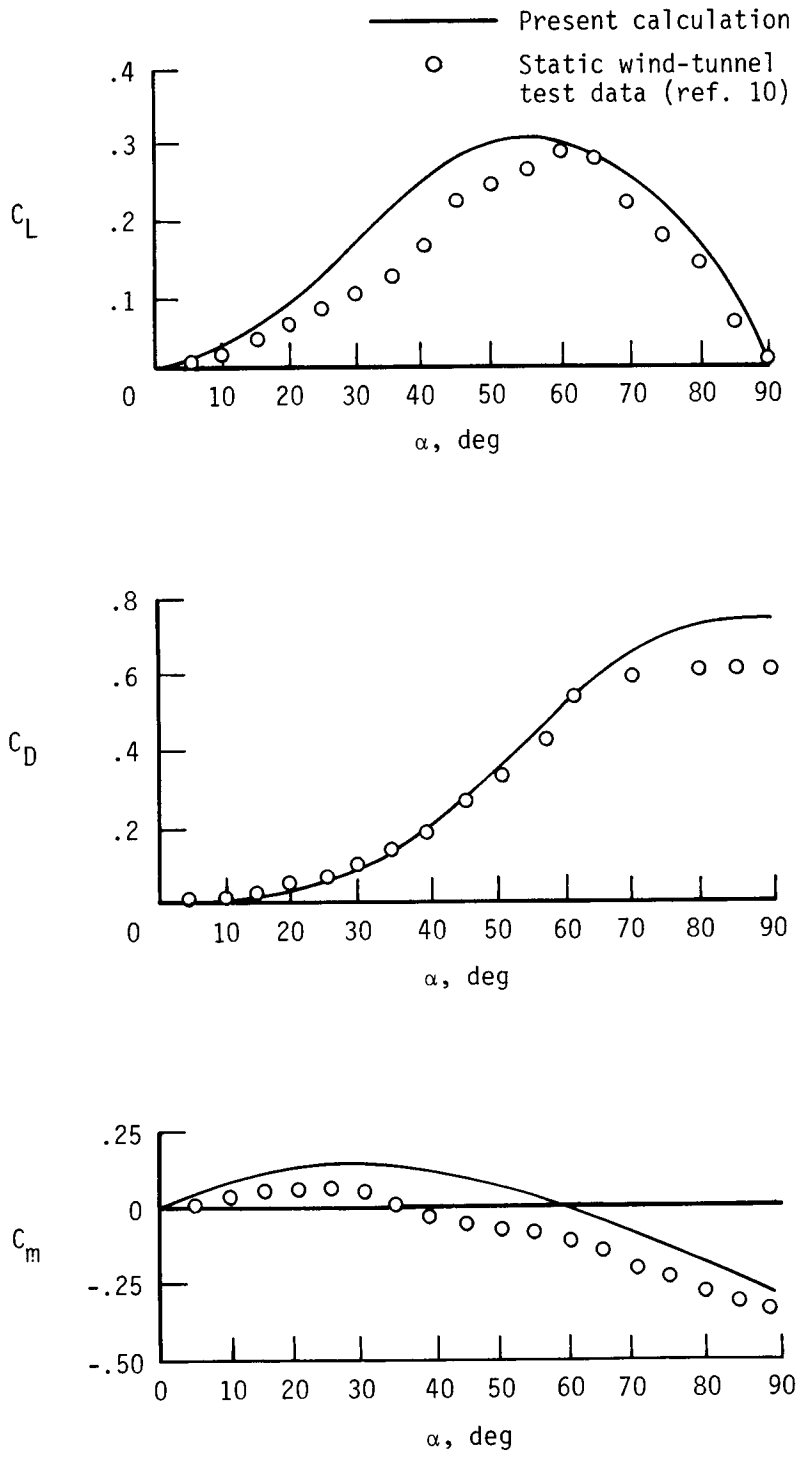

Figure 29. Static longitudinal aerodynamic coefficients of body of model A airplane. $N_{Re} = 0.288 \times 10^6$.

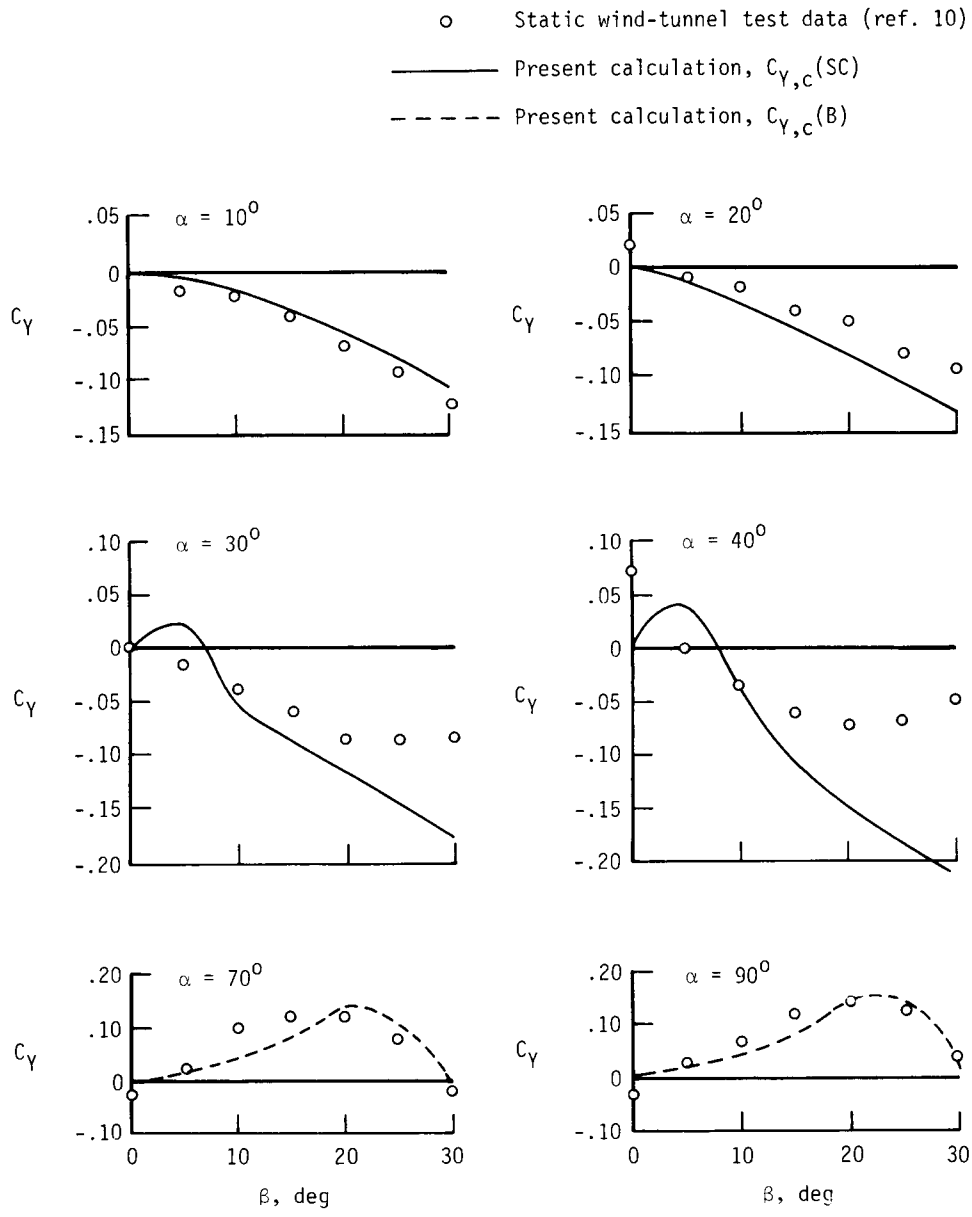

Figure 30. Static side-force characteristics of body of model A airplane.

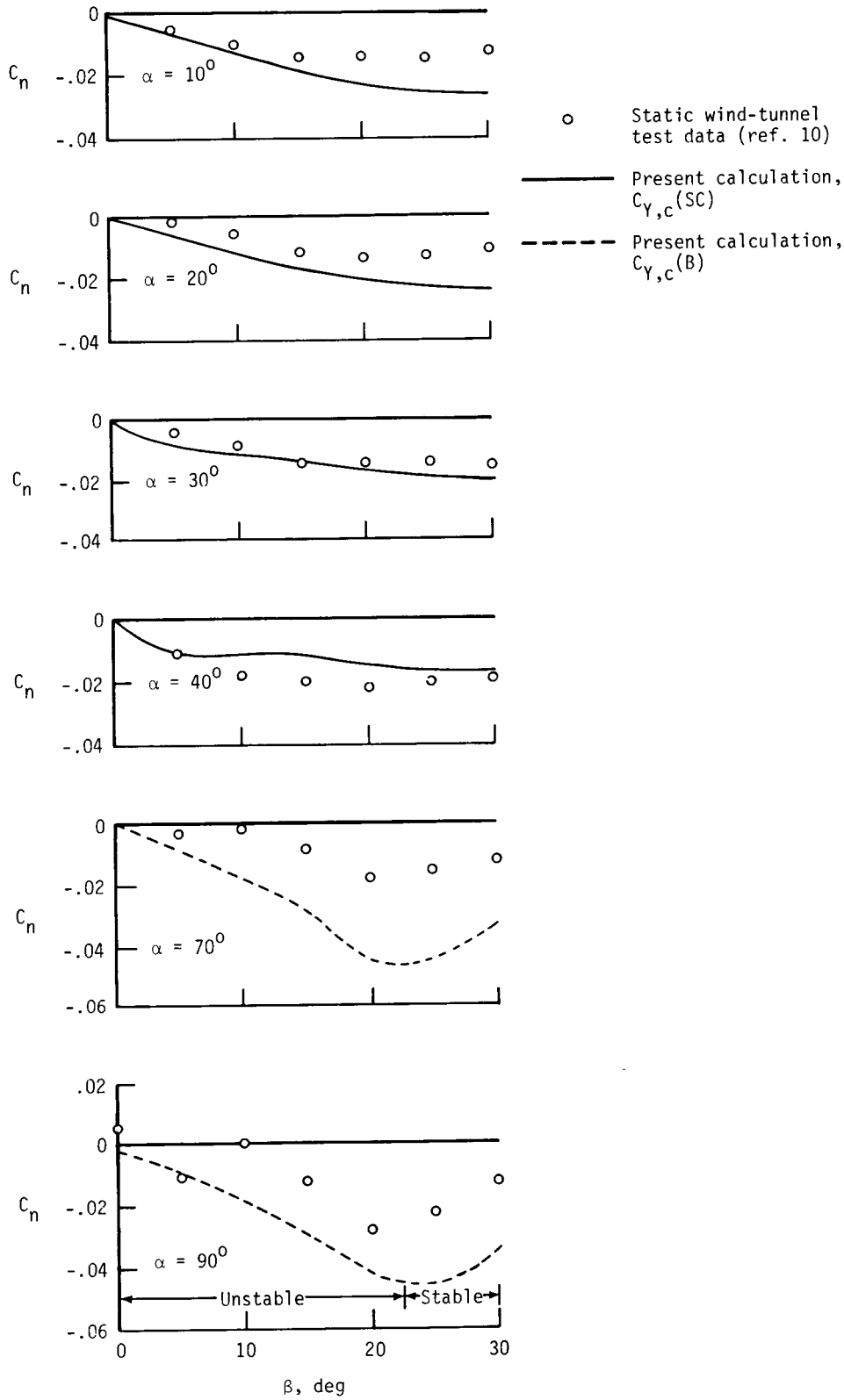

Figure 31. Static yawing-moment characteristics of body of model A airplane.

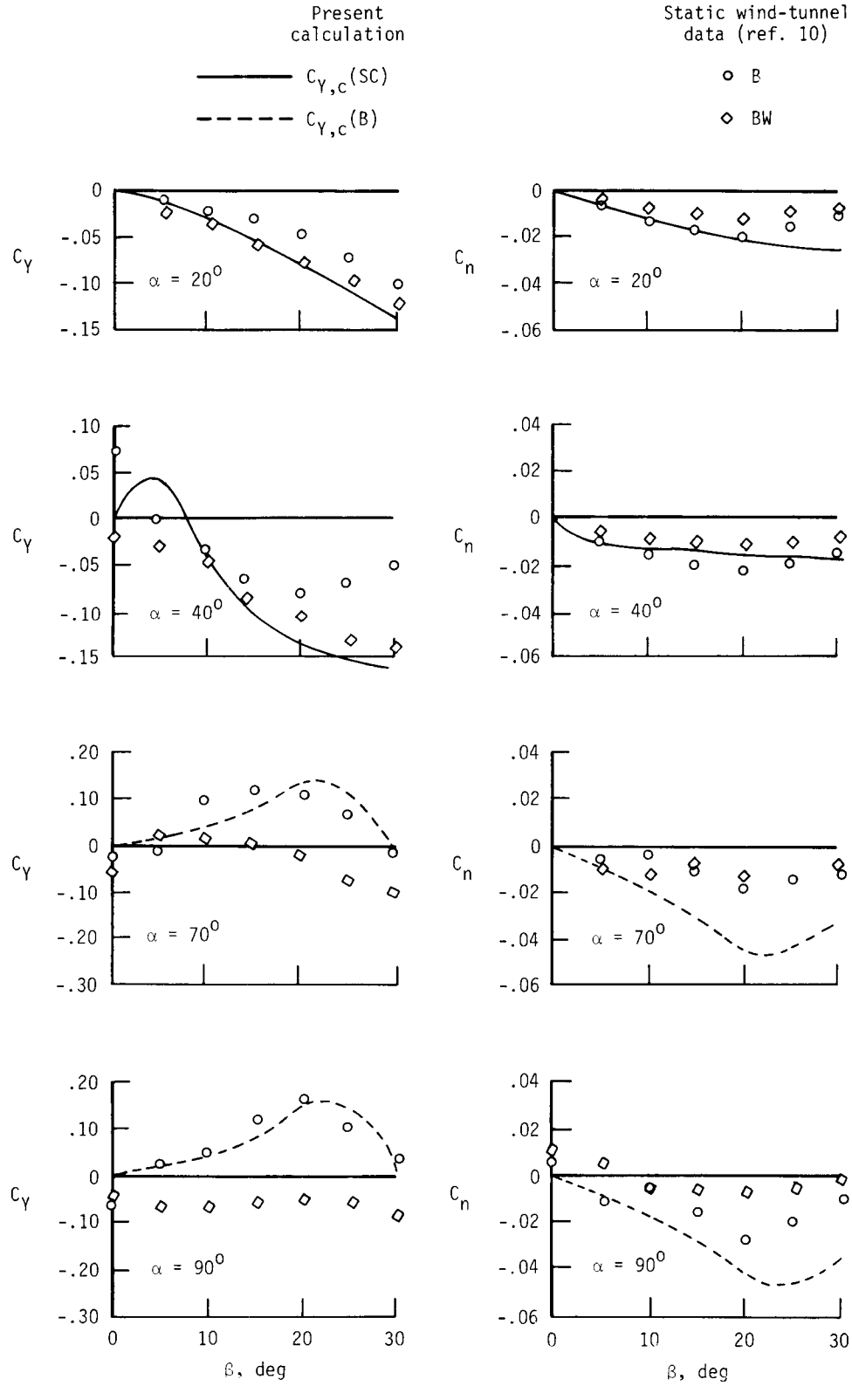

Figure 32. Comparison of static side-force and yawing-moment coefficients of body-alone and wing-body configurations.

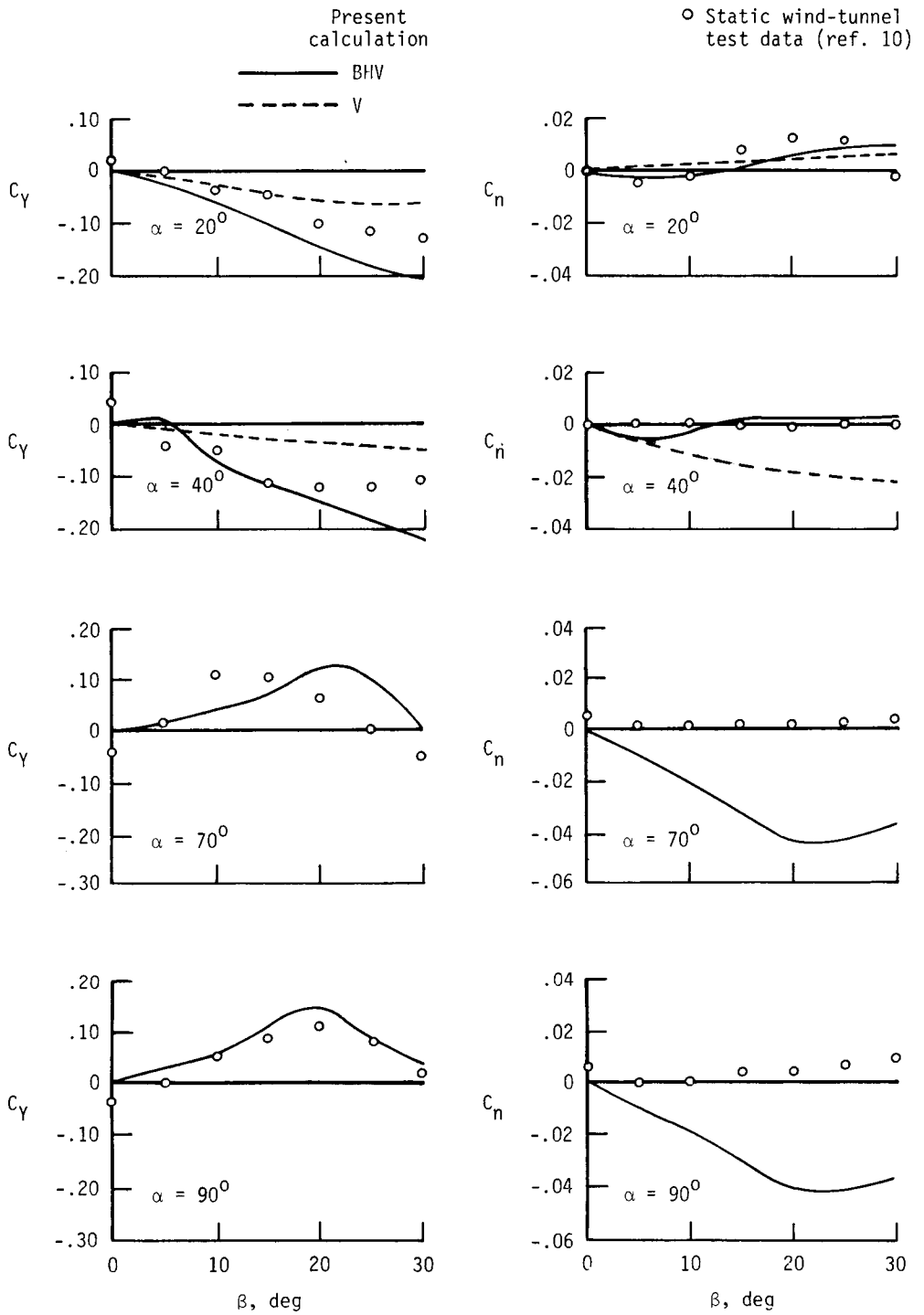

(a) Tail 3 configuration.

Figure 33. Static side-force and yawing-moment coefficients of BHV configuration.

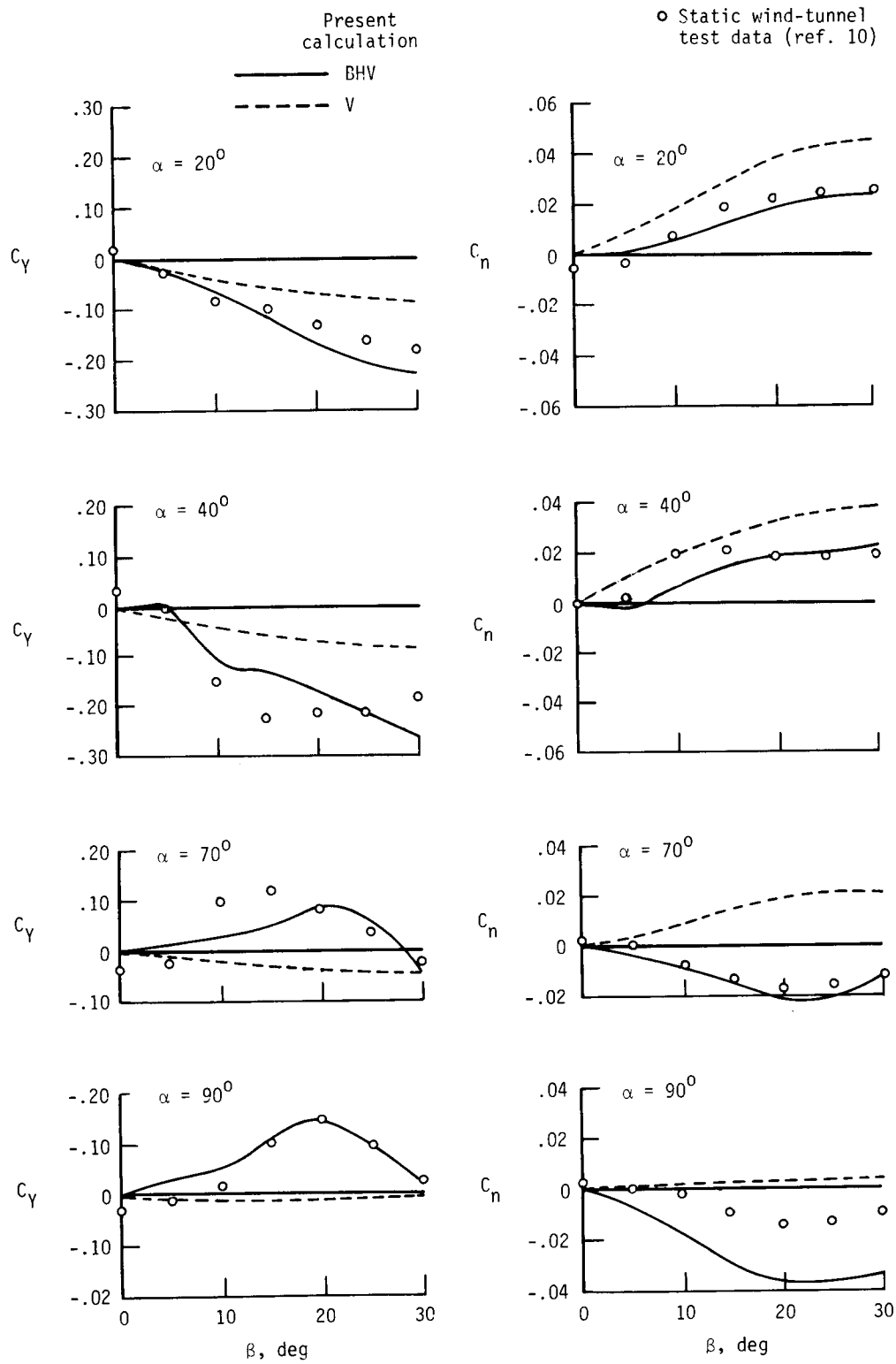

(b) Tail 4 configuration.

Figure 33. Concluded.

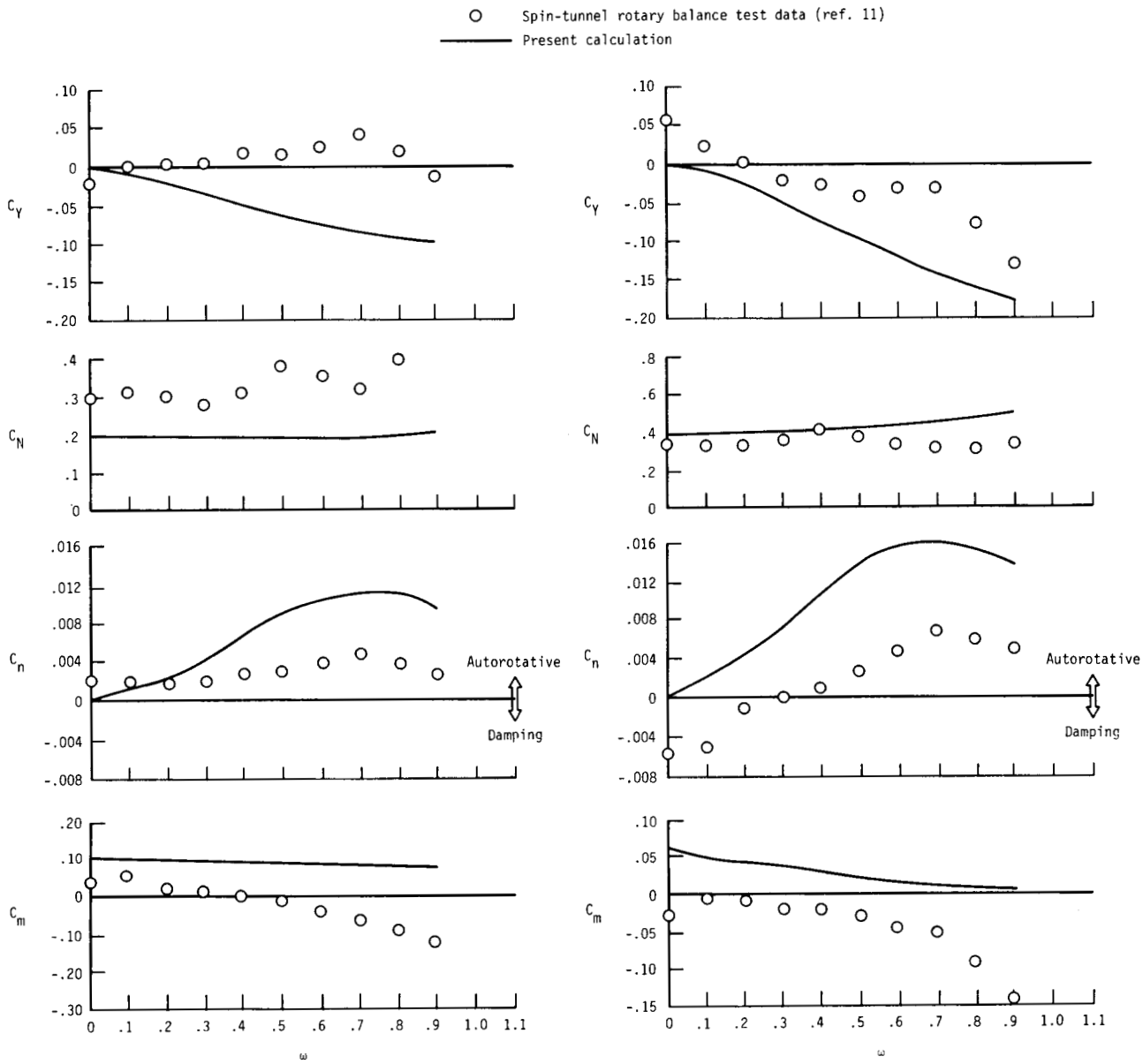

(a) $\alpha = 30°$.

(b) $\alpha = 45°$.

Figure 34. Rotary aerodynamic characteristics of body (B) configuration.

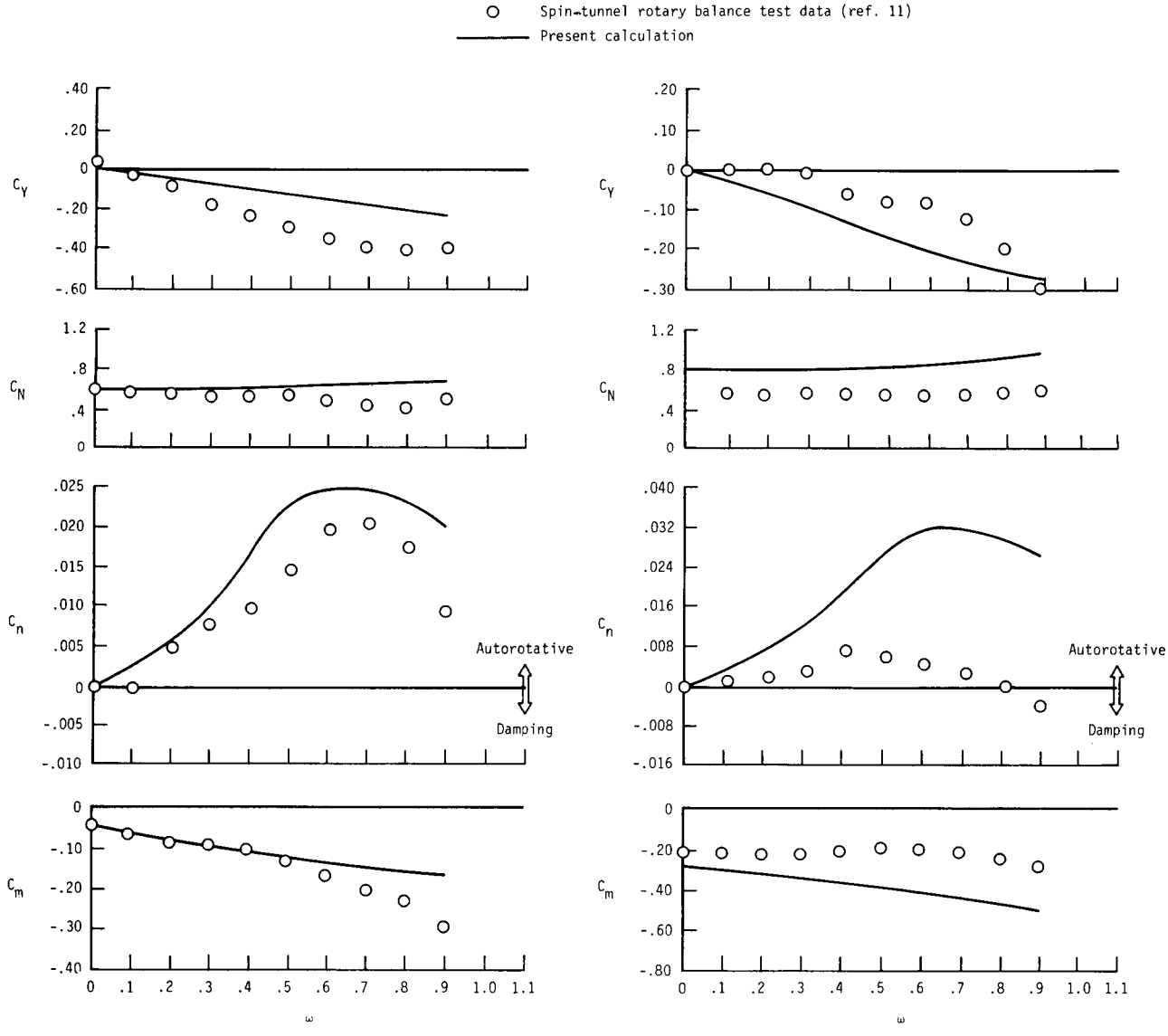

(c) $\alpha = 60°$.

(d) $\alpha = 90°$.

Figure 34. Concluded.

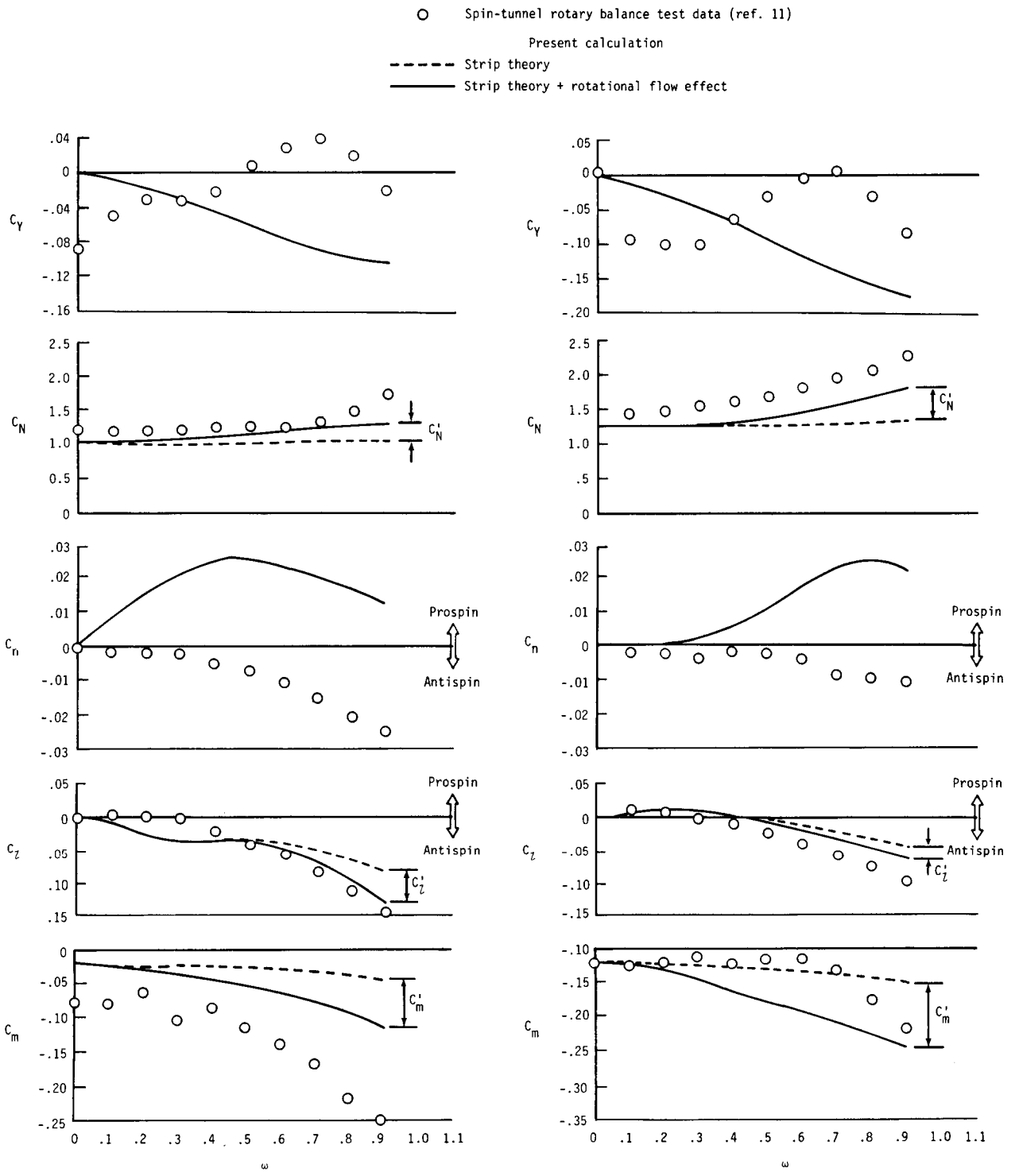

(a) $\alpha = 30°$.

(b) $\alpha = 45°$.

Figure 35. Rotary aerodynamic characteristics of BW configuration.

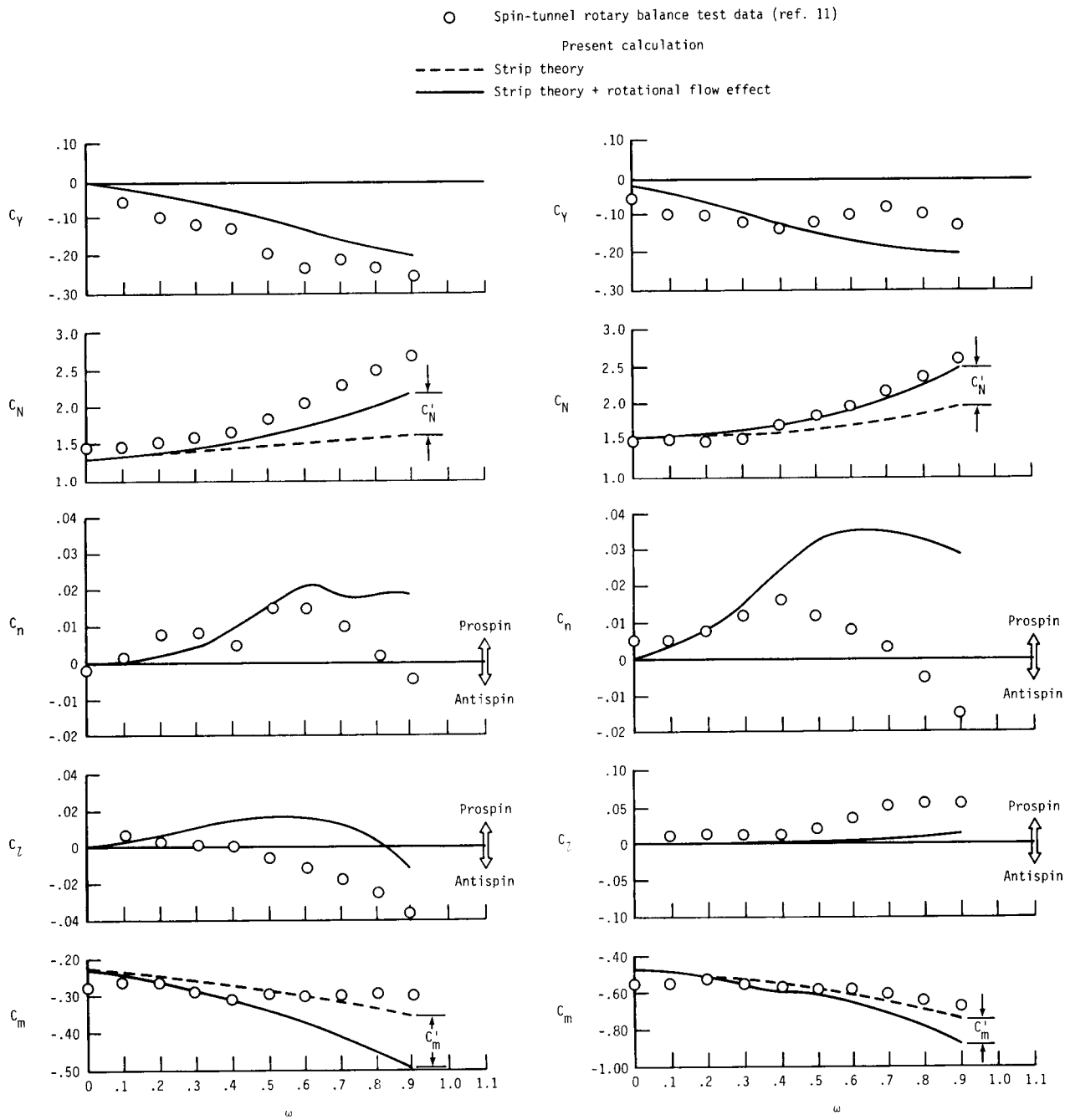

(c) $\alpha = 60°$.

(d) $\alpha = 90°$.

Figure 35. Concluded.

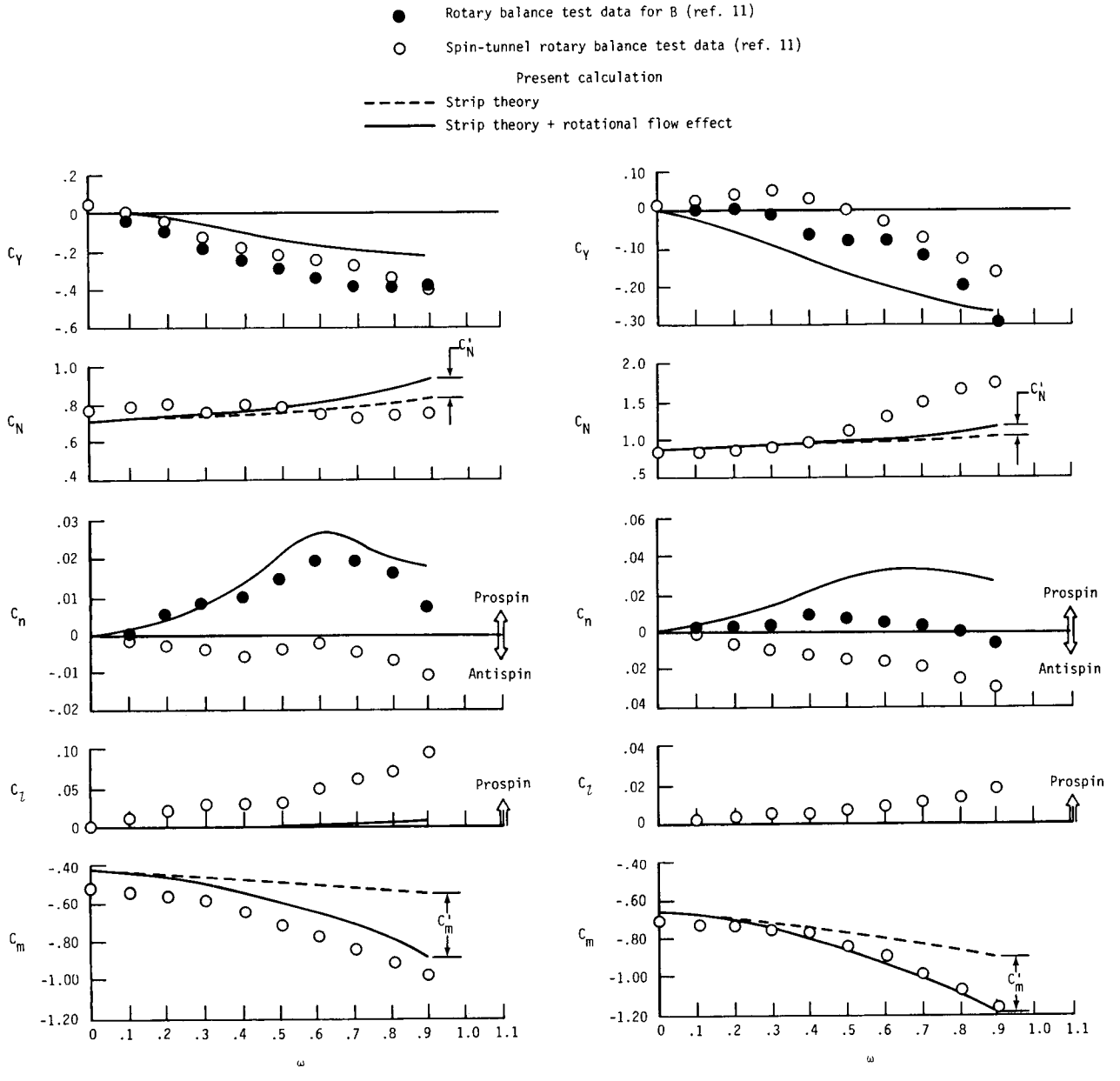

(a) $\alpha = 60°$.

(b) $\alpha = 90°$.

Figure 36. Rotary aerodynamic characteristics of BH configuration.

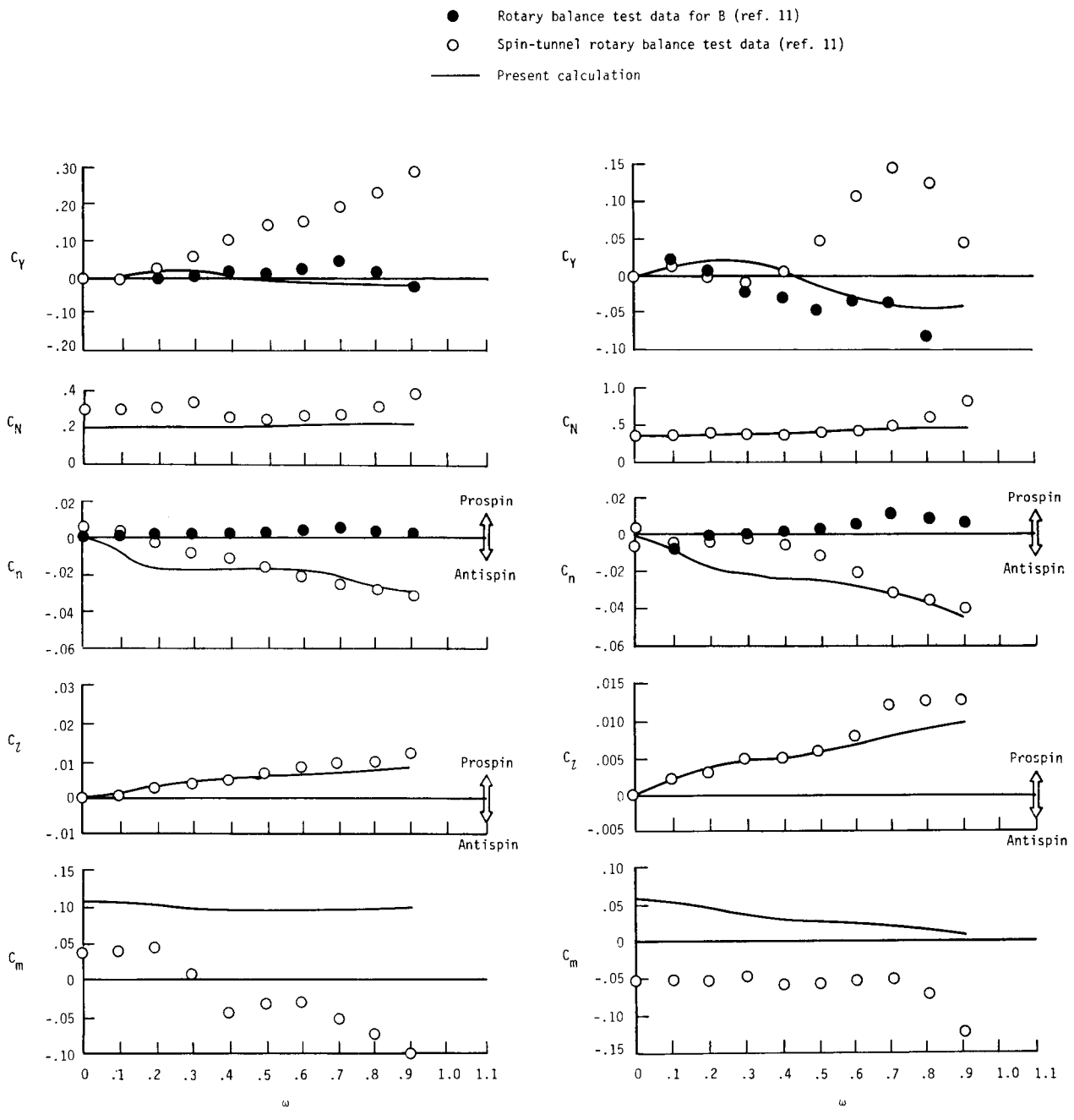

(a) $\alpha = 30°$.

(b) $\alpha = 45°$.

Figure 37. Rotary aerodynamic characteristics of BV configuration.

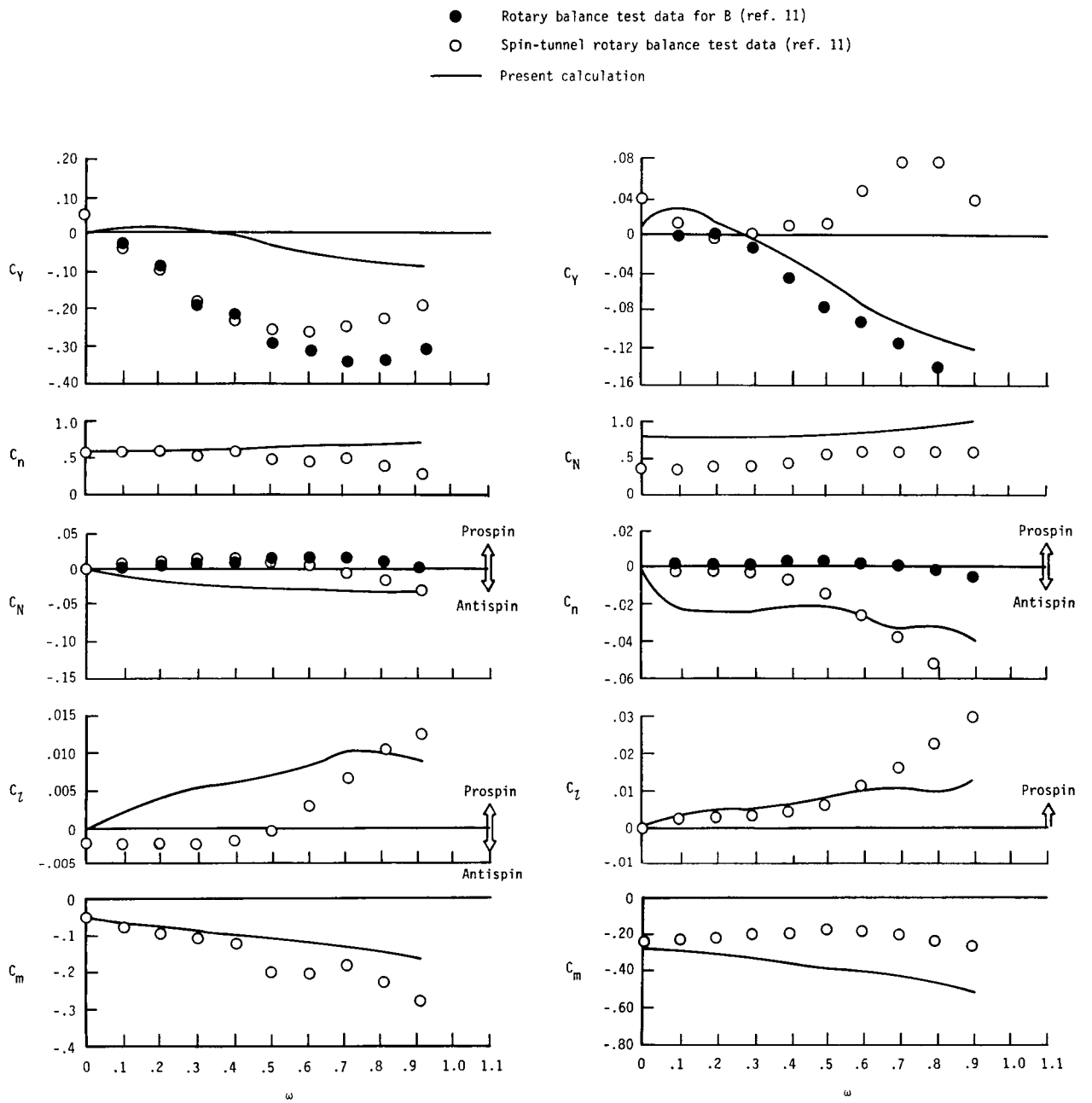

(c) $\alpha = 60°$.

(d) $\alpha = 90°$.

Figure 37. Concluded.

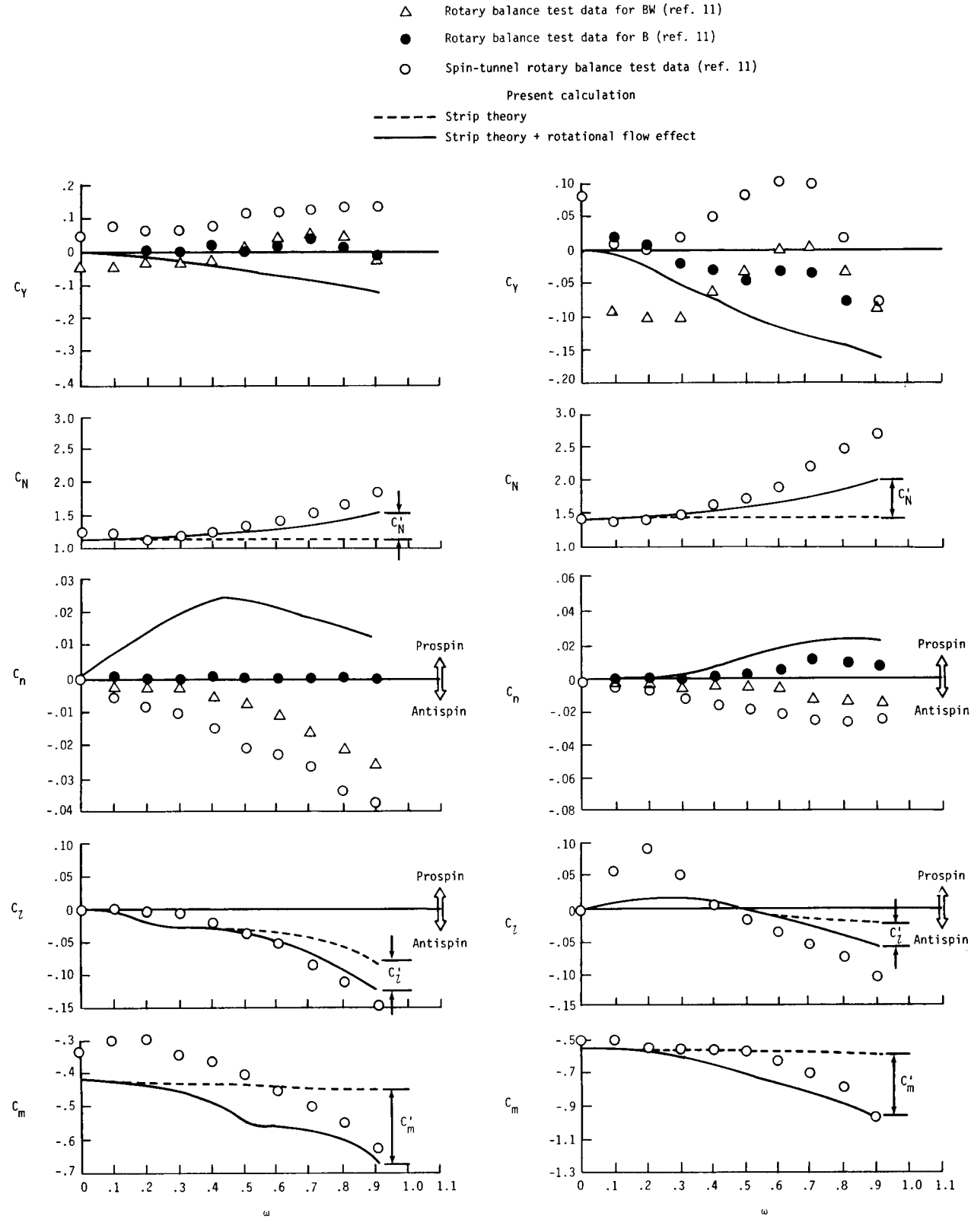

(a) $\alpha = 30°$.

(b) $\alpha = 45°$.

Figure 38. Rotary aerodynamic characteristics of BWH configuration with tail 3.

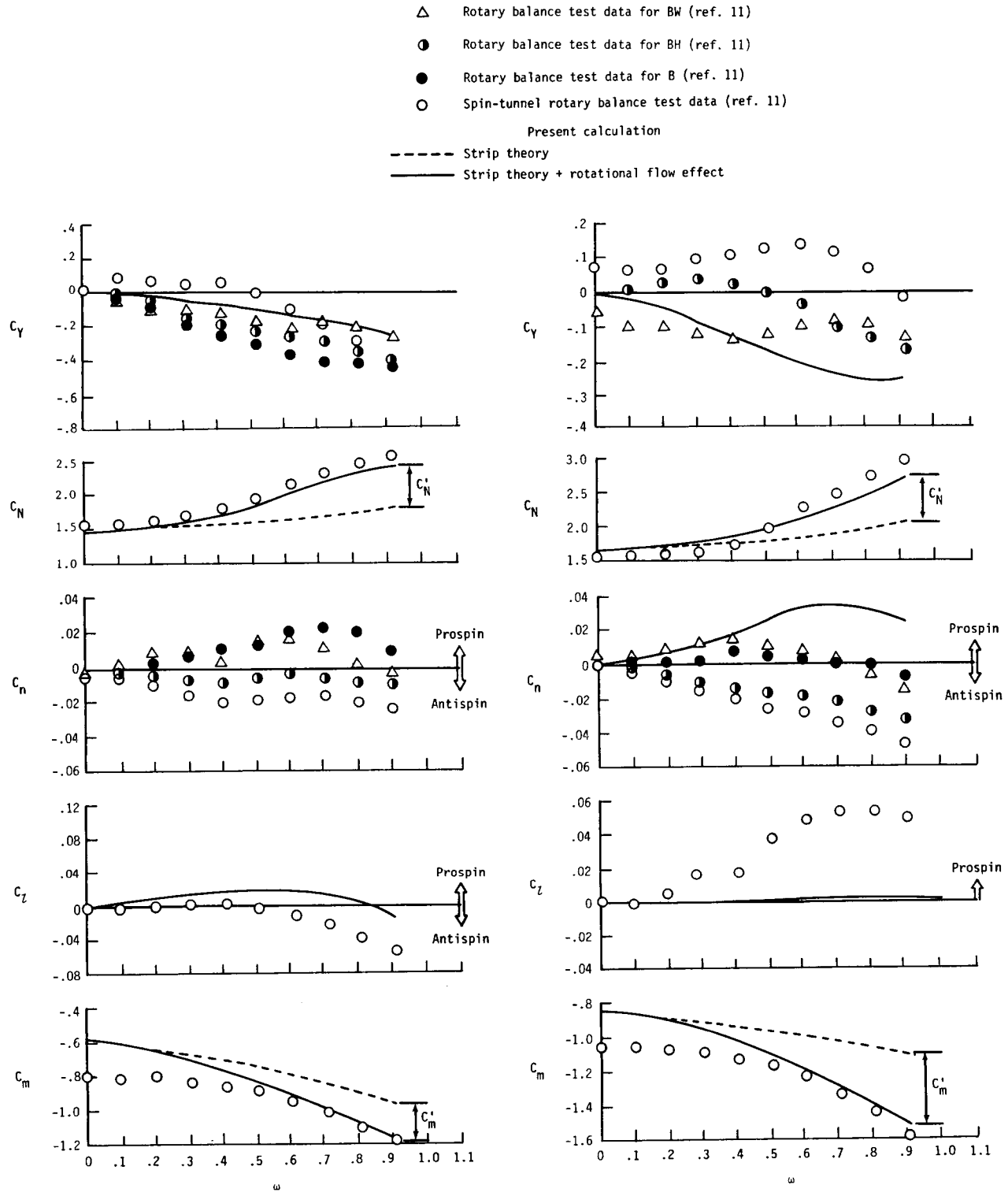

(c) $\alpha = 60°$.

(d) $\alpha = 90°$.

Figure 38. Concluded.

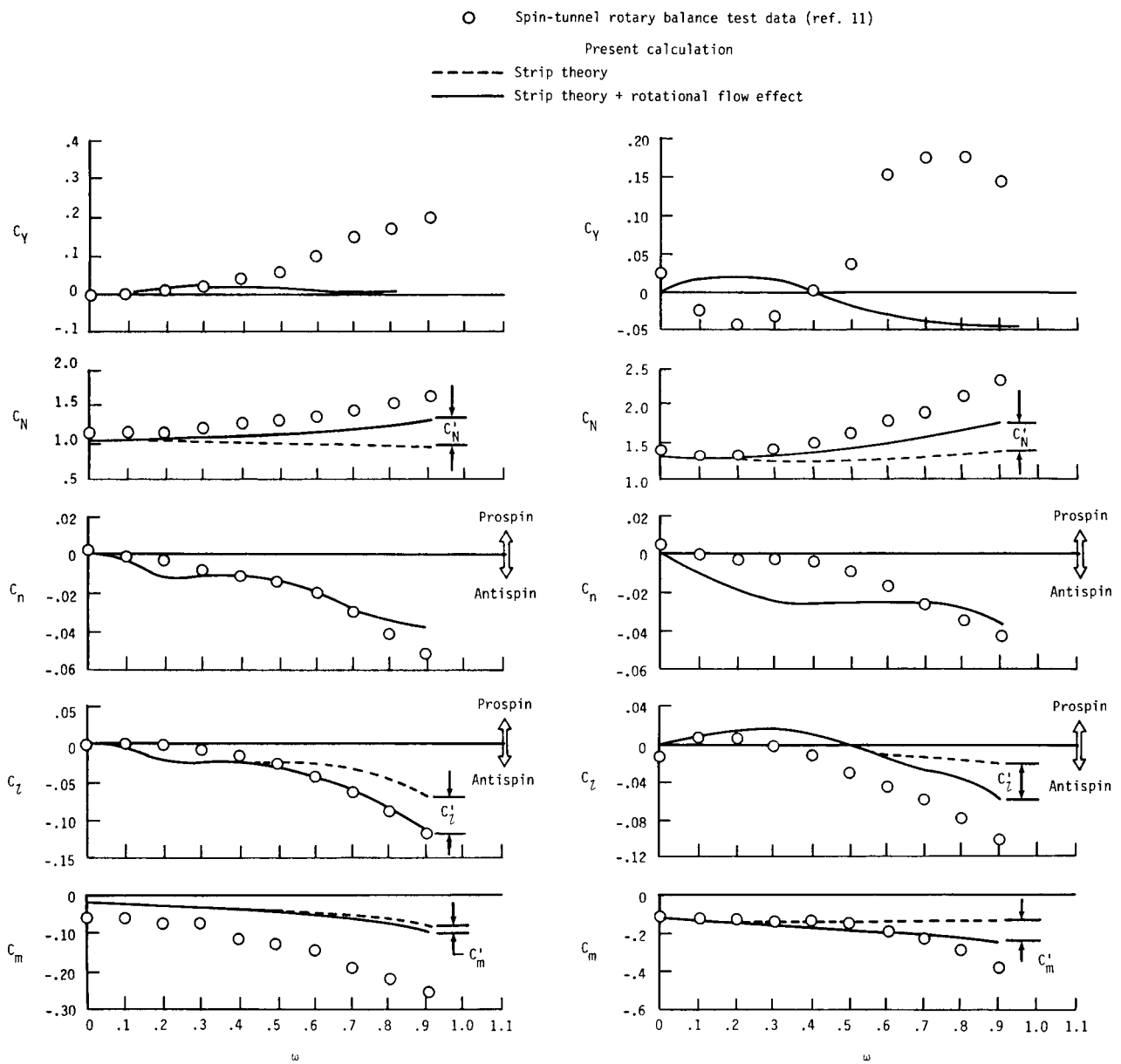

(a) $\alpha = 30°$.

(b) $\alpha = 45°$.

Figure 39. Rotary aerodynamic characteristics of BWV configuration.

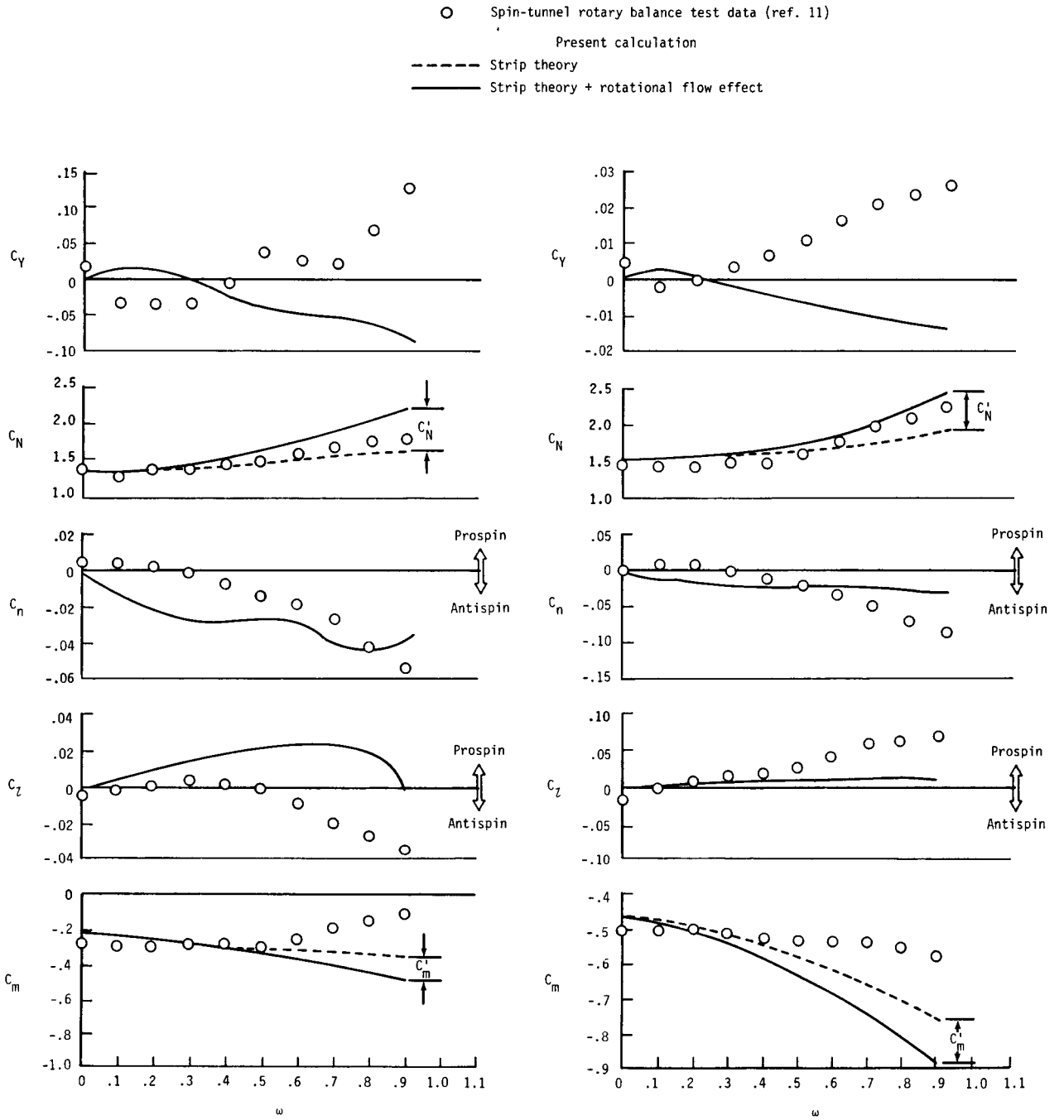

(c) $\alpha = 60°$.

(d) $\alpha = 90°$.

Figure 39. Concluded.

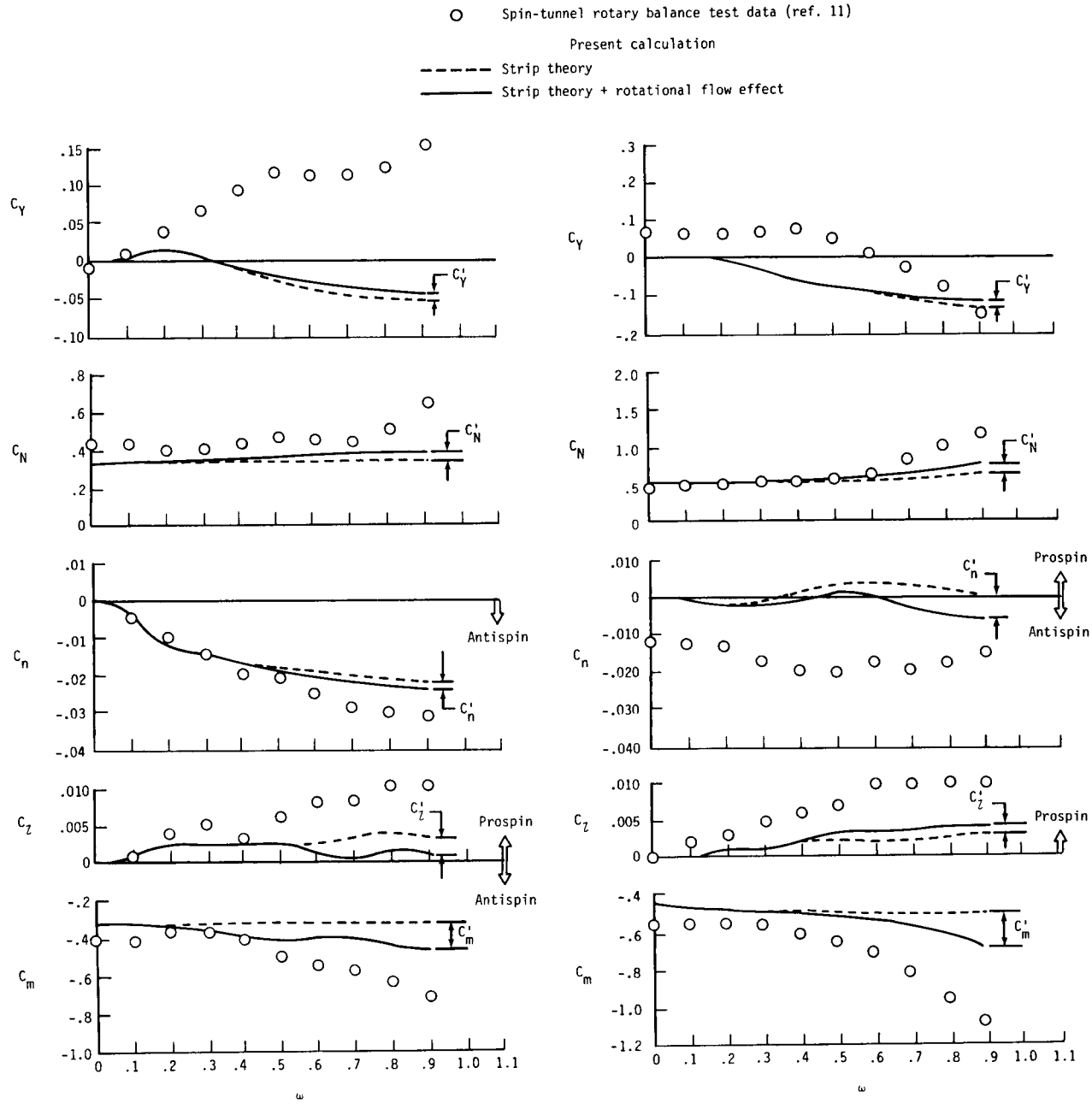

(a) $\alpha = 30°$.

(b) $\alpha = 45°$.

Figure 40. Rotary aerodynamic characteristics of BHV configuration with tail 3.

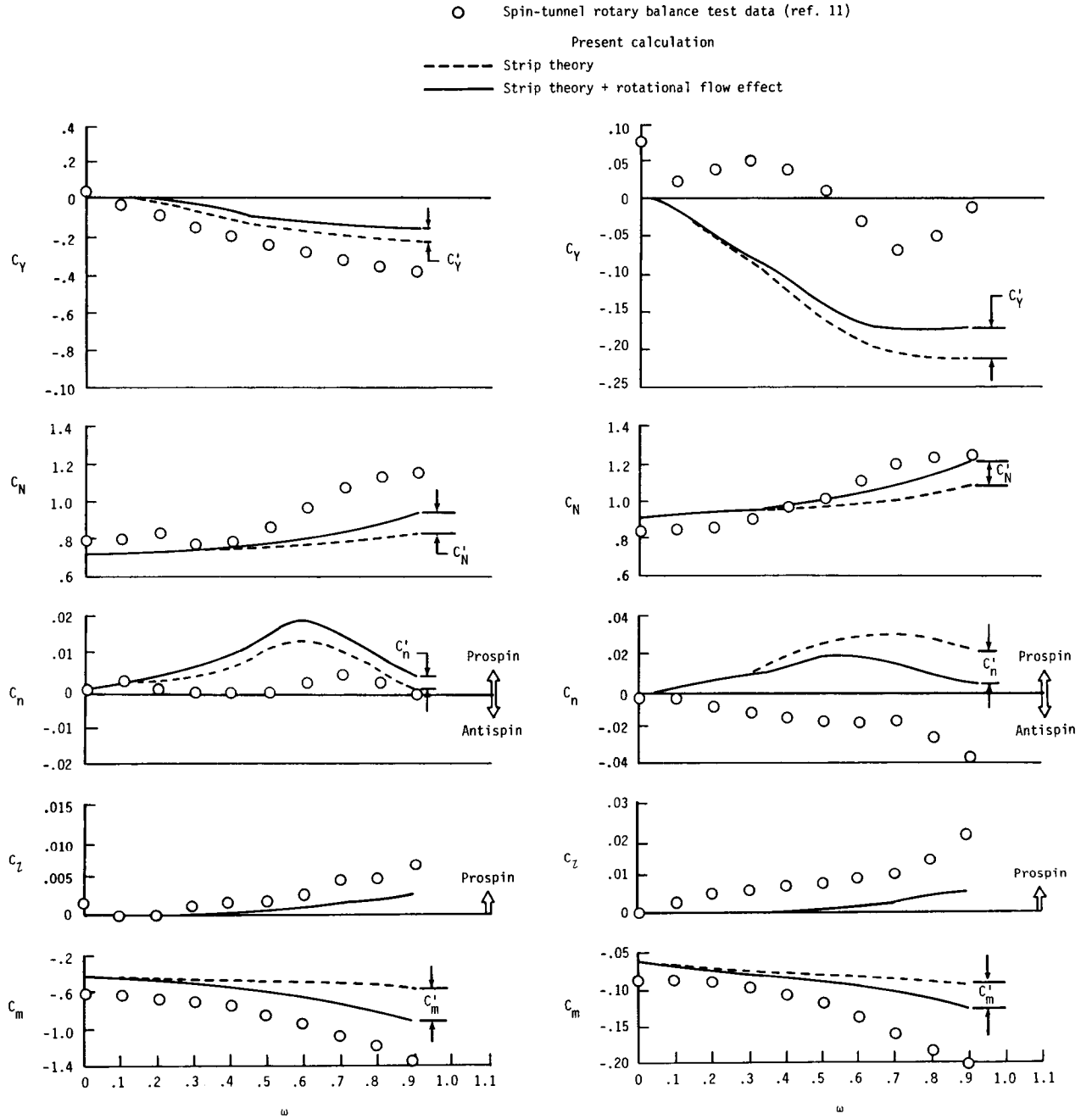

(c) $\alpha = 60°$.

(d) $\alpha = 90°$.

Figure 40. Concluded.

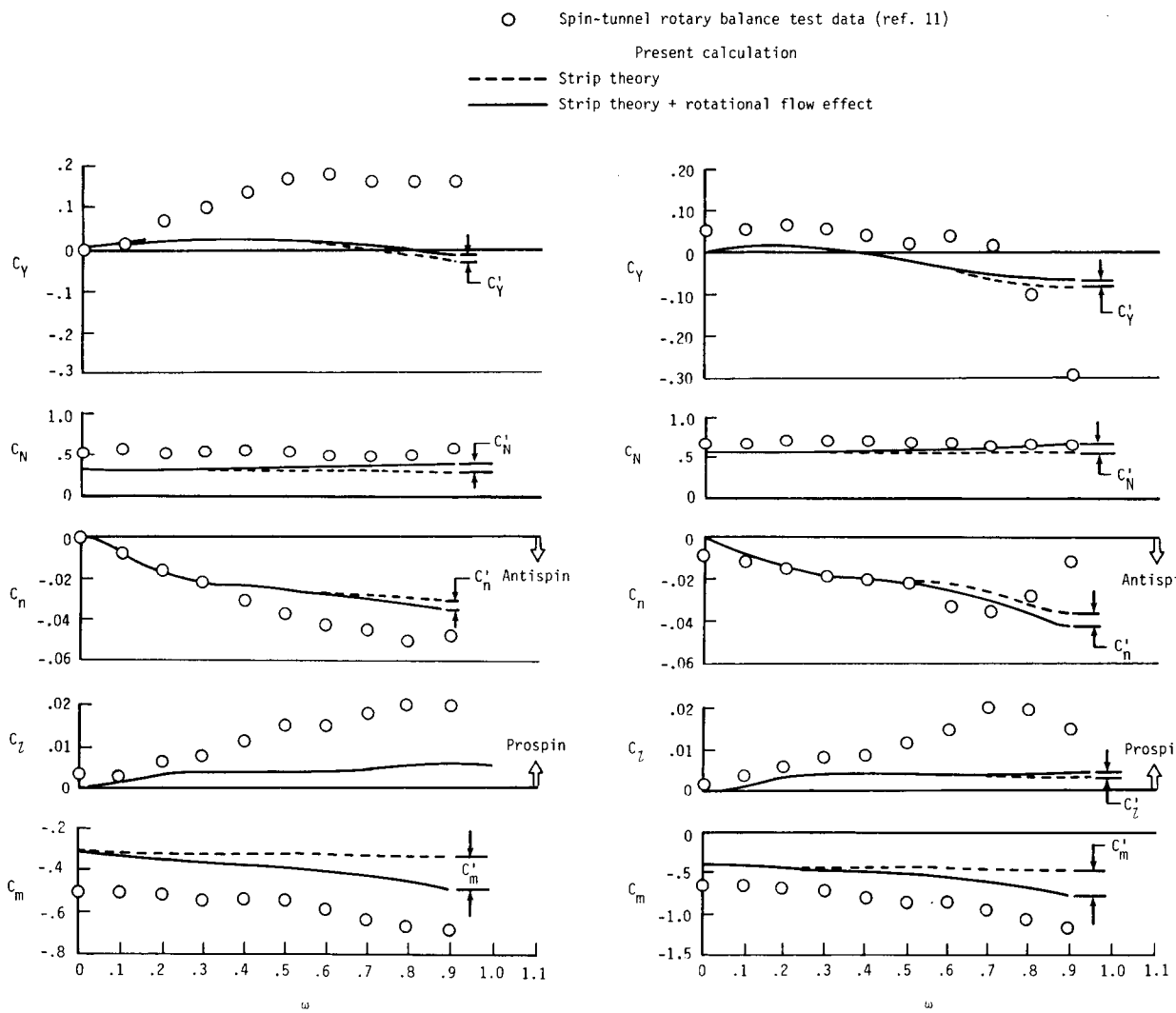

(a) $\alpha = 30°$.

(b) $\alpha = 45°$.

Figure 41. Rotary aerodynamic characteristics of BHV configuration with tail 4.

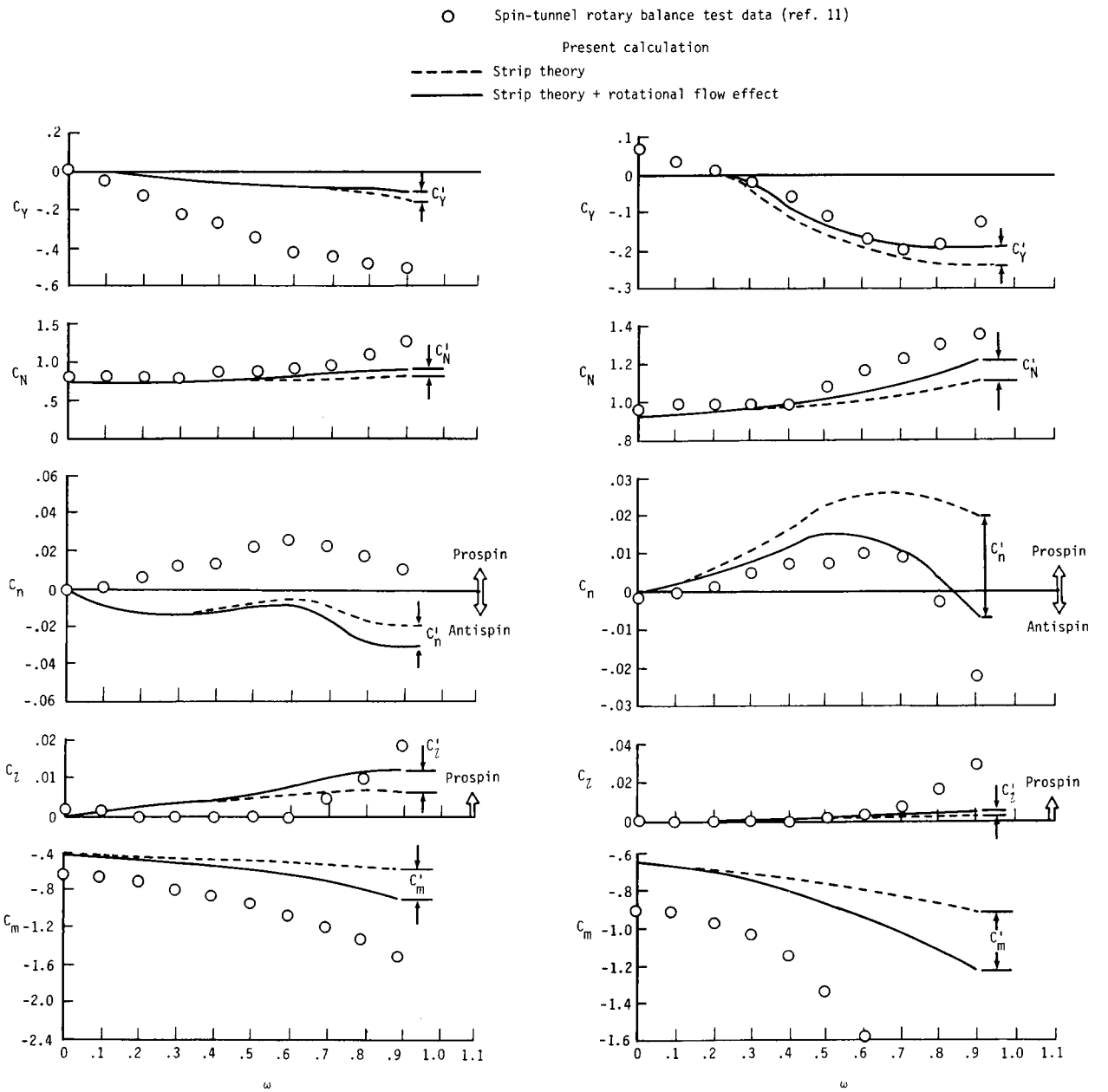

(c) $\alpha = 60°$.

(d) $\alpha = 90°$.

Figure 41. Concluded.

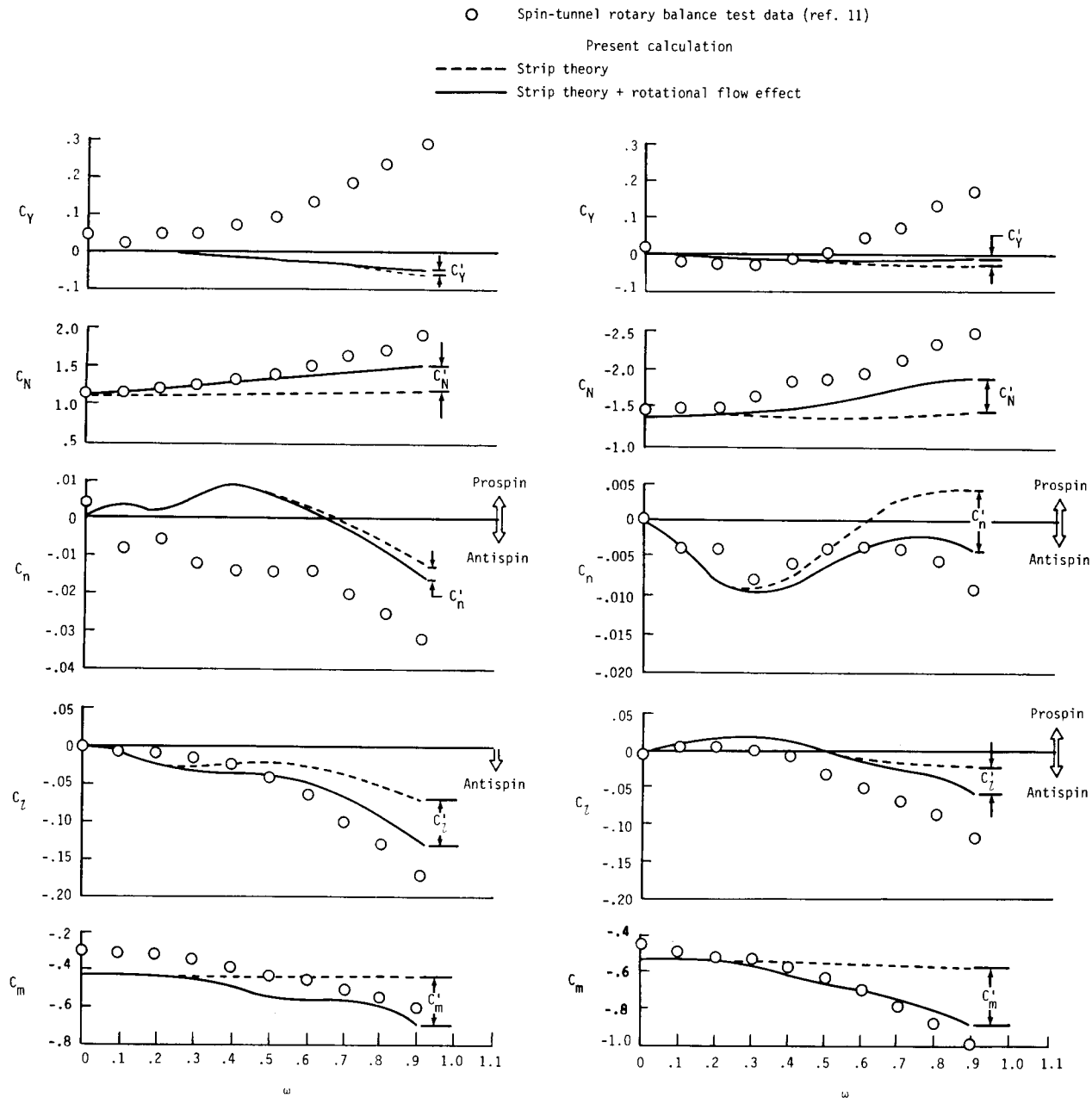

(a) $\alpha = 30°$.

(b) $\alpha = 45°$.

Figure 42. Rotary aerodynamic characteristics of BWHV configuration with tail 3.

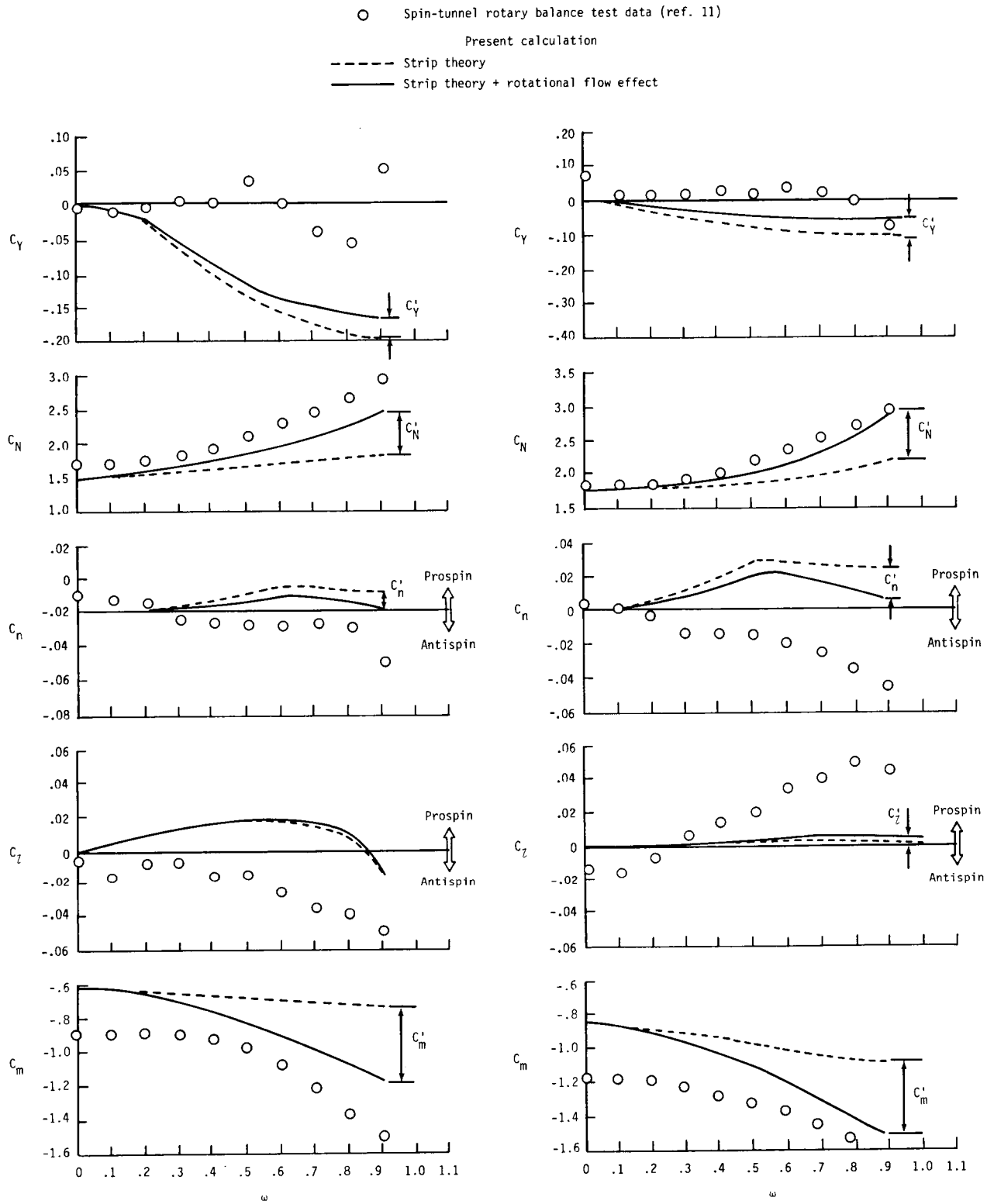

(c) $\alpha = 60°$.

(d) $\alpha = 90°$.

Figure 42. Concluded.

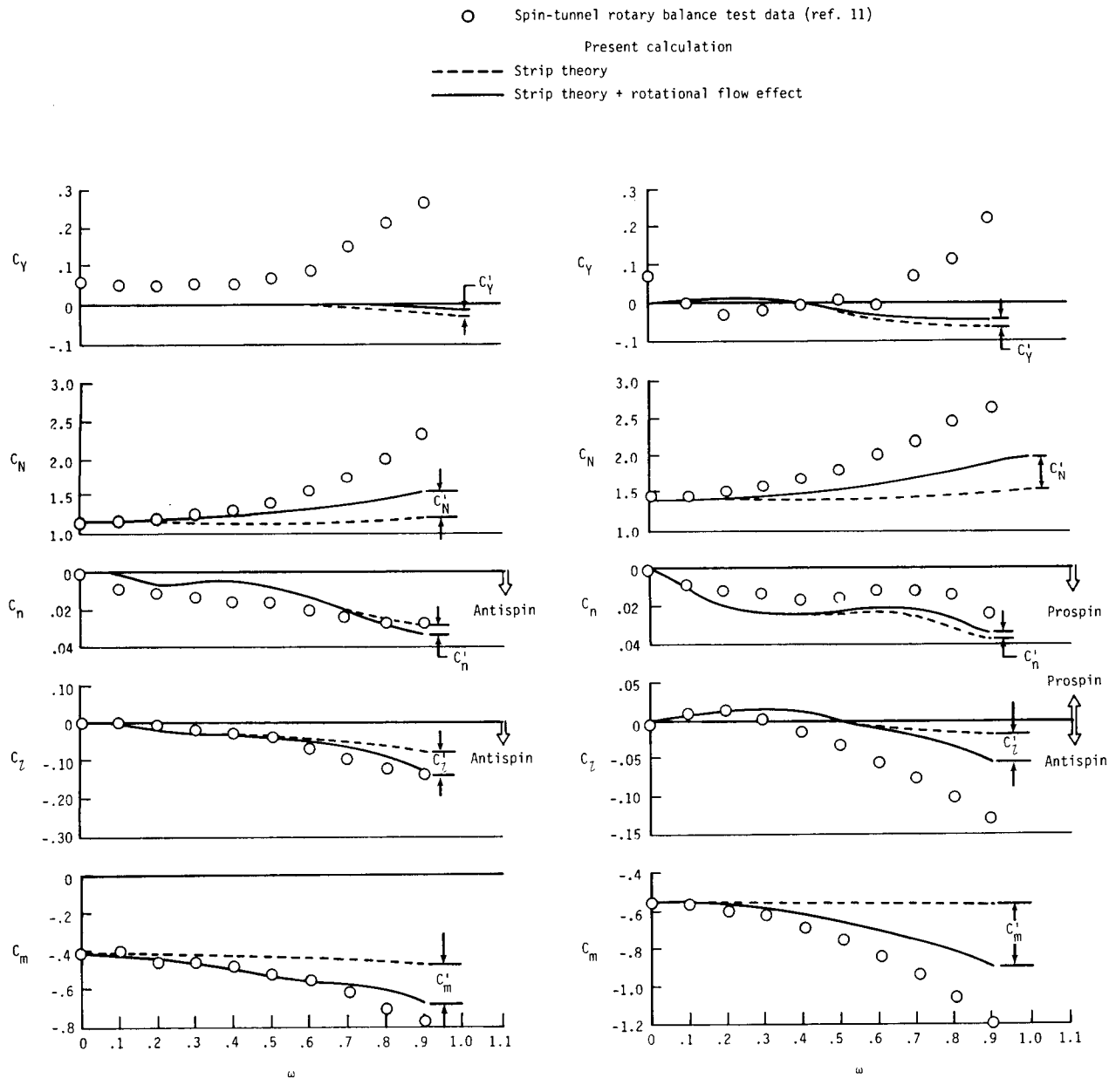

(a) $\alpha = 30°$.

(b) $\alpha = 45°$.

Figure 43. Rotary aerodynamic characteristics of BWHV configuration with tail 4.

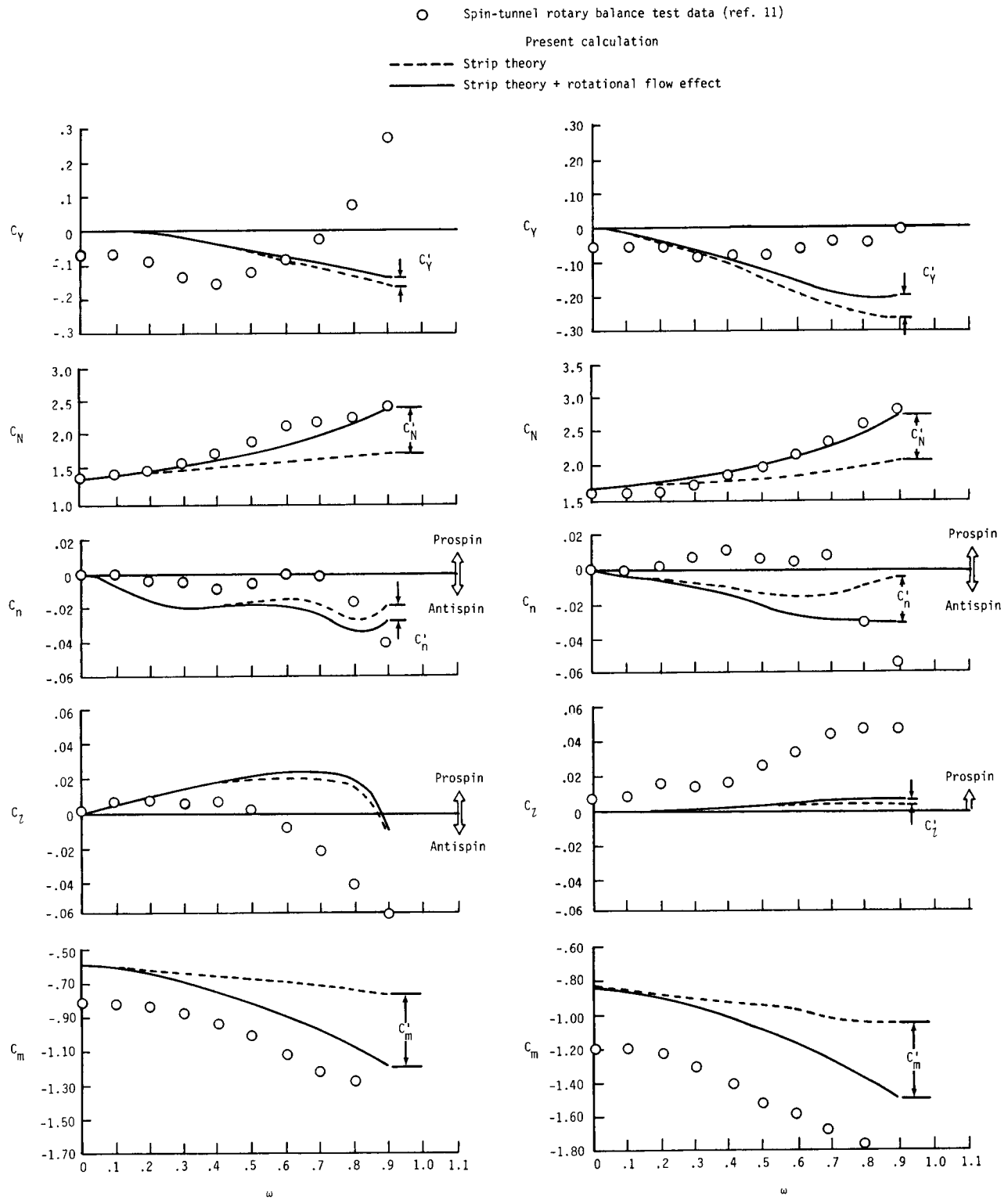

(c) $\alpha = 60°$.

(d) $\alpha = 90°$.

Figure 43. Concluded.

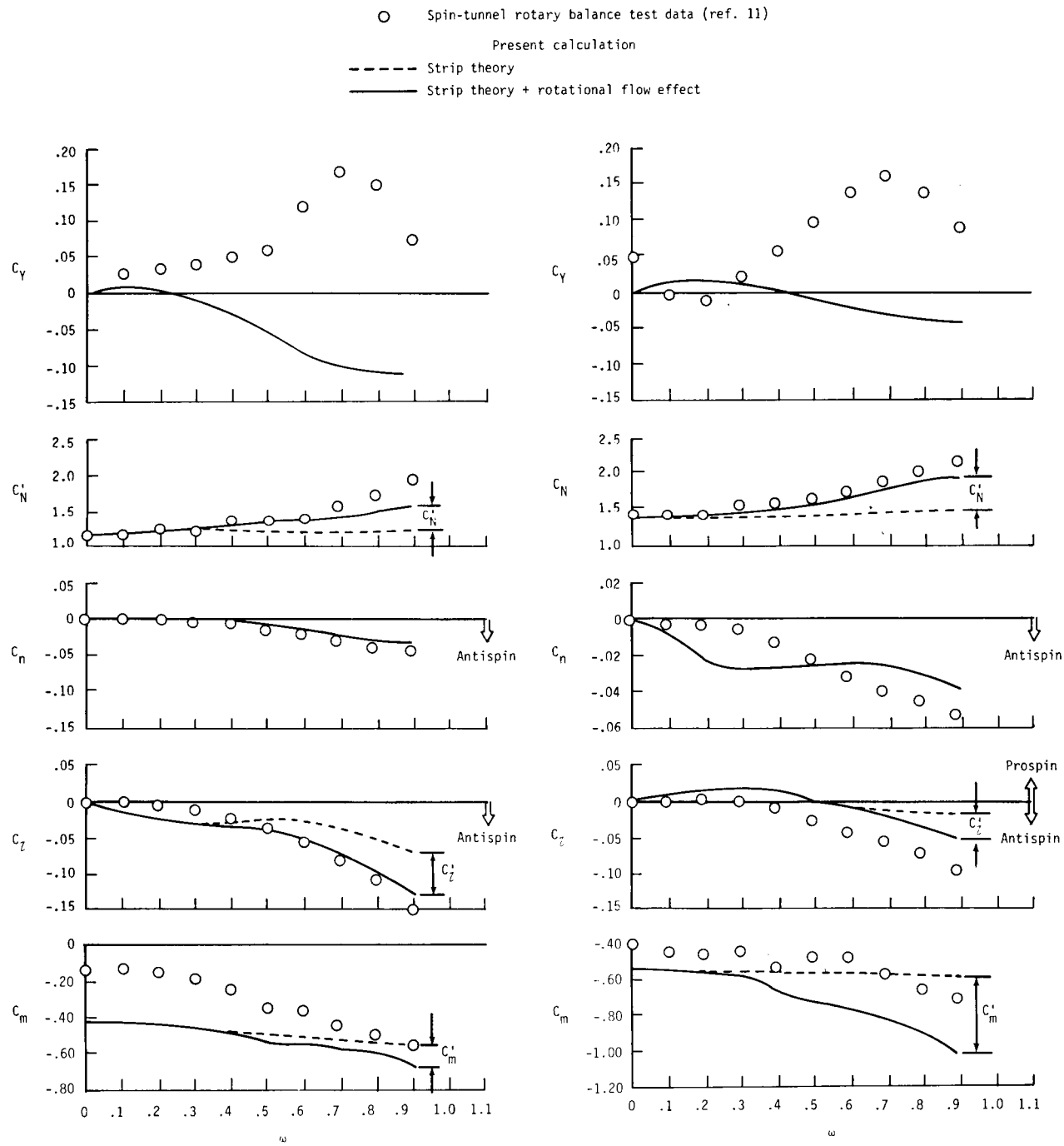

(a) $\alpha = 30°$.

(b) $\alpha = 45°$.

Figure 44. Rotary aerodynamic characteristics of BWHV configuration with tail 5.

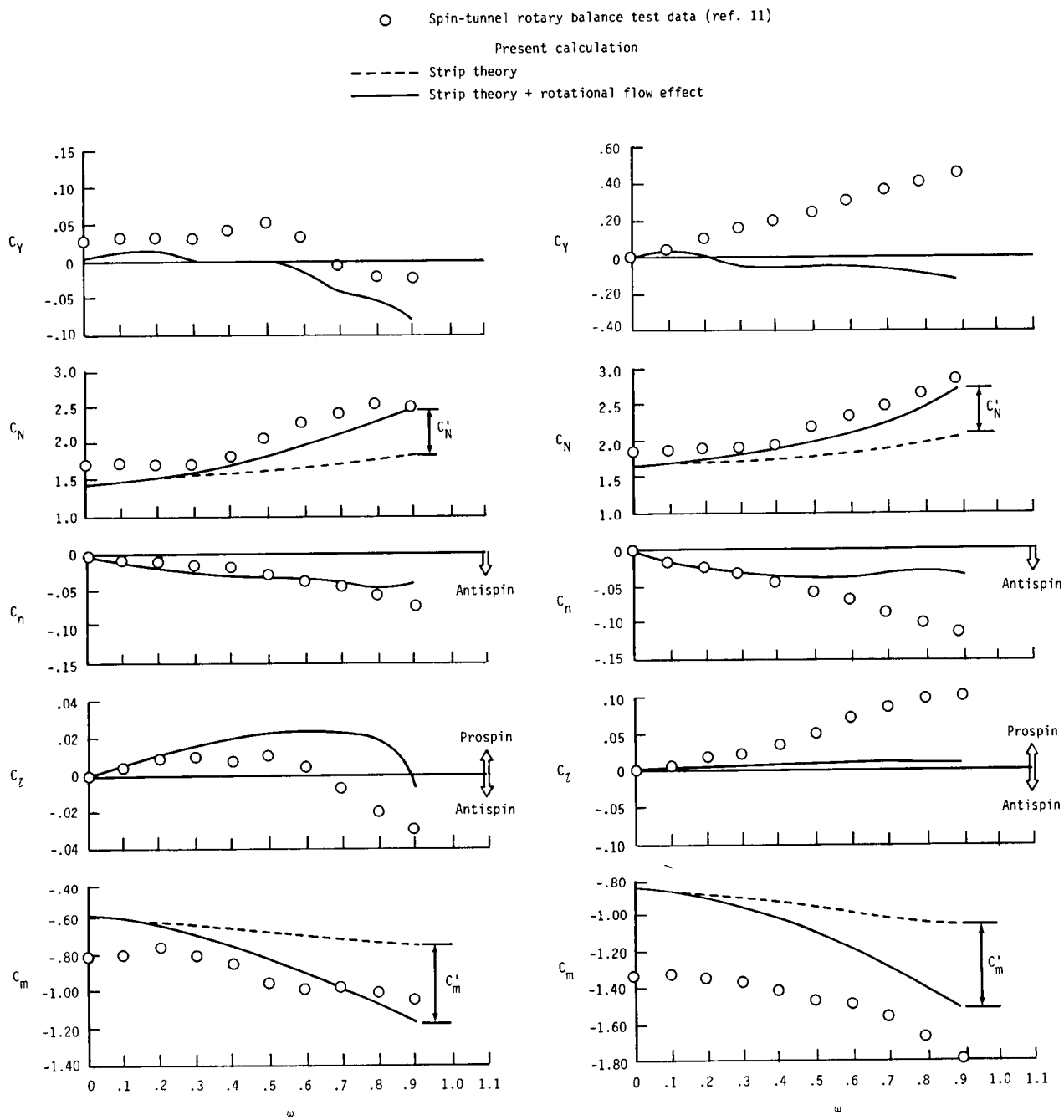

(c) $\alpha = 60°$.

(d) $\alpha = 90°$.

Figure 44. Concluded.

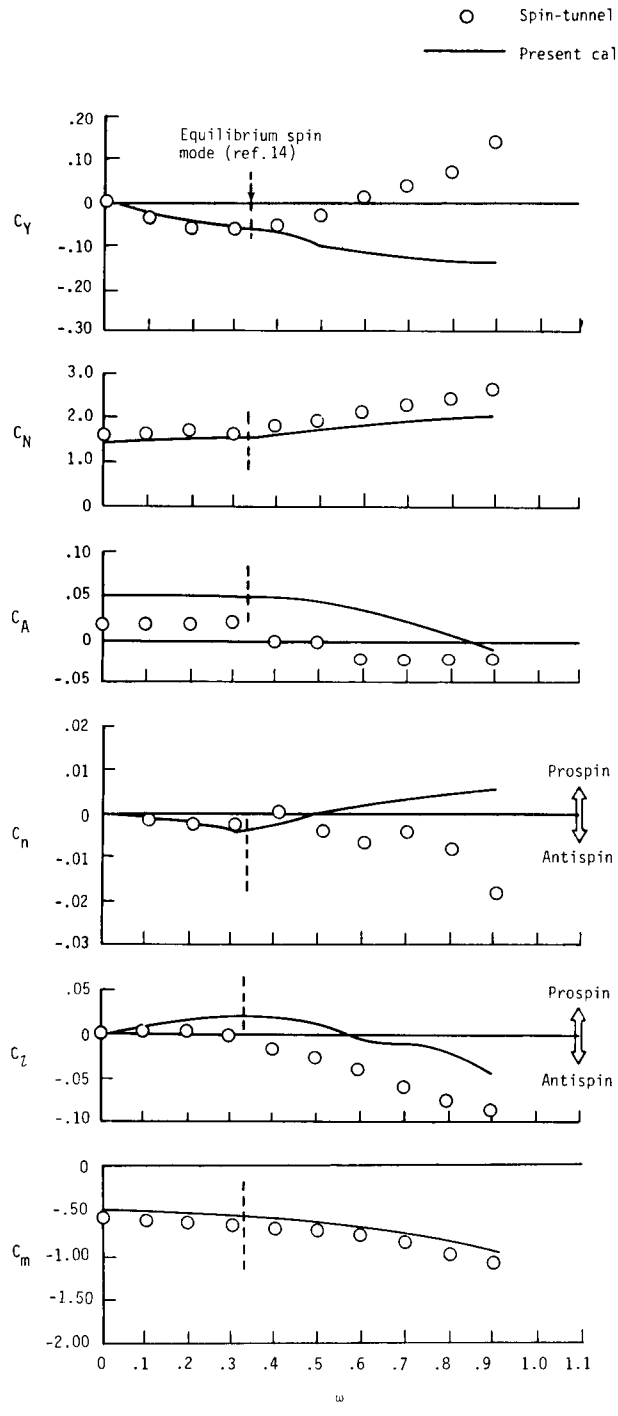

Figure 45. Rotary aerodynamic characteristics of model A airplane with tail 3 at moderately flat spin attitude. $\alpha = 50°$.

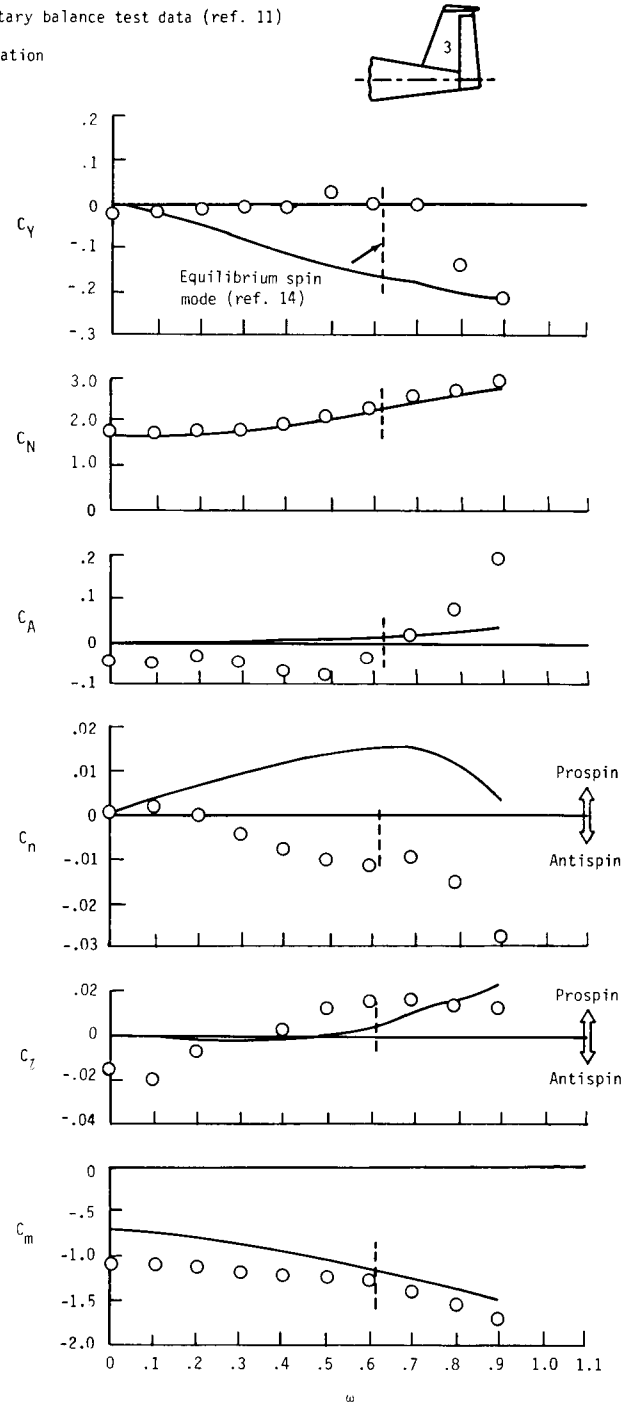

Figure 46. Rotary aerodynamic characteristics of model A airplane with tail 3 at flat spin attitude. $\alpha = 80°$.

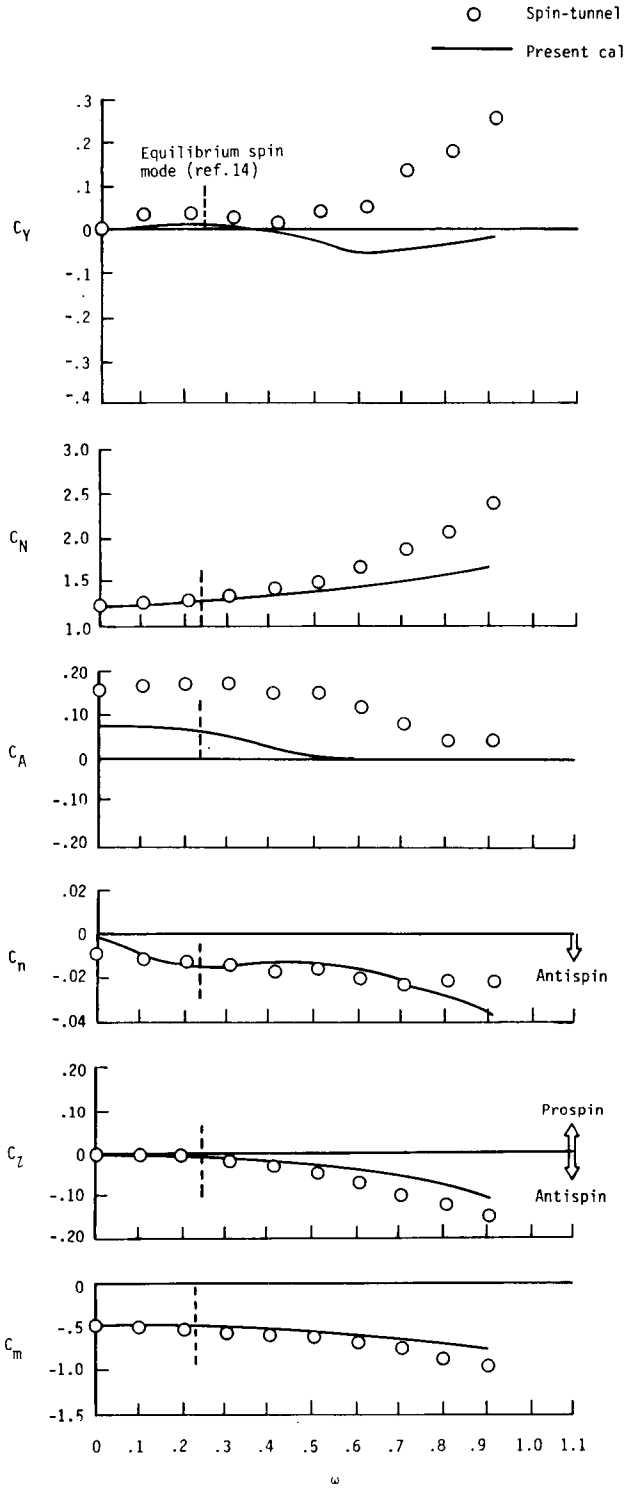

Figure 47. Rotary aerodynamic characteristics of model A airplane with tail 4 at steep spin attitude. $\alpha = 35°$.

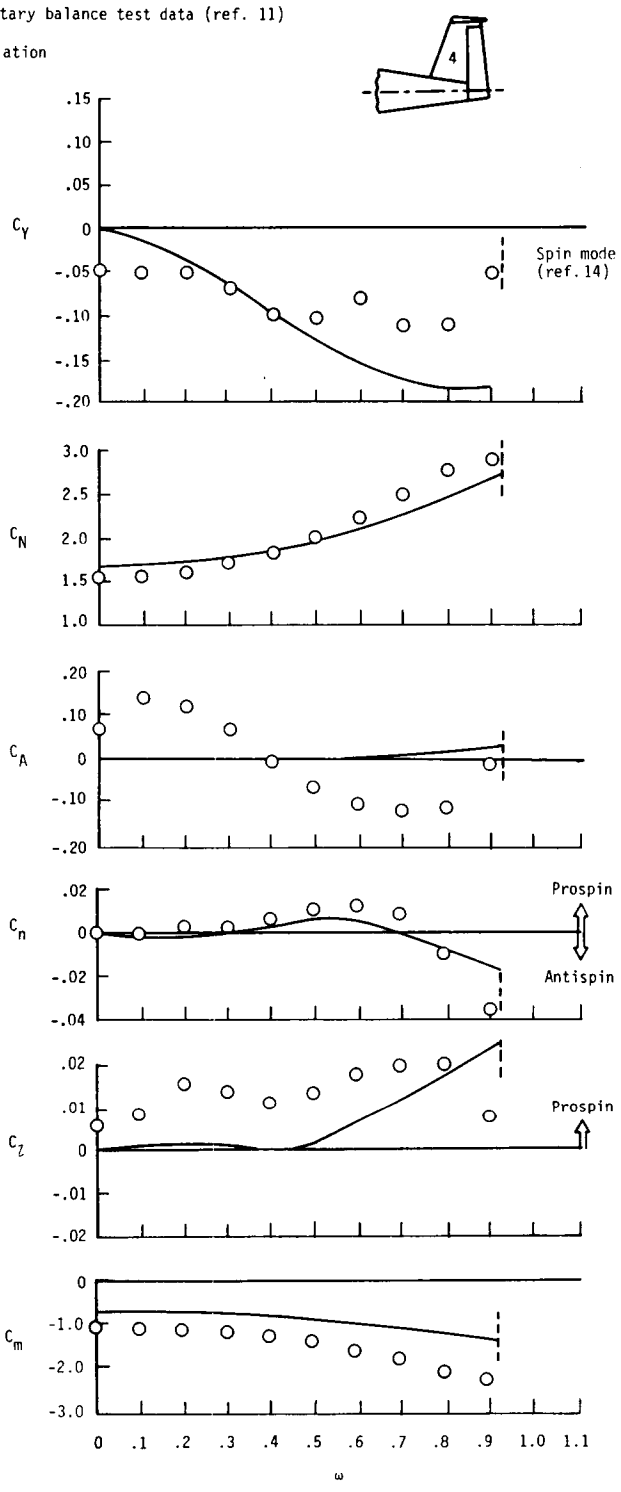

Figure 48. Rotary aerodynamic characteristics of model A airplane with tail 4 at flat spin attitude. $\alpha = 80°$.

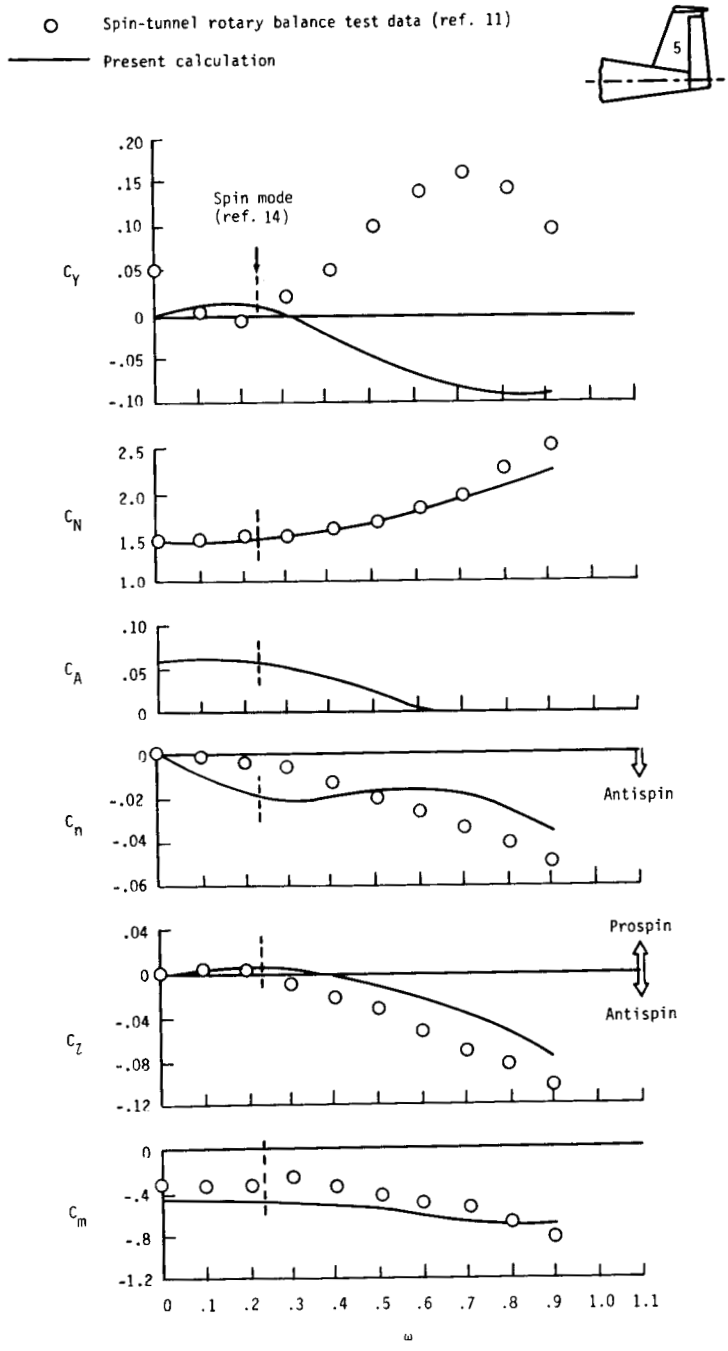

Figure 49. Rotary aerodynamic characteristics of model A airplane with tail 5 at moderately steep spin attitude. $\alpha = 40°$.

NASA
National Aeronautics and Space Administration

Report Documentation Page

1. Report No.	2. Government Accession No.	3. Recipient's Catalog No.
NASA TM-4009		

4. Title and Subtitle	5. Report Date
Semiempirical Method for Prediction of Aerodynamic Forces and Moments on a Steadily Spinning Light Airplane	December 1987
	6. Performing Organization Code
7. Author(s)	8. Performing Organization Report No.
Bandu N. Pamadi and Lawrence W. Taylor, Jr.	L-15654
9. Performing Organization Name and Address	10. Work Unit No.
NASA Langley Research Center Hampton, VA 23665-5225	506-46-21-01
	11. Contract or Grant No.
12. Sponsoring Agency Name and Address	13. Type of Report and Period Covered
National Aeronautics and Space Administration Washington, DC 20546-0001	Technical Memorandum
	14. Sponsoring Agency Code

15. Supplementary Notes

Bandu N. Pamadi: Vigyan Research Associates, Inc., Hampton, Virginia.
Lawrence W. Taylor, Jr.: Langley Research Center, Hampton, Virginia.

16. Abstract

A semiempirical method is presented for the estimation of aerodynamic forces and moments acting on a steadily spinning (rotating) light airplane. The airplane is divided into wing, body, and tail surfaces. The effect of power is ignored. The strip theory is employed for each component of the spinning airplane to determine its contribution to the total aerodynamic coefficients. Then, increments to some of the coefficients which account for centrifugal effect are estimated. The theory is applied to a light, low-wing, single-engine general aviation airplane, and the results are compared with spin-tunnel rotary balance test data.

17. Key Words (Suggested by Authors(s))	18. Distribution Statement
Airplane spin Aerodynamics of spinning airplane	Unclassified—Unlimited Subject Category 02

19. Security Classif.(of this report)	20. Security Classif.(of this page)	21. No. of Pages	22. Price
Unclassified	Unclassified	86	A05

NASA FORM 1626 OCT 86 NASA-Langley, 1987
For sale by the National Technical Information Service, Springfield, Virginia 22161-2171